



**Numerical Investigation of Aerodynamics of
Canard-Controlled Missile Using Planar and Grid Tail Fins,
Part II: Subsonic and Transonic Flow**

**by James DeSpirito, Milton E. Vaughn, Jr.,
and W. David Washington**

ARL-TR-3162

March 2004

NOTICES

Disclaimers

The findings in this report are not to be construed as an official Department of the Army position unless so designated by other authorized documents.

Citation of manufacturer's or trade names does not constitute an official endorsement or approval of the use thereof.

Destroy this report when it is no longer needed. Do not return it to the originator.

Army Research Laboratory

Aberdeen Proving Ground, MD 21005-5066

ARL-TR-3162

March 2004

Numerical Investigation of Aerodynamics of Canard-Controlled Missile Using Planar and Grid Tail Fins, Part II: Subsonic and Transonic Flow

James DeSpirito

Weapons and Materials Research Directorate, ARL

Milton E. Vaughn, Jr. and W. David Washington

U.S. Army Aviation and Missile Command

Report Documentation Page

Form Approved
OMB No. 0704-0188

Public reporting burden for this collection of information is estimated to average 1 hour per response, including the time for reviewing instructions, searching existing data sources, gathering and maintaining the data needed, and completing and reviewing the collection information. Send comments regarding this burden estimate or any other aspect of this collection of information, including suggestions for reducing the burden, to Department of Defense, Washington Headquarters Services, Directorate for Information Operations and Reports (0704-0188), 1215 Jefferson Davis Highway, Suite 1204, Arlington, VA 22202-4302. Respondents should be aware that notwithstanding any other provision of law, no person shall be subject to any penalty for failing to comply with a collection of information if it does not display a currently valid OMB control number.
PLEASE DO NOT RETURN YOUR FORM TO THE ABOVE ADDRESS.

1. REPORT DATE (DD-MM-YYYY) March 2004		2. REPORT TYPE Final		3. DATES COVERED (From - To) June 2002–February 2003	
4. TITLE AND SUBTITLE Numerical Investigation of Aerodynamics of Canard-Controlled Missile Using Planar and Grid Tail Fins, Part II: Subsonic and Transonic Flow				5a. CONTRACT NUMBER	
				5b. GRANT NUMBER	
				5c. PROGRAM ELEMENT NUMBER	
6. AUTHOR(S) James DeSpirito, Milton E. Vaughn, Jr.,* and W. David Washington*				5d. PROJECT NUMBER 1L162618AH80	
				5e. TASK NUMBER	
				5f. WORK UNIT NUMBER	
7. PERFORMING ORGANIZATION NAME(S) AND ADDRESS(ES) U.S. Army Research Laboratory ATTN: AMSRD-ARL-WM-BC Aberdeen Proving Ground, MD 21005-5066				8. PERFORMING ORGANIZATION REPORT NUMBER ARL-TR-3162	
9. SPONSORING/MONITORING AGENCY NAME(S) AND ADDRESS(ES)				10. SPONSOR/MONITOR'S ACRONYM(S)	
				11. SPONSOR/MONITOR'S REPORT NUMBER(S)	
12. DISTRIBUTION/AVAILABILITY STATEMENT Approved for public release; distribution is unlimited.					
13. SUPPLEMENTARY NOTES * U.S. Army Aviation and Missile Command ATTN: AMSAM-RD-SS-AT Redstone Arsenal, AL 35898					
14. ABSTRACT Viscous computational fluid dynamic simulations were used to predict the aerodynamic coefficients and flow field around a canard-controlled missile in subsonic and transonic flow. Computations were performed at Mach 0.6 and 0.9, six angles of attack between 0° and 10°, and with planar and grid tail fins. The computations were validated with wind tunnel data. Flow visualizations showed that the canard downwash produced a low-pressure region on the starboard side of the missile that produced a large induced side force. The canard trailing vortices interacted with the tail fins until $\alpha > 8^\circ$, producing a pressure differential on the leeward tail fin, leading to the adverse induced roll effects. Visualizations of the flow through the grid fin structure showed choking of the flow at Mach 0.9 and Mach 1.5. The validated simulations results showed that grid fins did not improve the canard roll-control effectiveness at subsonic and transonic speeds as well as they did at the low supersonic speed.					
15. SUBJECT TERMS computational fluid dynamics, canard, lattice fins, grid fins, roll-reversal, missile aerodynamics					
16. SECURITY CLASSIFICATION OF:			17. LIMITATION OF ABSTRACT UL	18. NUMBER OF PAGES 104	19a. NAME OF RESPONSIBLE PERSON James DeSpirito
a. REPORT UNCLASSIFIED	b. ABSTRACT UNCLASSIFIED	c. THIS PAGE UNCLASSIFIED			19b. TELEPHONE NUMBER (Include area code) 410-278-6104

Contents

List of Figures	v
List of Tables	viii
Acknowledgments	ix
1. Introduction	1
2. Computational Approach	1
2.1 Geometry and Simulation Parameters.....	1
2.2 Solver.....	4
2.3 Computational Mesh and Boundary Conditions	4
2.4 Solution Methodology.....	6
3. Results and Discussion	7
3.1 Aerodynamic Coefficients – CFD Validation.....	7
3.1.1 Supersonic Flow.....	7
3.1.2 Subsonic and Transonic Flow	9
3.2 Flow-Field Visualizations	18
3.3 Control Surface Forces.....	26
3.4 Flow-Through Grid Fins	28
4. Summary and Conclusions	35
5. References	37
Appendix A. Aerodynamic Coefficients for Planar Fin Case	39
Appendix B. Aerodynamic Coefficients for Grid Fin Case	49
Appendix C. Force Coefficients on Canards	59
Appendix D. Force Coefficients on Planar Fins	65

Appendix E. Force Coefficients on Grid Fins	71
Appendix F. Components of Aerodynamic Coefficients	77
List of Abbreviations and Symbols	86
Distribution List	88

List of Figures

Figure 1. Generic canard-controlled missile with planar fins.....	2
Figure 2. Generic canard-controlled missile with grid fins.	3
Figure 3. (a) Missile nose with canards at $\delta = 0^\circ$ and (b) front view of missile.....	3
Figure 4. Surface mesh near body–grid fin base interface.....	5
Figure 5. Mesh on missile surface and axial plane in tail region for planar fin subsonic and transonic cases.	6
Figure 6. Computed and experimental rolling moment coefficient for (a) planar fin and (b) grid fin cases in supersonic flow.....	8
Figure 7. Computed and experimental side force coefficient for (a) planar fin and (b) grid fin cases in supersonic flow.	9
Figure 8. Computed and experimental normal force coefficient for (a) planar fin and (b) grid fin cases at Mach 0.6.....	10
Figure 9. Computed and experimental pitching moment coefficient about the missile nose for (a) planar fin and (b) grid fin cases at Mach 0.6.	12
Figure 10. Computed and experimental center of pressure location from nose for (a) planar fin and (b) grid fin cases at Mach 0.6.	13
Figure 11. Computed and experimental axial force coefficient for (a) planar fin and (b) grid fin cases at Mach 0.6.....	14
Figure 12. Computed and experimental side force coefficient for (a) planar fin and (b) grid fin cases at Mach 0.6.....	15
Figure 13. Computed and experimental side force coefficient for (a) planar fin and (b) grid fin cases at Mach 0.9.....	16
Figure 14. Computed and experimental rolling moment coefficient for (a) planar fin and (b) grid fin cases at Mach 0.6.	17
Figure 15. Computed and experimental rolling moment coefficient for (a) planar fin and (b) grid fin cases at Mach 0.9.	18
Figure 16. Computed rolling moment coefficient for (a) planar fin and (b) grid fin cases at several Mach numbers.	19
Figure 17. C_p contours on planar finned missile surfaces at $M = 0.6$ and (a) $\alpha = 0^\circ$, (b) $\alpha = 4^\circ$, and (c) $\alpha = 10^\circ$	20
Figure 18. C_p contours on planar finned missile surfaces at $M = 0.9$ and (a) $\alpha = 0^\circ$, (b) $\alpha = 4^\circ$, and (c) $\alpha = 10^\circ$	21
Figure 19. C_p contours on grid finned missile surfaces at $M = 0.6$ and (a) $\alpha = 0^\circ$, (b) $\alpha = 4^\circ$, and (c) $\alpha = 10^\circ$	22
Figure 20. C_p contours on grid finned missile surfaces at $M = 0.9$ and (a) $\alpha = 0^\circ$, (b) $\alpha = 4^\circ$, and (c) $\alpha = 10^\circ$	23

Figure 21. C_p contours on (a) port side and (b) starboard side of grid finned missile surfaces at $M = 0.6$ and $\alpha = 10^\circ$	24
Figure 22. C_p surface contours and vorticity magnitude contours on cross planes at $x/d = 2, 4, \dots, 22$ for the (a) planar finned and (b) grid finned missile at $M = 0.6$ and $\alpha = 4^\circ$	25
Figure 23. C_p surface contours and vorticity magnitude contours on cross planes at $x/d = 2, 4, \dots, 22$ for the (a) planar finned and (b) grid finned missile at $M = 0.6$ and $\alpha = 10^\circ$	26
Figure 24. Side force coefficient on tail fins for (a) planar fin and (b) grid fin case for $\delta = 10^\circ$ and $M = 0.6$	27
Figure 25. Normal force coefficient on tail fins for (a) planar fin and (b) grid fin case for $\delta = 10^\circ$ and $M = 0.6$	28
Figure 26. Fin normal force slope values as a function of Mach number (δ).....	29
Figure 27. Grid fin flow field proposed in reference (6).....	30
Figure 28. C_p (a, b) and Mach number (c) contours on vertical symmetry plane with leeward grid fin geometry removed, $\alpha = 0^\circ$ and $M = 0.6$	31
Figure 29. C_p (a, b) and Mach number (c) contours on vertical symmetry plane with leeward grid fin geometry removed, $\alpha = 0^\circ$ and $M = 0.9$	32
Figure 30. C_p (a, b) and Mach number (c) contours on vertical symmetry plane with leeward grid fin geometry removed, $\alpha = 0^\circ$ and $M = 1.5$	33
Figure 31. C_p (a, b) and Mach number (c) contours on vertical symmetry plane with leeward grid fin geometry removed, $\alpha = 0^\circ$ and $M = 3.0$	34
Figure A-1. Normal force for the planar fin case at Mach 0.6.....	40
Figure A-2. Normal force for the planar fin case at Mach 0.9.....	40
Figure A-3. Side force for the planar fin case at Mach 0.6.....	41
Figure A-4. Side force for the planar fin case at Mach 0.9.....	41
Figure A-5. Axial force for the planar fin case at Mach 0.6.....	42
Figure A-6. Axial force for the planar fin case at Mach 0.9.....	42
Figure A-7. Pitching moment about the nose for the planar fin case at Mach 0.6.....	43
Figure A-8. Pitching moment about the nose for the planar fin case at Mach 0.9.....	43
Figure A-9. Pitching moment about the moment reference point (MRP) for the planar fin case at Mach 0.6.....	44
Figure A-10. Pitching moment about the MRP for the planar fin case at Mach 0.9.....	44
Figure A-11. Rolling moment for the planar fin case at Mach 0.6.....	45
Figure A-12. Rolling moment for the planar fin case at Mach 0.9.....	45
Figure A-13. Yawing moment about the nose for the planar fin case at Mach 0.6.....	46
Figure A-14. Yawing moment about the nose for the planar fin case at Mach 0.9.....	46
Figure A-15. Center of pressure location from the nose for the planar fin case at Mach 0.6.....	47
Figure A-16. Center of pressure location from the nose for the planar fin case at Mach 0.9.....	47

Figure B-1. Normal force for the grid fin case at Mach 0.6.	50
Figure B-2. Normal force for the grid fin case at Mach 0.9.	50
Figure B-3. Side force for the grid fin case at Mach 0.6.	51
Figure B-4. Side force for the grid fin case at Mach 0.9.	51
Figure B-5. Axial force for the grid fin case at Mach 0.6.	52
Figure B-6. Axial force for the grid fin case at Mach 0.9.	52
Figure B-7. Pitching moment about the nose for the grid fin case at Mach 0.6.	53
Figure B-8. Pitching moment about the nose for the grid fin case at Mach 0.9.	53
Figure B-9. Pitching moment about the moment reference point (MRP) for the grid fin case at Mach 0.6.	54
Figure B-10. Pitching moment about the MRP for the grid fin case at Mach 0.9.	54
Figure B-11. Rolling moment for the grid fin case at Mach 0.6.	55
Figure B-12. Rolling moment for the grid fin case at Mach 0.9.	55
Figure B-13. Yawing moment about the nose for the grid fin case at Mach 0.6.	56
Figure B-14. Yawing moment about the nose for the grid fin case at Mach 0.9.	56
Figure B-15. Center of pressure location from the nose for the grid fin case at Mach 0.6.	57
Figure B-16. Center of pressure location from the nose for the grid fin case at Mach 0.9.	57
Figure C-1. Canard normal force, $\delta = 10^\circ$, Mach 0.6.	60
Figure C-2. Canard normal force, $\delta = 10^\circ$, Mach 0.9.	60
Figure C-3. Canard side force, $\delta = 10^\circ$, Mach 0.6.	61
Figure C-4. Canard side force, $\delta = 10^\circ$, Mach 0.9.	61
Figure C-5. Canard axial force, $\delta = 10^\circ$, Mach 0.6.	62
Figure C-6. Canard axial force, $\delta = 10^\circ$, Mach 0.9.	62
Figure D-1. Planar fin normal force, $\delta = 10^\circ$, Mach 0.6.	66
Figure D-2. Planar fin normal force, $\delta = 10^\circ$, Mach 0.9.	66
Figure D-3. Planar fin side force, $\delta = 10^\circ$, Mach 0.6.	67
Figure D-4. Planar fin side force, $\delta = 10^\circ$, Mach 0.9.	67
Figure D-5. Planar fin axial force, $\delta = 10^\circ$, Mach 0.6.	68
Figure D-6. Planar fin axial force, $\delta = 10^\circ$, Mach 0.9.	68
Figure E-1. Grid fin normal force, $\delta = 10^\circ$, Mach 0.6.	72
Figure E-2. Grid fin normal force, $\delta = 10^\circ$, Mach 0.9.	72
Figure E-3. Grid fin side force, $\delta = 10^\circ$, Mach 0.6.	73
Figure E-4. Grid fin side force, $\delta = 10^\circ$, Mach 0.9.	73
Figure E-5. Grid fin axial force, $\delta = 10^\circ$, Mach 0.6.	74

Figure E-6. Grid fin axial force, $\delta = 10^\circ$, Mach 0.9.....	74
Figure F-1. Components of normal force for the planar fin case, $\delta = 10^\circ$, Mach 0.6.....	78
Figure F-2. Components of normal force for the planar fin case, $\delta = 10^\circ$, Mach 0.9.....	78
Figure F-3. Components of normal force for the grid fin case, $\delta = 10^\circ$, Mach 0.6.	79
Figure F-4. Components of normal force for the grid fin case, $\delta = 10^\circ$, Mach 0.9.	79
Figure F-5. Components of side force for the planar fin case, $\delta = 10^\circ$, Mach 0.6.	80
Figure F-6. Components of side force for the planar fin case, $\delta = 10^\circ$, Mach 0.9.	80
Figure F-7. Components of side force for the grid fin case, $\delta = 10^\circ$, Mach 0.6.	81
Figure F-8. Components of side force for the grid fin case, $\delta = 10^\circ$, Mach 0.9.	81
Figure F-9. Components of axial force for the planar fin case, $\delta = 10^\circ$, Mach 0.6.	82
Figure F-10. Components of axial force for the planar fin case, $\delta = 10^\circ$, Mach 0.9.	82
Figure F-11. Components of axial force for the grid fin case, $\delta = 10^\circ$, Mach 0.6.....	83
Figure F-12. Components of axial force for the grid fin case, $\delta = 10^\circ$, Mach 0.9.....	83

List of Tables

Table 1. Canard and fin characteristics.....	3
Table C-1. Aerodynamic coefficients on canards, planar fin case, $\delta = 10^\circ$, Mach 0.6.	63
Table C-2. Aerodynamic coefficients on canards, planar fin case, $\delta = 10^\circ$, Mach 0.9.	63
Table D-1. Aerodynamic coefficients on planar fins, $\delta = 10^\circ$, Mach 0.6.....	69
Table D-2. Aerodynamic coefficients on planar fins, $\delta = 10^\circ$, Mach 0.9.....	69
Table E-1. Aerodynamic coefficients on grid fins, $\delta = 10^\circ$, Mach 0.6.....	75
Table E-2. Aerodynamic coefficients on grid fins, $\delta = 10^\circ$, Mach 0.9.....	75
Table F-1. Components of aerodynamic coefficients, planar fin case, $\delta = 10^\circ$, Mach 0.6.....	84
Table F-2. Components of aerodynamic coefficients, planar fin case, $\delta = 10^\circ$, Mach 0.9.....	84
Table F-3. Components of aerodynamic coefficients, grid fin case, $\delta = 10^\circ$, Mach 0.6.	85
Table F-4. Components of aerodynamic coefficients, grid fin case, $\delta = 10^\circ$, Mach 0.9.	85

Acknowledgments

The authors thank Richard Angelini, U.S. Army Research Laboratory (ARL), for providing scientific visualizations of the flow fields, and Eric Fournier, Defence Research and Development Canada–Valcartier, for providing discussions on the wind tunnel data. This work was supported in part by a grant of high-performance computing time from the U.S. Department of Defense High Performance Computing Modernization program at the ARL Major Shared Resource Center, Aberdeen Proving Ground, MD.

INTENTIONALLY LEFT BLANK.

1. Introduction

Missile concepts with forward control fins, or canards, have been used for many years. However, previous studies have shown that concepts with canards can suffer from adverse induced rolling moments (1–4). The use of grid fins, or “lattice controls,” for the tail control surfaces instead of conventional planar fins was proposed by the U.S. Army Aviation and Missile Command (AMCOM) personnel as a possible remedy for the roll control problems (5). A grid fin is an unconventional lifting and control surface that consists of an outer frame supporting an inner grid of intersecting planar surfaces of small chord (6). Computational fluid dynamics (CFD) techniques to calculate the viscous flow around a missile with grid fins were recently demonstrated (7, 8).

The present study extends an earlier CFD investigation of the adverse roll effects of canards on a missile with both conventional planar fins and grid fins in supersonic flow (9, 10). The supersonic CFD investigation, validated with data from an earlier wind tunnel investigation (5), confirmed that grid fins alleviate the adverse roll effects at low supersonic speed. The CFD compliments the wind tunnel data by providing the ability to visualize the flow field to aid in understanding the flow physics responsible for the adverse forces and moments. The CFD calculations also provide the forces on each individual canard and fin, which were not measured in the wind tunnel. The present work extends the CFD database to include subsonic and transonic flow. Wind tunnel results showed that grid fins are not as effective in alleviating the adverse rolling moments at subsonic and transonic speeds. The CFD provides insight into the flow physics responsible for the difference in effectiveness and may help in designing a grid fin that will be more effective for roll control at lower speeds.

2. Computational Approach

2.1 Geometry and Simulation Parameters

The investigation used CFD to determine the flow field and aerodynamic coefficients on a 16-cal., four-finned, generic canard-controlled missile. The study followed an experimental wind tunnel investigation performed by AMCOM and the Defence Research and Development–Valcartier, formerly the Defence Research Establishment–Valcartier (DREV), Canada (5). The DREV wind tunnel is an intermittent, in-draft wind tunnel with a 0.6- × 0.6-m test section. In this type of tunnel, the air flows from an atmospheric pressure tank to a vacuum tank, and the Reynolds number is lower than free-flight values at high Mach numbers. The wind tunnel Reynolds number ranges from $\sim 1.56 \times 10^7 \text{ m}^{-1}$ at $M = 1.15$ to $4.7 \times 10^6 \text{ m}^{-1}$ at $M = 4.0$.

The wind tunnel model geometry was used in the CFD study. Four canards on the ogive were in-line with the fins. Two fin types were investigated: conventional planar fins and grid fins. Figures 1–2 show the geometry for the planar fin and grid fin cases, respectively. The missile has a 3.7-cal.-long truncated tangent ogive with a hemispherical nose and a 12.3-cal. long body. The canard midchord is located 0.96 cal. from the missile nose, and the fin midchord is located 1.5 cal. from the missile base. The canards (figure 3a) have a double-wedge, trapezoidal planform with a span of 0.37 cal., a root chord of 0.36 cal., a tip chord of 0.13 cal., a midchord root thickness of 0.03 cal., and a taper ratio of 1.48. The planar fins have a double wedge, rectangular planform with a span of 0.78 cal., a chord of 0.65 cal., and a mid-chord thickness of 0.03 cal. The grid fins (figure 3b) consist of 23 cubic and 12 prismatic cells with a span of 0.74 cal., a chord of 0.10 cal., and a thickness of 0.46 cal. The web thickness between the grid fin cells is 0.003 cal. The canard and fin characteristics are summarized in table 1.

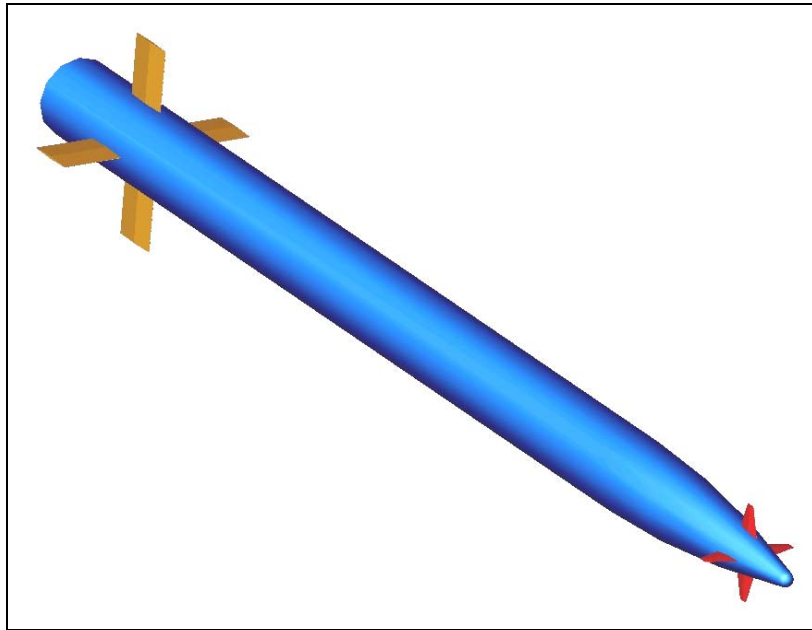


Figure 1. Generic canard-controlled missile with planar fins.

The analyses were performed at two Mach numbers: $M = 0.6$ and 0.9 , with one canard deflection: $\delta = 10^\circ$, and at six angles of attack: $\alpha = 0, 2, 4, 6, 8,$ and 10° . The DREV wind tunnel conditions were used in this study. For $M = 0.6$, the freestream conditions were a Reynolds number of $1.01 \times 10^7 \text{ m}^{-1}$, a static temperature of 284 K, and a static pressure of $7.66 \times 10^4 \text{ Pa}$. For $M = 0.9$, the freestream conditions were a Reynolds number of $1.40 \times 10^7 \text{ m}^{-1}$, a static temperature of 255 K, and a static pressure of $5.62 \times 10^4 \text{ Pa}$. The model reference diameter (D) was 30 mm, and the moment reference point (MRP) was 10.63 cal. aft of the missile nose. The simulations were performed with the missile in the cruciform (+) configuration. The DREV wind tunnel data ranged from 4 to $+15^\circ$ angle of attack. In the 10° canard deflection case, all four canards were deflected in the same direction, intended to give a positive roll, which by convention was clockwise when viewed from the rear of the missile.

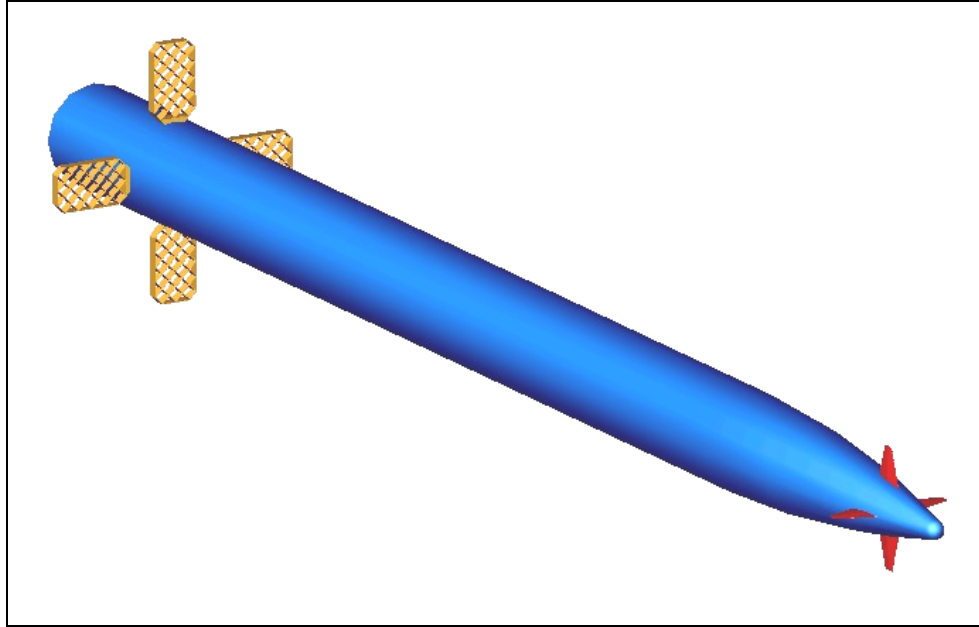


Figure 2. Generic canard-controlled missile with grid fins.

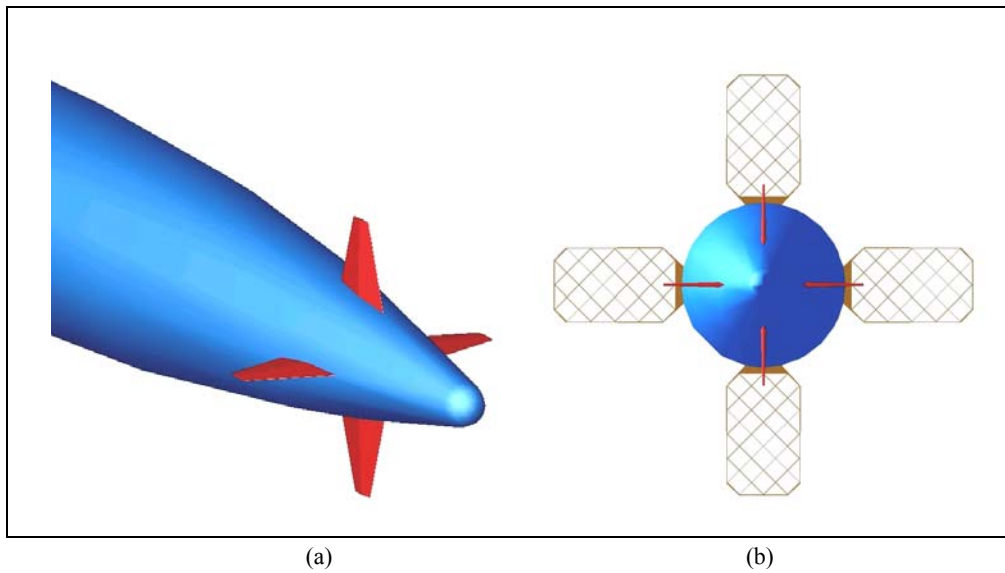


Figure 3. (a) Missile nose with canards at $\delta = 0^\circ$ and (b) front view of missile.

Table 1. Canard and fin characteristics.

Control Type	Span (cal.)	Root Chord (cal.)	Tip Chord (cal.)	Root Thickness (cal.)	Taper Ratio	Web (cal.)
Canard	0.37	0.36	0.13	0.03	1.48	—
Planar fin	0.78	0.65	0.65	0.03	1.0	—
Grid fin	0.74	0.10	0.10	0.46	1.0	0.003

2.2 Solver

Steady-state calculations were used to compute the flow field using the commercial CFD code, FLUENT (v6.0) (11). The implicit, compressible, unstructured-mesh solver was used. The three-dimensional (3-D), time-dependent, Reynolds-Averaged Navier-Stokes (RANS) equations are solved using the finite volume method:

$$\frac{\partial}{\partial t} \int_V \mathbf{W} dV + \oint [F - G] \cdot d\mathbf{A} = \int_V \mathbf{H} dV, \quad (1)$$

where

$$\mathbf{W} = \begin{Bmatrix} \rho \\ \rho u \\ \rho v \\ \rho w \\ \rho E \end{Bmatrix}, \quad \mathbf{F} = \begin{Bmatrix} \rho \mathbf{v} \\ \rho v u + p \mathbf{i} \\ \rho v v + p \mathbf{j} \\ \rho v w + p \mathbf{k} \\ \rho \mathbf{v} E + p \mathbf{v} \end{Bmatrix}, \quad \mathbf{G} = \begin{Bmatrix} 0 \\ \boldsymbol{\tau}_{xi} \\ \boldsymbol{\tau}_{yi} \\ \boldsymbol{\tau}_{zi} \\ \boldsymbol{\tau}_{ij} v_j + \mathbf{q} \end{Bmatrix}. \quad (2)$$

The inviscid flux vector \mathbf{F} is evaluated by a standard upwind flux-difference splitting. In the implicit solver, each equation in the coupled set of governing equations is linearized implicitly with respect to all dependent variables in the set, resulting in a block system of equations. A block Gauss-Seidel, point implicit linear equation solver is used with an algebraic multigrid method to solve the resultant block system of equations. The coupled set of governing equations is discretized in time, and time marching proceeds until a steady-state solution is reached. In the implicit scheme, which was used in this study, an Euler-implicit discretization in time is combined with a Newton-type linearization of the fluxes.

A modified form of the k - ϵ two-equation turbulence model was used in this study. Called the “realizable” k - ϵ model in FLUENT, it differs from the standard k - ϵ model in that it contains a new formulation for the turbulent viscosity and a new transport equation for the dissipation rate, which was derived from an exact equation for the transport of the mean-square vorticity fluctuation (12). The term “realizable” means that the model satisfies certain mathematical constraints on the Reynolds stresses consistent with turbulent flow physics. The realizable k - ϵ model has shown substantial improvements over the standard k - ϵ model where flow features include strong streamline curvature, vortices, and rotation (11).

2.3 Computational Mesh and Boundary Conditions

The geometry and unstructured mesh were generated using the preprocessor, GAMBIT, supplied in the FLUENT software suite. Canard deflection and angle of attack precluded the use of symmetry or periodicity, so a full 3-D mesh was required. In generating the meshes, boundary layer mesh spacing was used near the missile body and fin surfaces. The enhanced wall treatment option, new in FLUENT v6.0, was used. The enhanced wall treatment option uses the two-layer model when the viscous layer is resolved by the grid and enhanced wall functions

when the grid is too coarse to resolve the viscous layer. The first point off the surface (cell center) was $\sim 7.0 \times 10^{-5}$ cal., chosen to give a y^+ value of ~ 1.0 . This could not be achieved on the surfaces of the grid fins, as will be discussed, but with the new enhanced wall treatment option, the near wall turbulence should still be modeled appropriately. All mesh stretching ratios were uniform and were kept below 1.25. At $M = 3.0$ (thinnest boundary layer), there were ~ 32 cells in the boundary layer, with ~ 11 cells in the viscous sublayer. About 144 cells were used on the missile body in the circumferential direction, with this value increased in the grid fin region (figure 4).

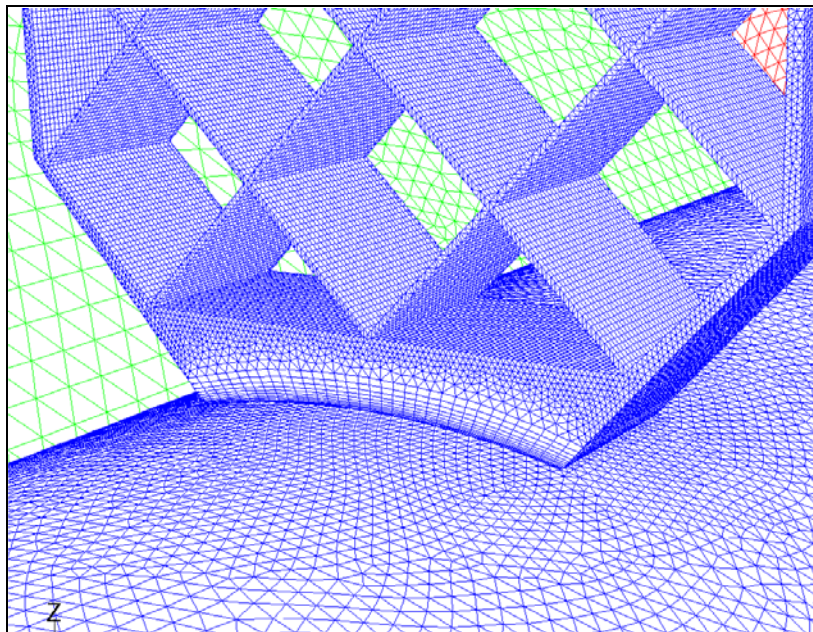


Figure 4. Surface mesh near body-grid fin base interface.

An all-hexahedral (hex) mesh was used for the planar fin case, while a hybrid hex and tetrahedral (tet) mesh with triangular prism layers were used for the grid fin case. O-grid type meshes were generated around the canards and planar fins. The first 13 cal. of the missile was meshed with the same type hex mesh in both tail fin cases. A tet mesh was used in the tail region (figure 4) in order to mesh the complicated grid fin structure. Layers of triangular prisms were used on the body to capture the boundary layer. The tet mesh in the tail was matched to the forward hex mesh via a layer of pyramidal cells. Due to meshing constraints, prism layers were not used around the grid fins, and the spacing of the first point off the grid fin surfaces was larger than desired. Postprocessing of the runs showed that the y^+ value was in the range of 1–1.8 on the missile body, less than 1.0 on the canards and planar fins, and between 10 and 20 on the grid fins. Similar y^+ values were observed in the supersonic cases. However, the supersonic runs were performed with a previous version of FLUENT, without the enhanced wall treatment. In those cases, some loss of accuracy of the flow calculation near the grid fin surfaces was expected.

The subsonic cases require a mesh that extends farther from the missile surface than the supersonic cases. An “outer” mesh was generated around the previous meshes used for the supersonic cases. This mesh extended 50 cal. ahead of and behind, and 66 cal. radially from the missile surface. The outer mesh added ~2.0 million cells to the planar fin case and ~1.6 million cells to the grid fin case. The total sizes of the planar and grid tail fin meshes were ~6.9 and 17.3 million cells, respectively. Figure 5 shows the tail region of the mesh used for the planar fin subsonic cases.

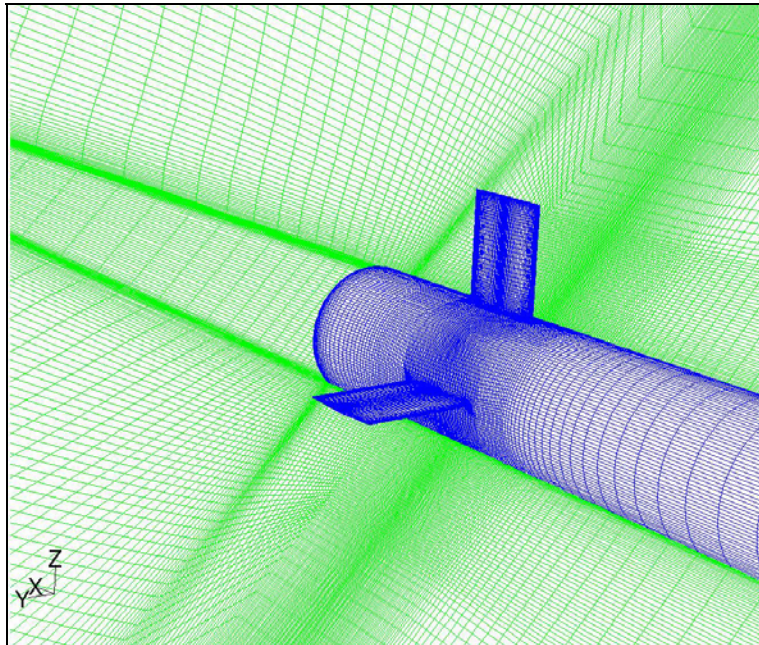


Figure 5. Mesh on missile surface and axial plane in tail region for planar fin subsonic and transonic cases.

A far-field pressure boundary condition was used at the downstream, upstream, and outer radial boundary. A no-slip, adiabatic wall boundary condition was used for all solid surfaces.

2.4 Solution Methodology

The simulations were performed in parallel on a Silicon Graphics, Inc. (SGI) Origin 3800 with R12000 processors and an IBM SMP P3 with Power3 processors. The simulations were run with the single precision solver, with a maximum Courant-Friedrich-Lewy (CFL) number of 7. Each case was started with a CFL of 1.0 and ramped up to the maximum during the first few hundred iterations. Mesh adaption was used in the supersonic cases (9, 10) to show mesh independence and no further mesh adaption was used in the subsonic cases.

The calculations took ~300–600 μ s/cell/iteration of CPU time, using 48 processors for the planar fin cases and 64 processors for the grid fin cases. For example, solving the grid fin case with 64 processors took ~81–162 s of CPU time per iteration. Convergence was determined by tracking

the change in the flow residuals and the aerodynamic coefficients during the solution. The solution was deemed converged when the flow residuals had stabilized and the aerodynamic coefficients were changing $<0.5\%$ after the last 100 iterations. The aerodynamic coefficients converged in ~ 2700 – 4600 iterations. The normalized residuals were reduced at least 3 orders of magnitude.

3. Results and Discussion

3.1 Aerodynamic Coefficients – CFD Validation

In this section, the results of the supersonic cases from the previous study are first summarized, followed by the subsonic results from the current study. The axial force, normal force, side force, rolling moment, and pitching moment are presented in missile-based coordinates. This is a right-handed system with the x axis coinciding with the missile axis and oriented to the rear, the y axis oriented to the missile's starboard side, and the z axis oriented upward. The forces are positive when coinciding with the positive coordinate axes. The rolling moment is positive when the roll is clockwise when looking forward from the aft end of the missile. The yawing moment is positive when the nose is moving right, and the pitching moment is positive when the nose is moving upward. The reference area is the cross-sectional area of the missile base, and the reference length is the diameter of the missile. The calculated coefficients are compared to wind-tunnel measurements performed at DREV (5).

3.1.1 Supersonic Flow

In the previous study, very good agreement was found between all the experimental and calculated aerodynamic coefficients (9, 10). The CFD accurately captured the adverse roll phenomenon, shown in figure 6. For the planar fin case at $M = 1.5$, C_l is negative (opposite the intended roll due to the canard deflection) at $\alpha = 0^\circ$. C_l decreases as α increases to $\sim 6^\circ$, then C_l increases, becoming positive at $\sim 8^\circ$. For the grid fin case at $M = 1.5$, C_l is now positive at $\alpha = 0^\circ$, decreasing to near 0 between $4^\circ < \alpha < 7^\circ$ (where roll control is substantially reduced but not reversed). At the higher Mach number, C_l is always positive and is similar for both types of fins. Flow visualizations of the computed results showed that the canard trailing vortices interact with the tail fins—primarily the leeward tail fin—and affect the roll control effectiveness of the canards.

The intensity of the canard trailing vortices is much lower at Mach 3.0, so there is little effect on the roll control effectiveness of the canards. At Mach 1.5, a pressure differential is generated on the leeward planar fin that counteracts the rolling moment generated by the canards. The flow interacts with the grid fins differently, not generating as large a side force on the leeward fin, and thus not reducing the roll control effectiveness of the canards as much as in the planar fin case.

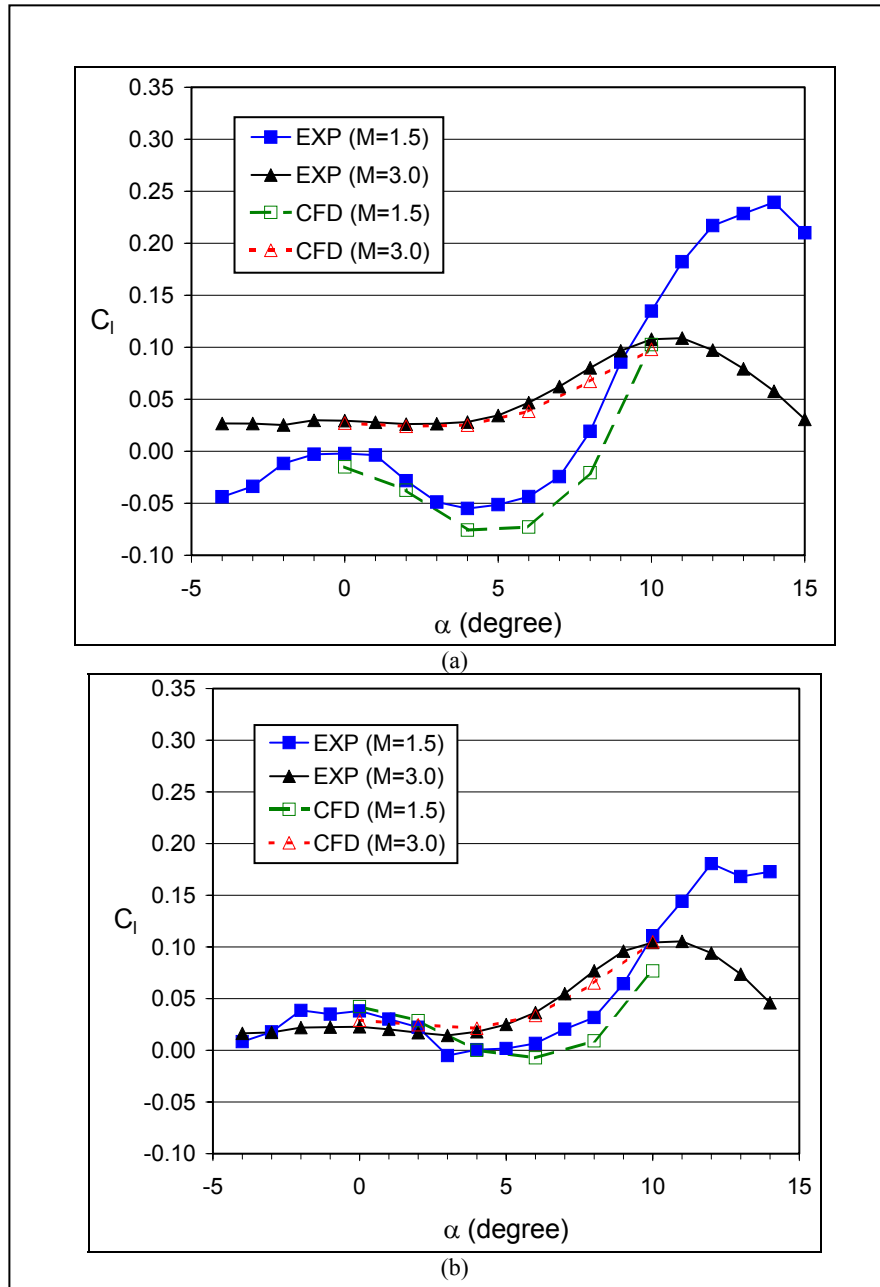


Figure 6. Computed and experimental rolling moment coefficient for (a) planar fin and (b) grid fin cases in supersonic flow.

Figure 7 shows the side force coefficient for both tail fin types. Again, there is little difference between the two fin types at the higher Mach number, and the maximum C_y is not too large. However, at the lower supersonic Mach number, the side force acting on the planar fins is ~ 5 times larger than at the higher Mach number. Flow visualizations (10) of the computed results showed that the flow field induced by the deflected canards generated a higher velocity, and thus a lower pressure, on the starboard side of the missile, thereby generating the side force. The effect increased with angle of attack. There is little effect of the type of tail fin on the induced side force.

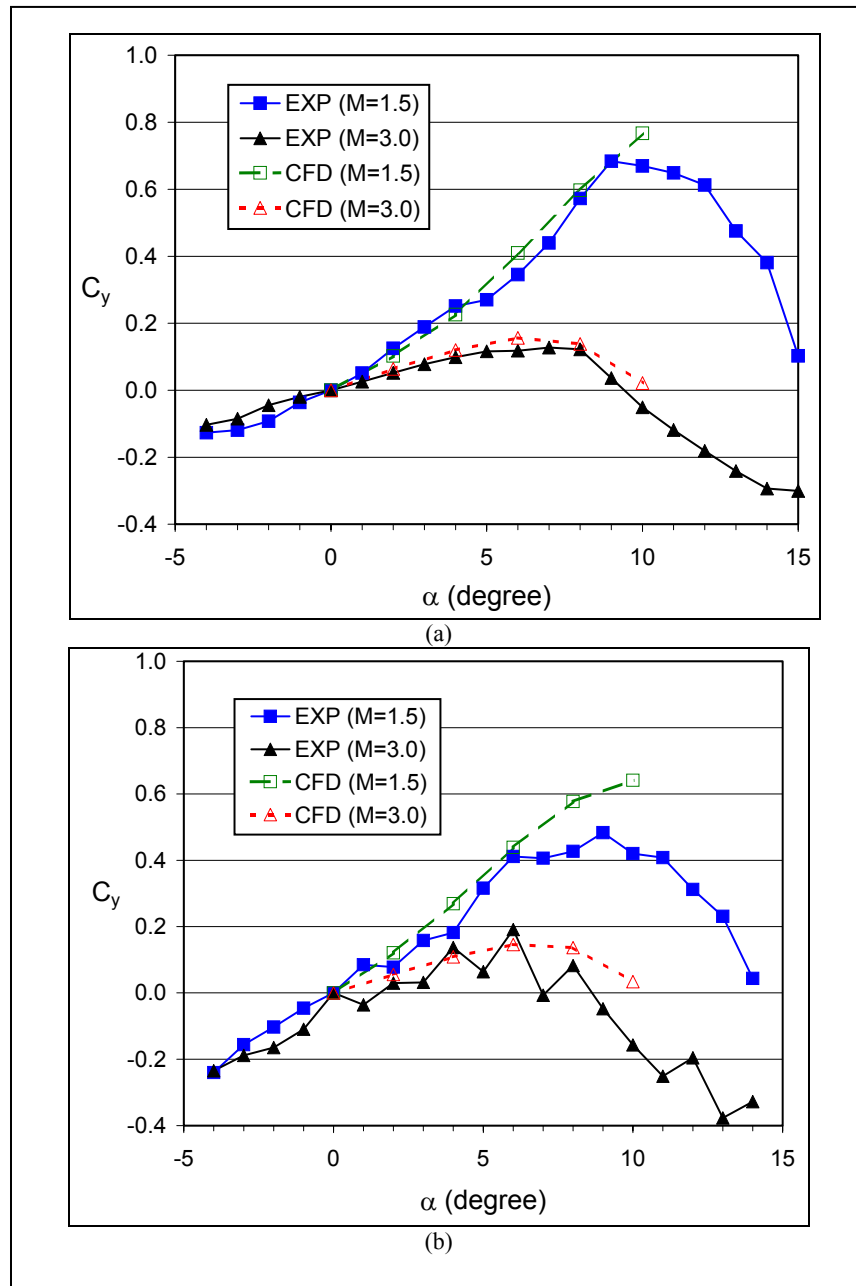


Figure 7. Computed and experimental side force coefficient for (a) planar fin and (b) grid fin cases in supersonic flow.

3.1.2 Subsonic and Transonic Flow

The computed aerodynamic coefficients show very good agreement with the experimental values in general. Figure 8 shows the computed and experimental normal force coefficient vs. α for both tail fin cases at $M = 0.6$. The CFD predictions compare very well to the measured C_z . Also shown is a prediction from the AP98 aeroprediction code (13) for the planar fin case. AP98 is an engineering code based on empirical and theoretical methods. Grid fins are not modeled by the AP98 code. The comparison of the CFD and AP98 predictions is excellent up to $\sim \alpha = 6^\circ$, where AP98 predicts a higher C_z . The difference between the computed and measured C_z at

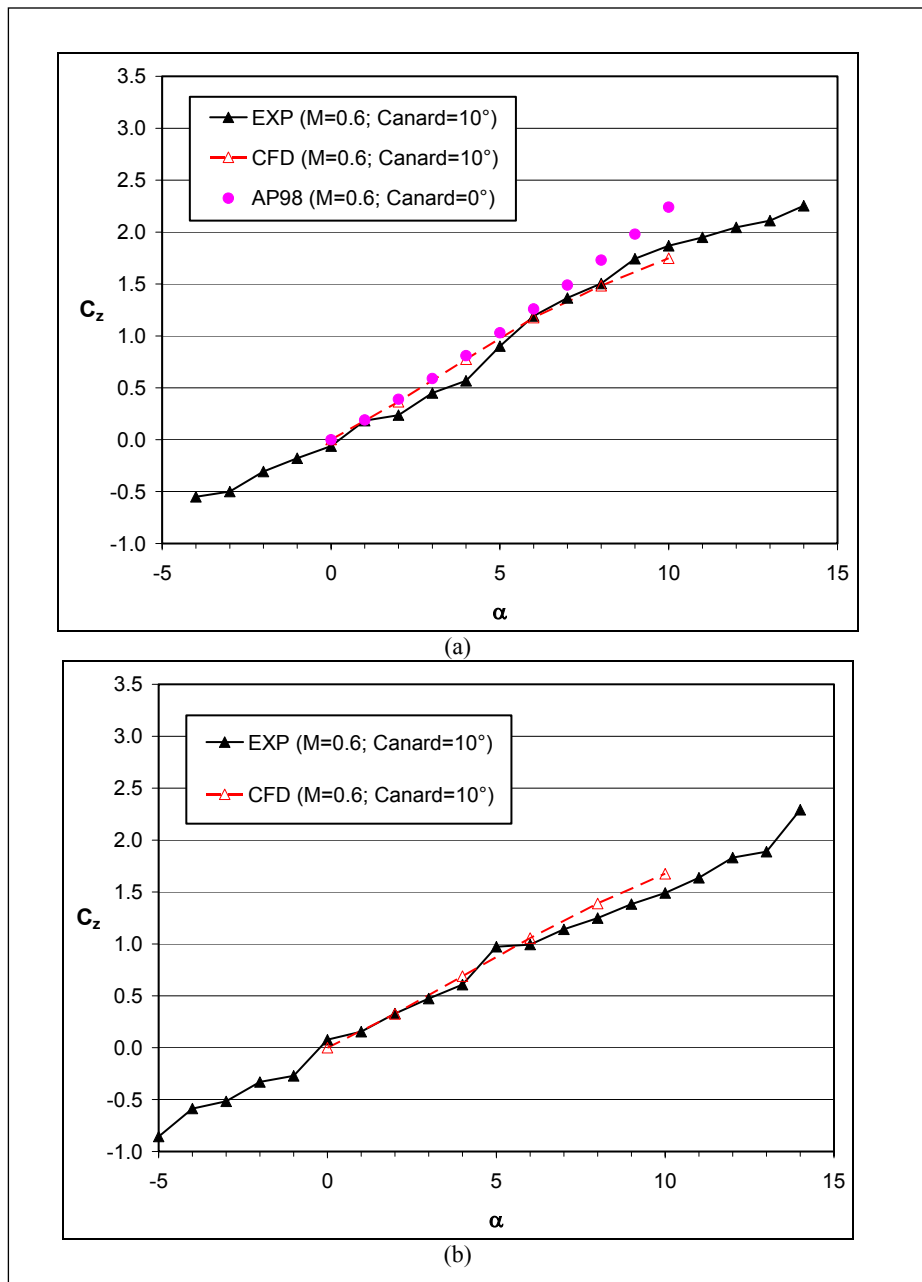


Figure 8. Computed and experimental normal force coefficient for (a) planar fin and (b) grid fin cases at Mach 0.6.

$\alpha = 10^\circ$ was 9.4% in the planar fin case (figure 8a) and 12.4% in the grid fin case (figure 8b). Note that the CFD predicts a lower normal force for the planar fin case and a higher normal force for the grid fin case. The C_z predicted by the CFD is very similar for both tail fin cases (4% at $\alpha = 10^\circ$), which is expected since the two types of fins were designed to give the same static stability. However, the two experimental C_z values differ by 23% at $\alpha = 10^\circ$.

The experimental data shown in these plots are data supplied by DREV. A second-order polynomial regression routine was used on the raw data to get values at regular, 1° , intervals of

α . This routine did not alter the generally nonsmooth character of the original raw experimental data. Biases in the data were also removed in some cases by zeroing the $\alpha = 0^\circ$ value. The sometimes “wiggly” nature of the experimental data makes it impractical to quantify the difference between the predicted and measured data at all values of α . In fact, one of the observations of the wind tunnel test data was that a significant amount of scatter exists in the data below $M = 1.28$ and that these data should be used with caution (5). Therefore, rather than state the maximum numerical difference, the percent difference will be stated where the qualitative trend of the curves have obviously diverged. For example, in figure 8a, the predicted values are linear in the range $0^\circ < \alpha < 5^\circ$ while the experimental values have moved lower. The maximum difference between the predicted and measured values is at $\alpha = 2^\circ$ and 4° (23%). However, the divergence of the predicted and measured values at $\alpha > 8^\circ$ may be a more important trend, and so the difference at $\alpha = 10^\circ$ was stated as previously mentioned.

The predicted and measured pitching moment coefficients (about missile nose) at $M = 0.6$ are shown in figure 9. The trends are similar to those observed for C_z . At $\alpha = 10^\circ$, the CFD predictions for the two types of tail fins differ by 5.4%, while the experimental values differ by 32.5%. The AP98 prediction (figure 9a) falls close to the experimental values, but this is due to the higher prediction of C_z by AP98.

Figure 10 shows the measured and computed center of pressure location, aft of the missile nose, for both tail fin types at $M = 0.6$. At $\alpha = 10^\circ$, the CFD predictions for the two types of tail fins differ by 1.3%, while the experimental values differ by 10.2%. The CFD, AP98, and measured values for the planar fin case compare very well. The calculation of x_{cp} is indeterminate at $\alpha = 0^\circ$, so the experimental and CFD data should be disregarded at this location.

The predicted and measured total axial force coefficients at $M = 0.6$ are shown in figure 11. This value includes the force on the missile base. The CFD predicted and measured values compare well for the planar fin case (figure 11a), with differences of 4%–7.3%. The variation with α is also similar. The AP98 prediction has the opposite trend with α , but the values are within 8% of the CFD predictions. The CFD predicted values of C_x vary between 0.38 and 0.40, while the measured values vary between 0.35 and 0.38. In the grid fin case (figure 11b), the predicted values of C_x are 16%–18% higher than the measured values. The trend with α is predicted very well. The predicted values of C_x vary between 0.64 and 0.71, while the measured values vary between 0.55 and 0.60. The C_x in the grid fin case is ~ 1.5 – 1.7 times that in the planar fin case. These differences and trends are similar to those observed in the supersonic cases. The axial force for the grid fin case is expected to be higher than that for the planar fin case. However, as noted for the supersonic cases (9, 10), the drag of the grid fins on this model is larger than could be achieved with an “optimum” design. Primarily, because of the small size of the wind tunnel model, the web thickness of the fin elements could not be scaled down to the proper design thickness due to machining limitations. The web is ~ 1.5 times larger than optimum.

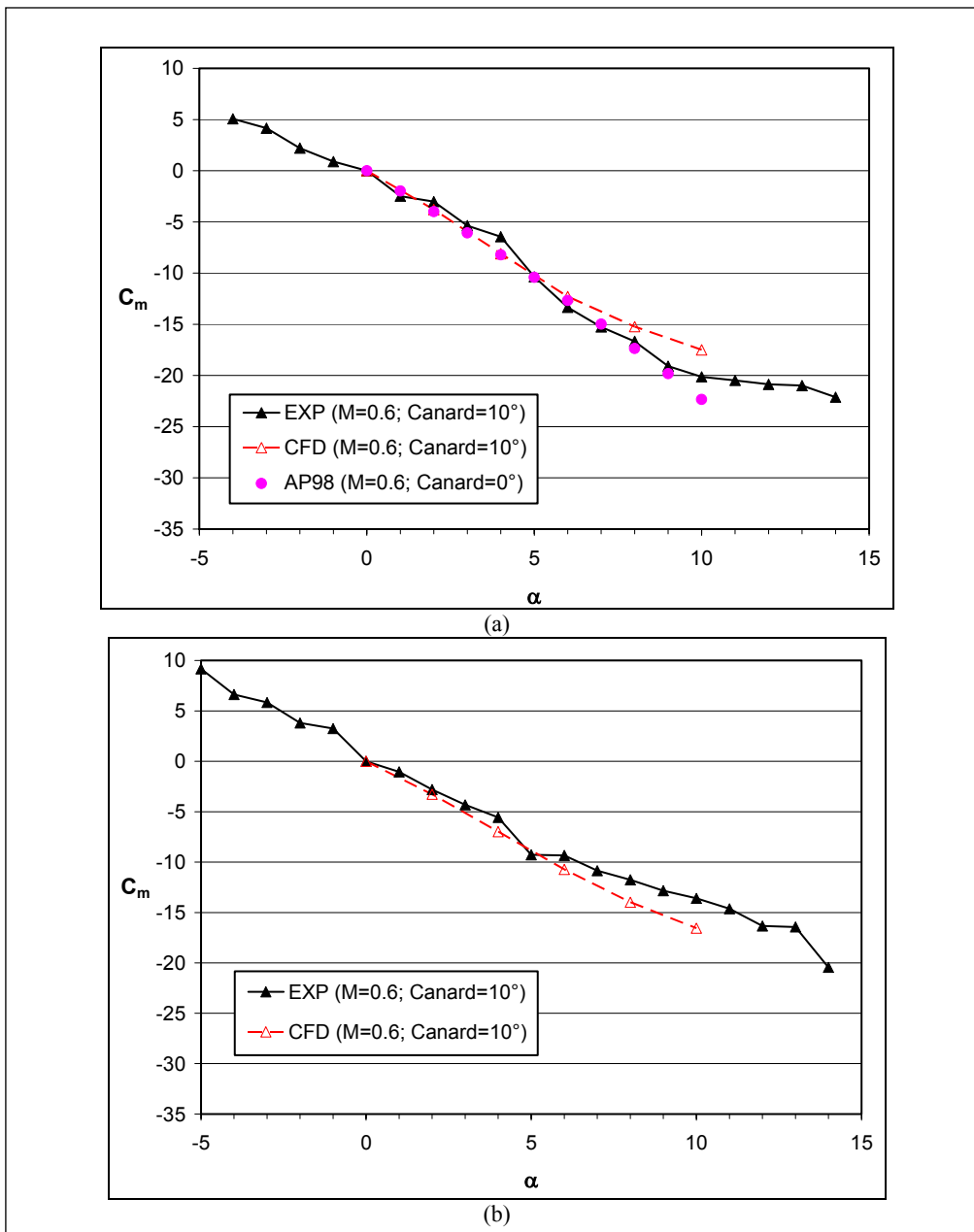


Figure 9. Computed and experimental pitching moment coefficient about the missile nose for (a) planar fin and (b) grid fin cases at Mach 0.6.

The results at $M = 0.9$ were very similar to the results at $M = 0.6$ for the aerodynamic coefficients shown thus far. These results are not presented here, but they are included in appendices A and B.

The most important objective of this study was to accurately predict the adverse induced rolling moment and side forces observed in the wind tunnel experiments. Validation of these components gives confidence to the flow visualizations obtained from the CFD. Figure 12 compares the predicted and measured side force coefficients for the two tail fin types at $M = 0.6$.

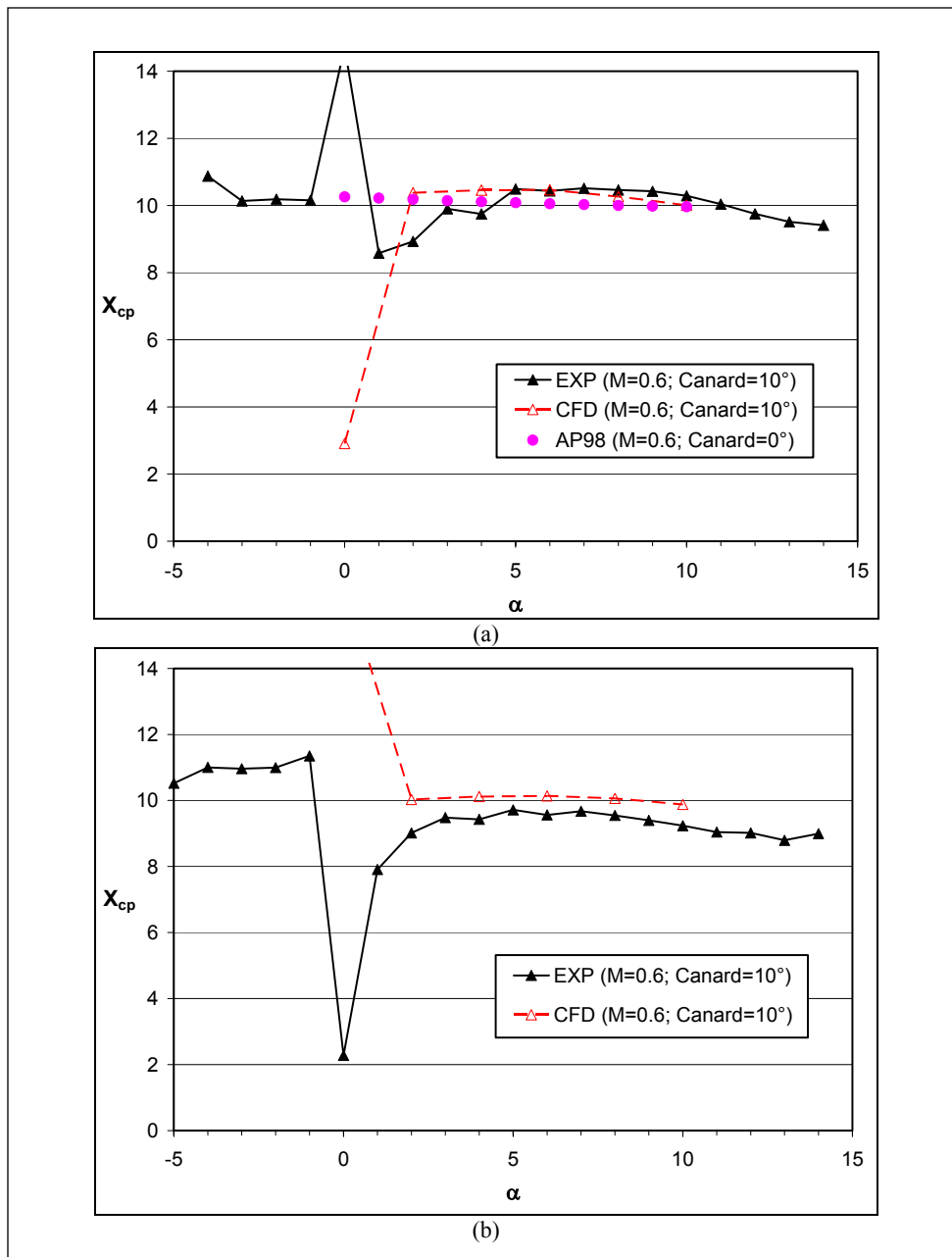


Figure 10. Computed and experimental center of pressure location from nose for (a) planar fin and (b) grid fin cases at Mach 0.6.

The predicted values are in relatively good agreement, considering that the experimental data are not very smooth. The level of induced side force is similar for both tail fin types. Flow visualizations showed a similar effect as in the supersonic case, with the flow past the deflected canards generating a low-pressure region on the starboard side of the missile.

The comparison of the predicted and measured C_y at $M = 0.9$ is shown in figure 13. The agreement is excellent in the planar fin case (figure 13a), capturing an inflection in the data at $\sim \alpha = 4^\circ$. There was only a moderate difference (8%) between the predicted and measured values at $\alpha = 10^\circ$. The predicted data in the grid fin case are similar to the predicted data in the

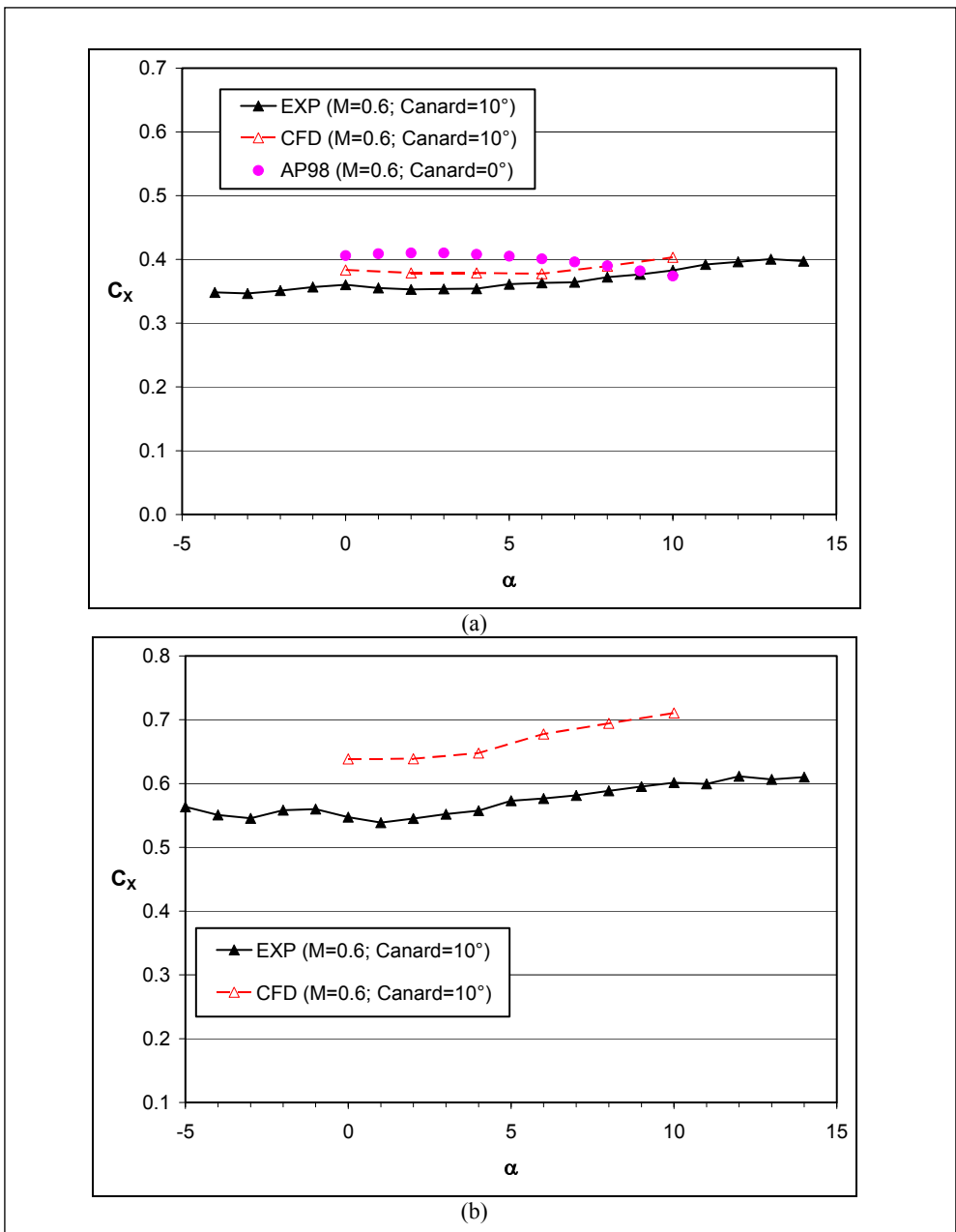


Figure 11. Computed and experimental axial force coefficient for (a) planar fin and (b) grid fin cases at Mach 0.6.

planar fin case; however, the validity of the experimental data between $0^\circ < \alpha < 4^\circ$ is questionable.

The predicted and measured rolling moment coefficients at $M = 0.6$ are compared in figure 14. The agreement between the predicted and measured values of C_l in the planar fin case (figure 14a) is very good. The agreement at $\alpha = 0^\circ$ is not good, but the experimental data are questionable for $-5^\circ < \alpha < 0^\circ$. In the grid fin case (figure 14b), the shape of the curves match, but appear offset, with the predicted values lagging the measured values. However, the predicted C_l

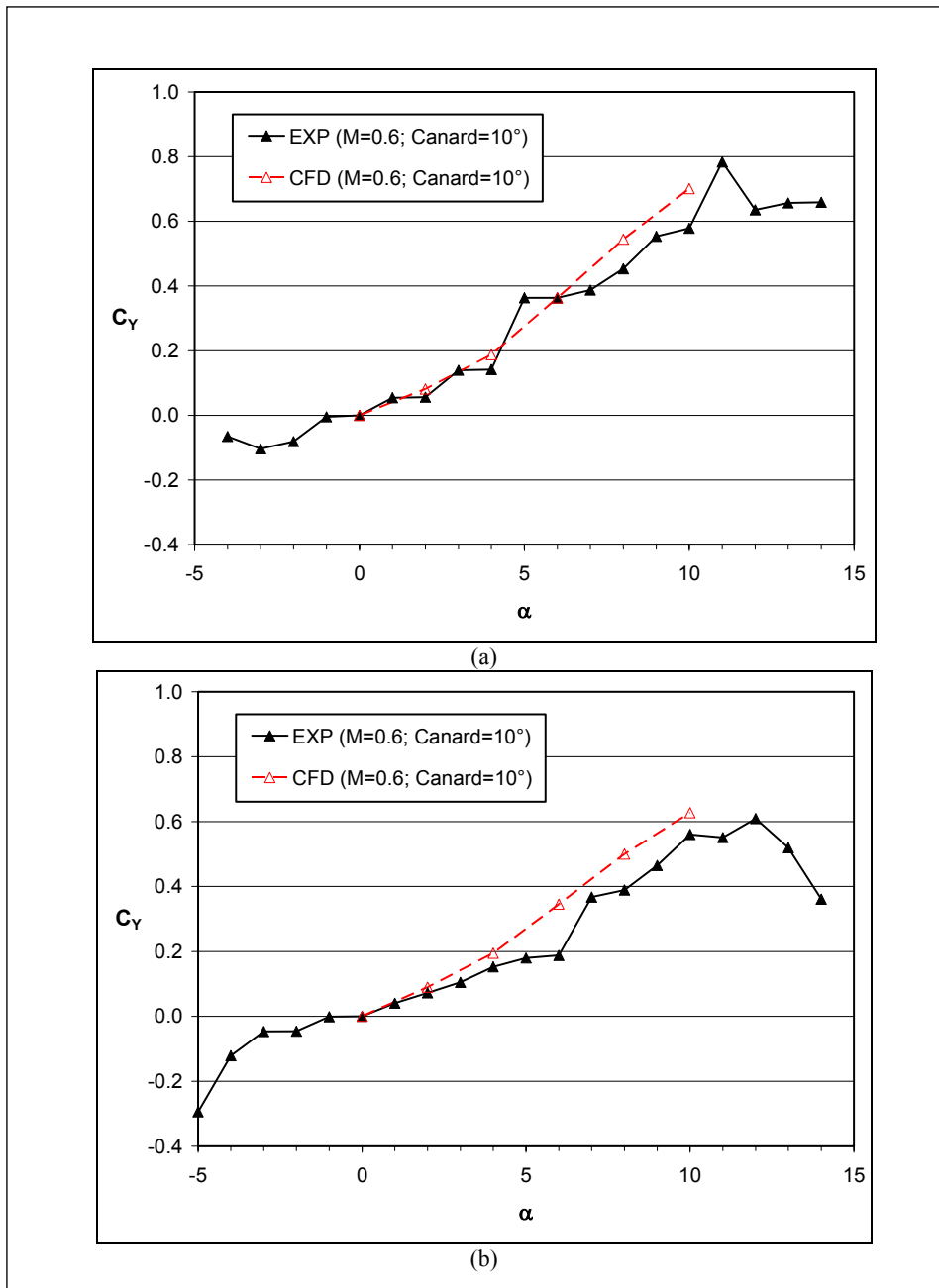


Figure 12. Computed and experimental side force coefficient for (a) planar fin and (b) grid fin cases at Mach 0.6.

indicates that the grid fins improves the roll control effectiveness of the canards (higher C_l) at $\alpha = 0^\circ$, whereas no improvement is shown in the measured values. The measured C_l for $\alpha > 0^\circ$ is similar for both fin types. The predicted C_l shows that the grid fins improve the canard roll control effectiveness for $0^\circ < \alpha < 4^\circ$, while slightly reducing it for $5^\circ < \alpha < 10^\circ$.

The comparison of the predicted and measured C_l at $M = 0.9$ is shown in figure 15. The general trends are similar to those observed at $M = 0.6$, with the measures C_l higher than the predicted value for the planar fin case at $\alpha = 0^\circ$ and the predicted values lagging the experimental values

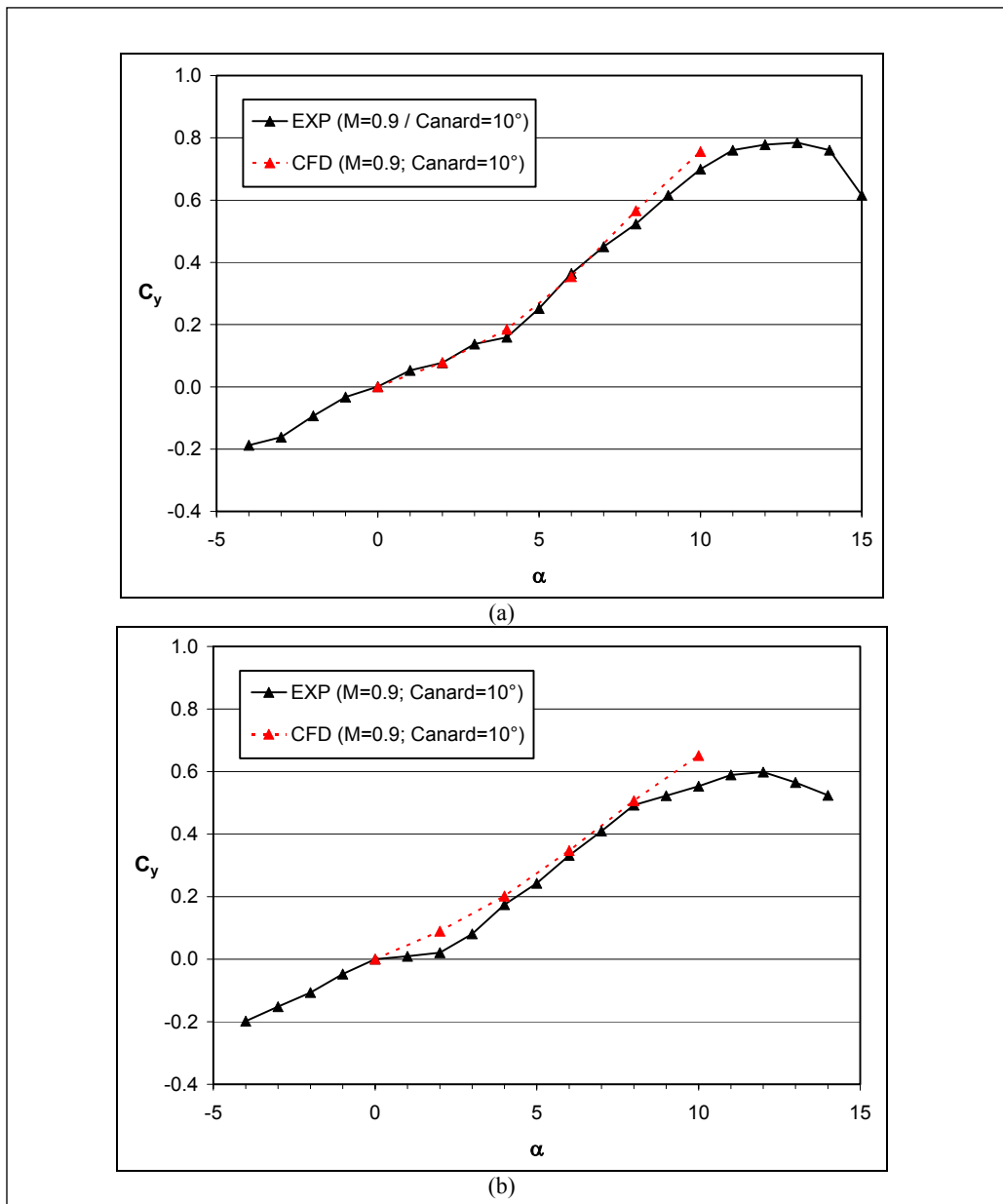


Figure 13. Computed and experimental side force coefficient for (a) planar fin and (b) grid fin cases at Mach 0.9.

for the grid fin case. The predicted values for the planar fin case (figure 15a) do not follow as smooth a trend as in the other cases, but the trend is still similar to those other cases.

At subsonic and transonic speed, the grid fins improves the canard roll-control effectiveness at low α , but the improvement is clearly not as good as achieved at the low supersonic speed. The predicted C_l for both tail fin types are compared in figure 16 at the four Mach numbers investigated in this report and references (9) and (10). The grid fins clearly have the largest impact on canard roll-control effectiveness at $M = 1.5$. The grid fins have the least impact at $M = 3.0$; but in this case, the roll control does not suffer from any adverse effects. The

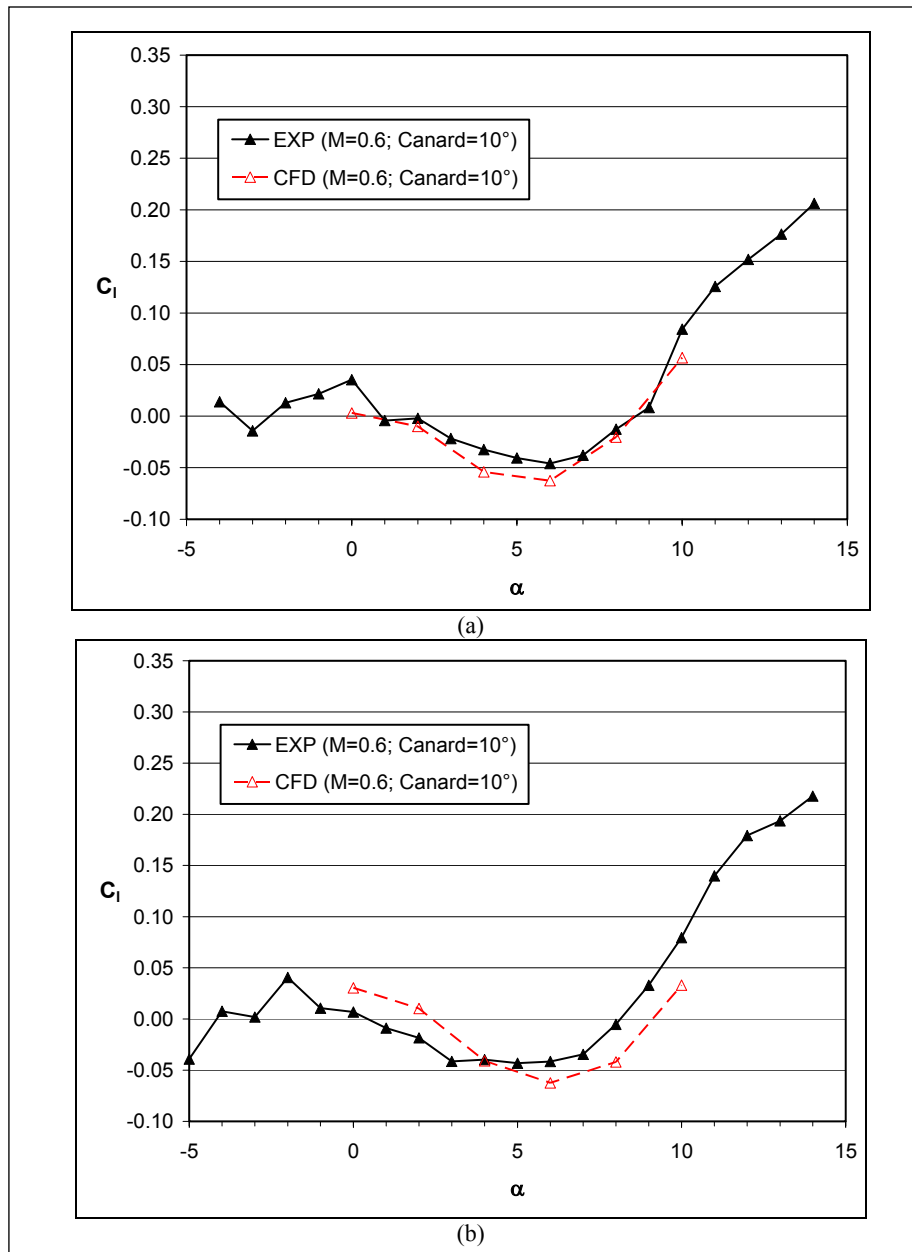


Figure 14. Computed and experimental rolling moment coefficient for (a) planar fin and (b) grid fin cases at Mach 0.6.

improvement in roll control at subsonic and transonic speed in the grid fin case at low α is evident for $0^\circ < \alpha < 2^\circ$. While there is some improvement in roll control for $\alpha < 2^\circ$ for the subsonic and transonic cases, there is no improvement for $\sim 2.5^\circ < \alpha < 7^\circ$. This behavior effectively nullifies the small benefit of using grid fins instead of planar fins at these speeds. In fact, the rolling moment in the subsonic and transonic cases with grid fins is reduced from that with planar fins for $8^\circ < \alpha < 10^\circ$.

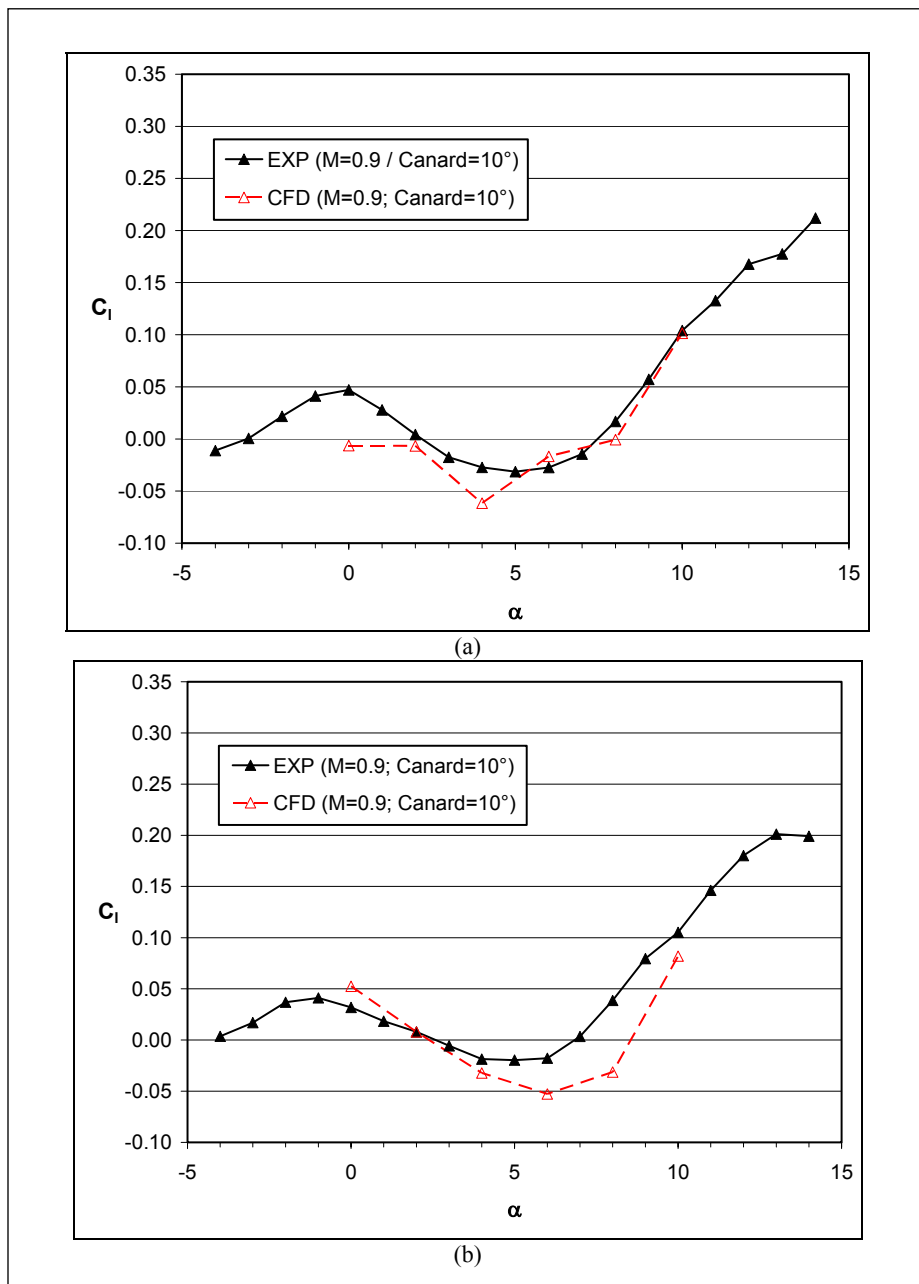


Figure 15. Computed and experimental rolling moment coefficient for (a) planar fin and (b) grid fin cases at Mach 0.9.

3.2 Flow-Field Visualizations

Visualizations of the flow field at subsonic and transonic speed show flow interaction effects that are similar to those observed in the supersonic cases. The downwash off the deflected canards produces a low-pressure region on the starboard side of the missile that in turn produces the induced side force. In addition, the canard trailing vortices interact with the fins until α is high enough so that the vortices miss the leeward fin. The adverse pressure on the leeward fin is primarily responsible for the adverse roll effects.

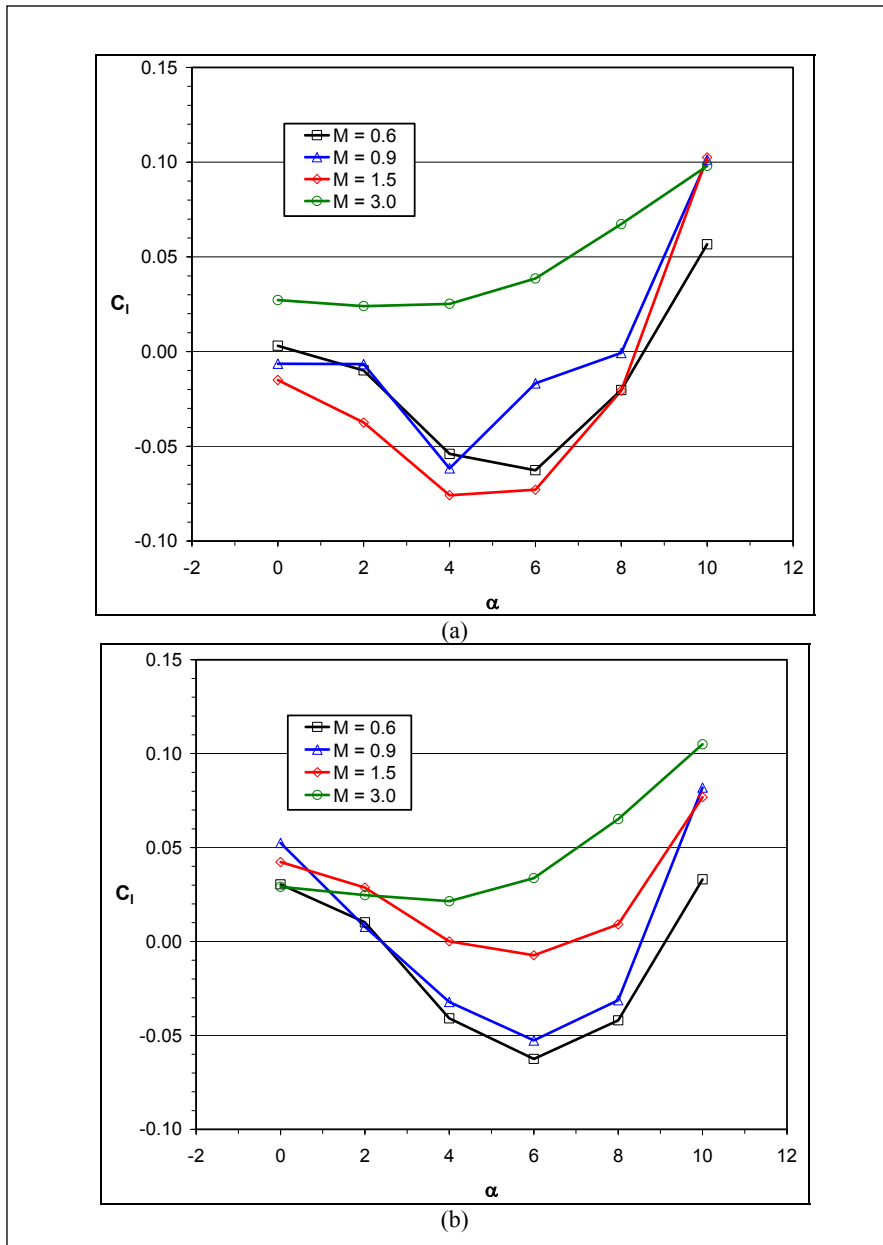


Figure 16. Computed rolling moment coefficient for (a) planar fin and (b) grid fin cases at several Mach numbers.

The result of the interaction of the canard trailing vortices with the tail fins is illustrated by contour plots of pressure coefficient on the missile surfaces in figures 17–20. In the planar fin case at $M = 0.6$, a small high-pressure region is observed on the starboard side of the leeward tail fin at $\alpha = 0^\circ$ (figure 17a). This causes a rolling moment opposite of that induced by the canards, thereby lowering the canard roll-control effectiveness. This high-pressure region is much larger at $\alpha = 4^\circ$ (figure 17b), where the adverse induced roll is nearly a maximum (figure 14a). At $\alpha = 10^\circ$ (figure 17c), high-pressure regions are on the port side of the leeward and windward fins. In this case, the adverse induced roll is minimized, and the canard effectiveness is

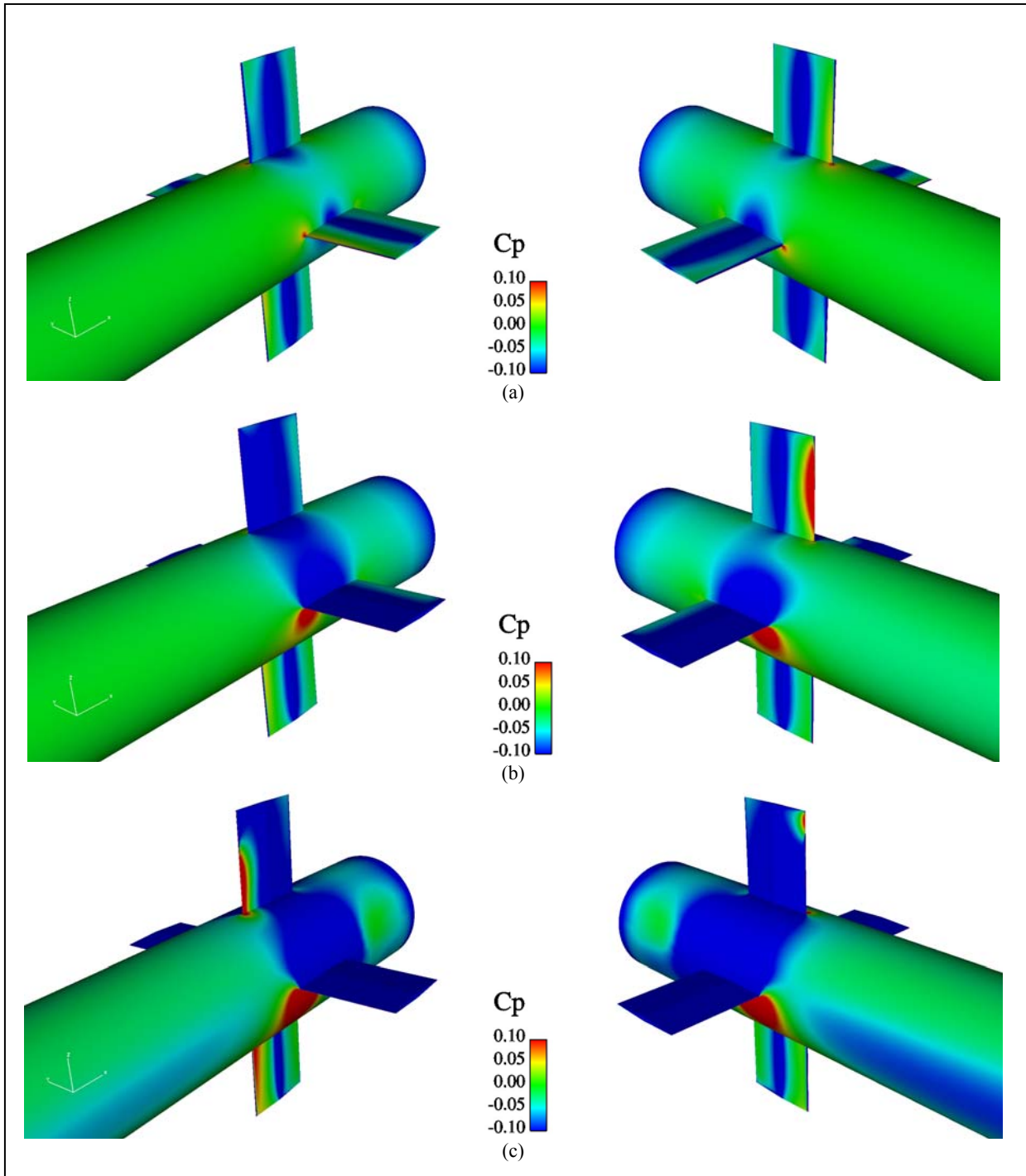


Figure 17. C_p contours on planar finned missile surfaces at $M = 0.6$ and (a) $\alpha = 0^\circ$, (b) $\alpha = 4^\circ$, and (c) $\alpha = 10^\circ$.

increased (figure 14a). Some minor differences can be observed in the planar fin case at $M = 0.9$ (figure 18), but the same induced roll effects are present.

In the grid fin case (figure 19), the effect is a little harder to observe. As in the supersonic case, the induced pressure on the grid fins is distributed over the fin more than in the planar fin case. Although a very high pressure is not observed on the grid fin vanes (as would be indicated by a

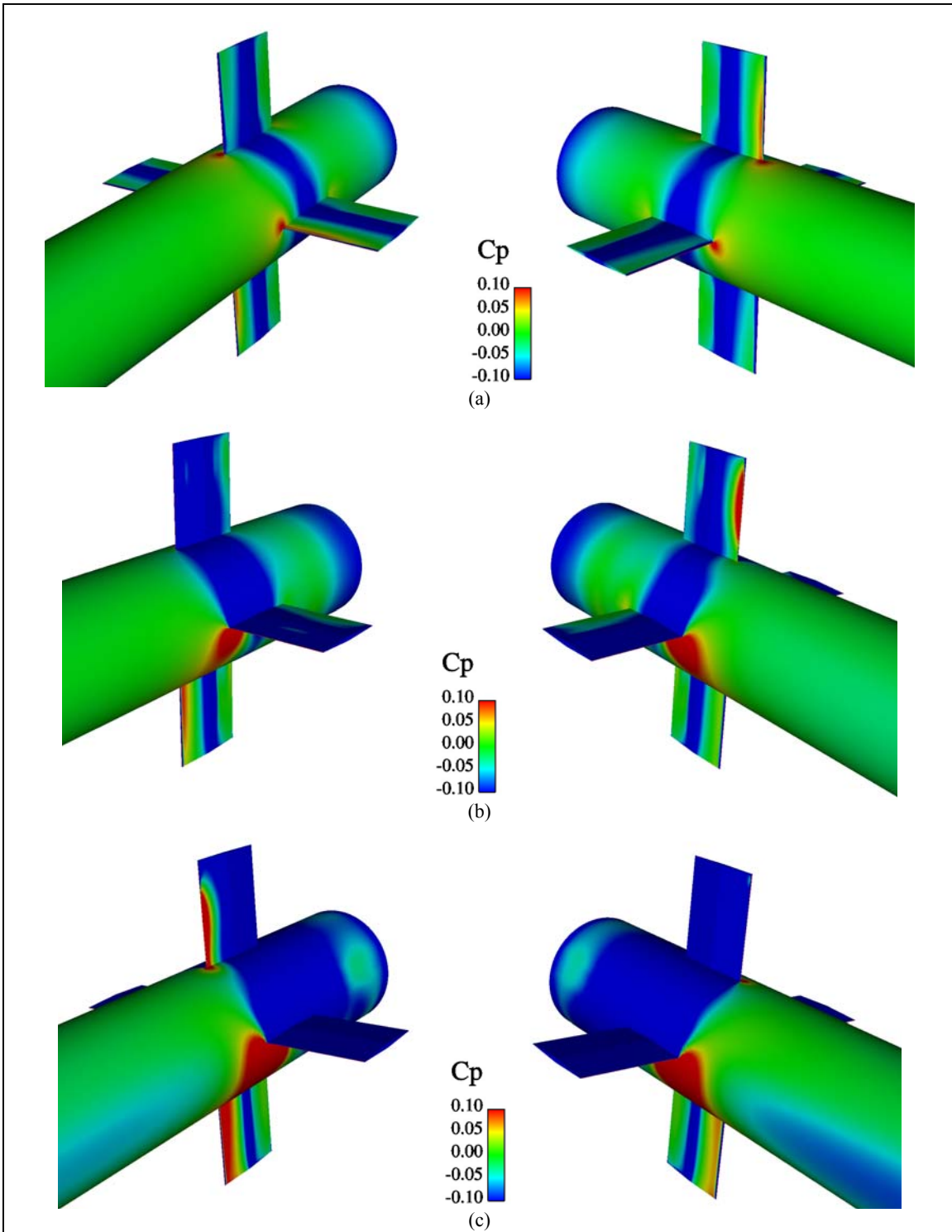


Figure 18. C_p contours on planar finned missile surfaces at $M = 0.9$ and (a) $\alpha = 0^\circ$, (b) $\alpha = 4^\circ$, and (c) $\alpha = 10^\circ$.

red color), higher pressures are observed more on the starboard sides of the leeward grid fin vanes than on the port sides at $\alpha = 0$ and 4° (figure 19a, b). At $\alpha = 10^\circ$ (figure 19c), the higher

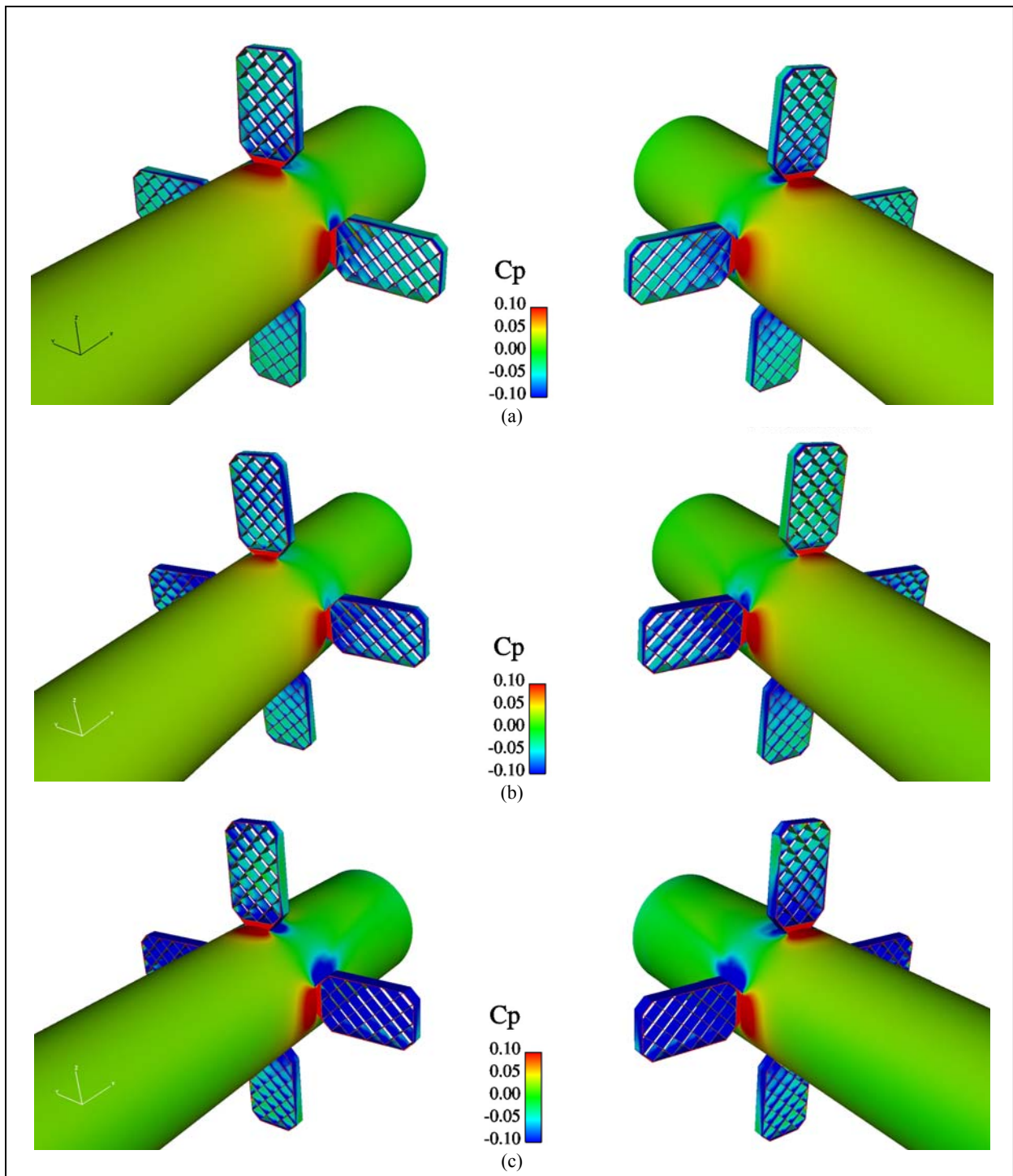


Figure 19. C_p contours on grid finned missile surfaces at $M = 0.6$ and (a) $\alpha = 0^\circ$, (b) $\alpha = 4^\circ$, and (c) $\alpha = 10^\circ$.

pressure has reversed sides, and canard roll-control effectiveness is improved. Again, there are minor differences at $M = 0.9$ (figure 20), but the general effect is the same.

The induced side force is generated on the missile body. This was confirmed in the supersonic cases by observing the separate components of side force on each surface (10). The effect is shown qualitatively for the $M = 0.6$ case in figure 21, where a larger low-pressure region is

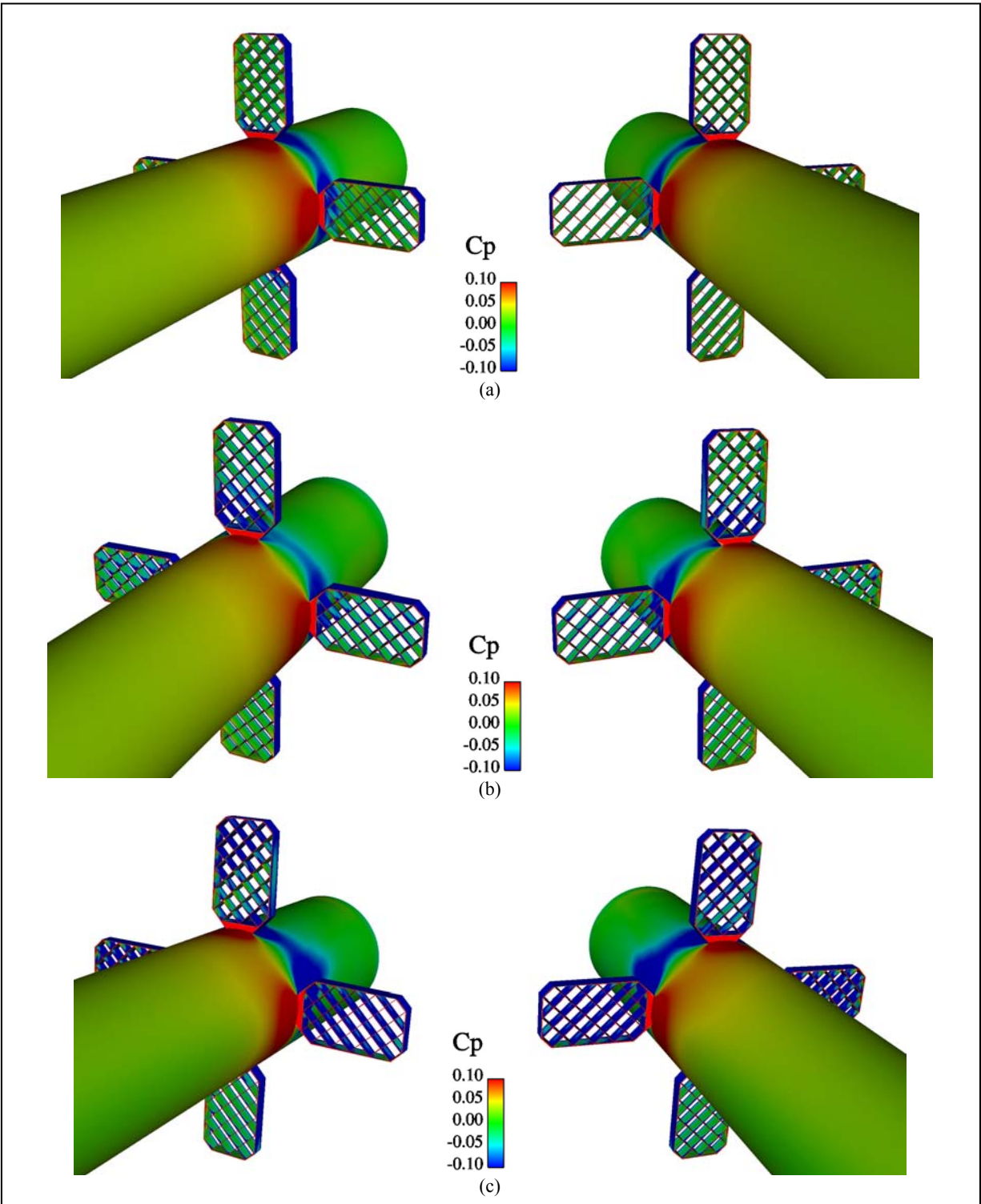


Figure 20. C_p contours on grid finned missile surfaces at $M = 0.9$ and (a) $\alpha = 0^\circ$, (b) $\alpha = 4^\circ$, and (c) $\alpha = 10^\circ$.

observed on the starboard side of the missile at $\alpha = 10^\circ$ (figure 21b). This generates the positive side force shown in figure 12. Understanding and quantifying this effect is important for

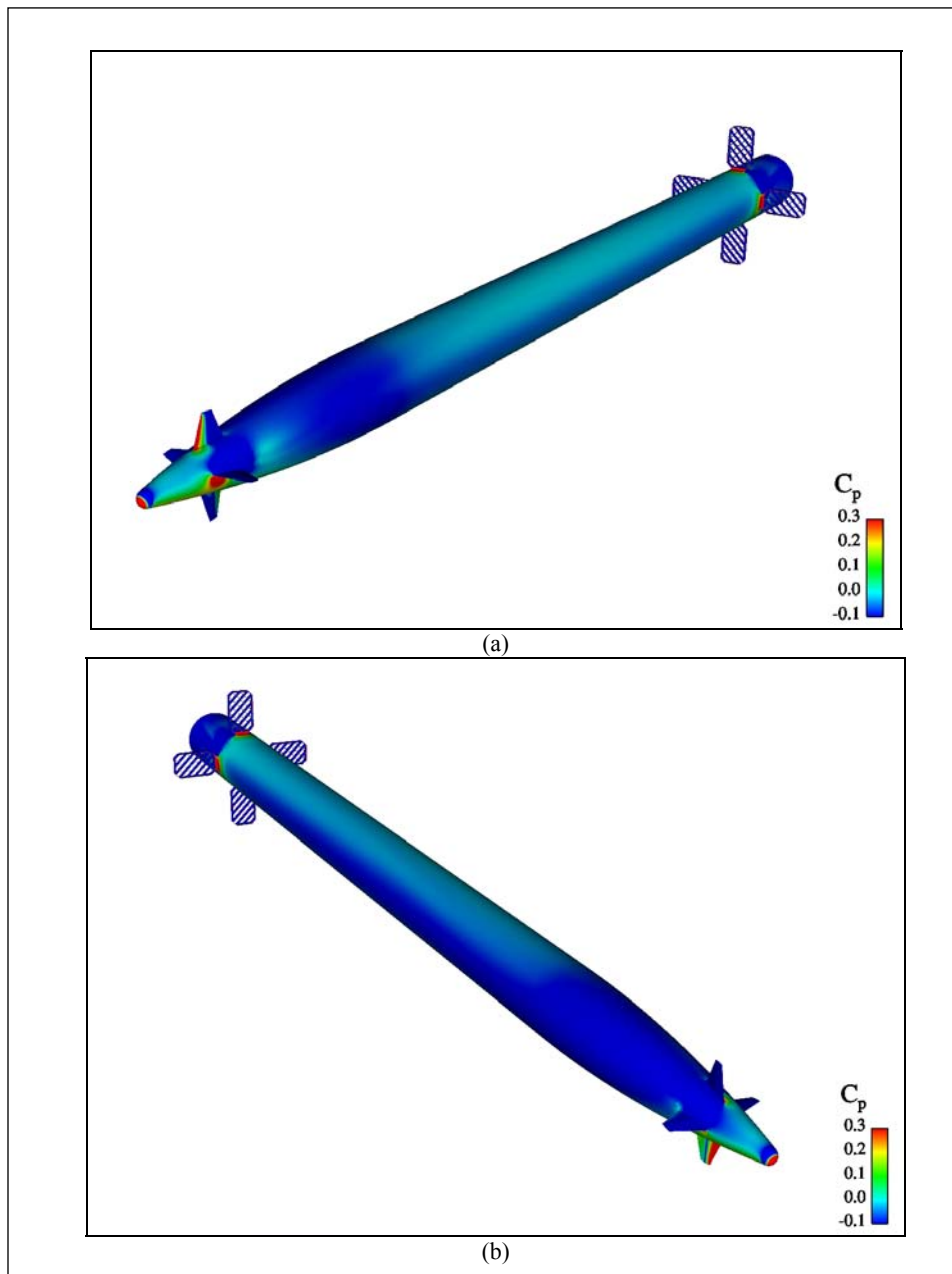


Figure 21. C_p contours on (a) port side and (b) starboard side of grid finned missile surfaces at $M = 0.6$ and $\alpha = 10^\circ$.

accounting for it with the proper flight control design. The effect was very similar for the $M = 0.9$ case, so it is not presented.

The canard trailing vortices at $\alpha = 4$ and 10° for the $M = 0.6$ cases are shown in figure 22 and figure 23, respectively. The effect is similar to that observed in the supersonic cases (10). The trailing vortex off the windward canard merges with the missile body boundary layer. The trailing vortices off the remaining three canards move toward the leeward side of the missile and will merge at different locations, depending on α . At $\alpha = 4^\circ$, the vortices interact with the tail fins before merging. In the planar fin case (figure 22a), the vortices pass by the leeward fin

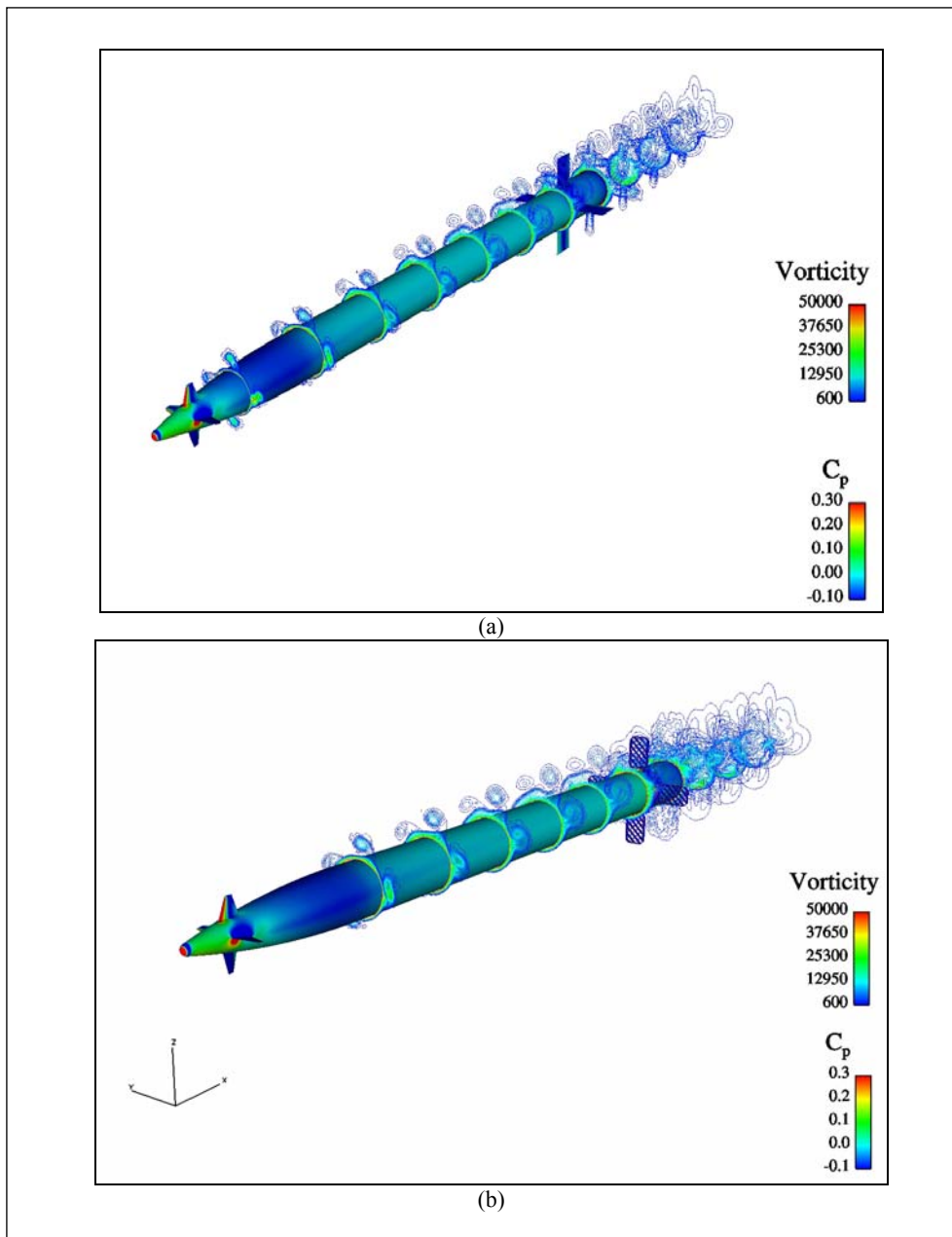


Figure 22. C_p surface contours and vorticity magnitude contours on cross planes at $x/d = 2, 4, \dots, 22$ for the (a) planar finned and (b) grid finned missile at $M = 0.6$ and $\alpha = 4^\circ$.

apparently unperturbed. In the grid fin case (figure 22b), however, the vortices that pass through the leeward tail fin are broken up. At $\alpha = 10^\circ$, the vortices merge before reaching the tail fins and do not interact with the fins at all. The body cross-flow vortices are primarily responsible for the interaction with the tail fins at this α . The flow pattern of the canard trailing vortices was very similar at $M = 0.9$, but intensity of the vortices was stronger.

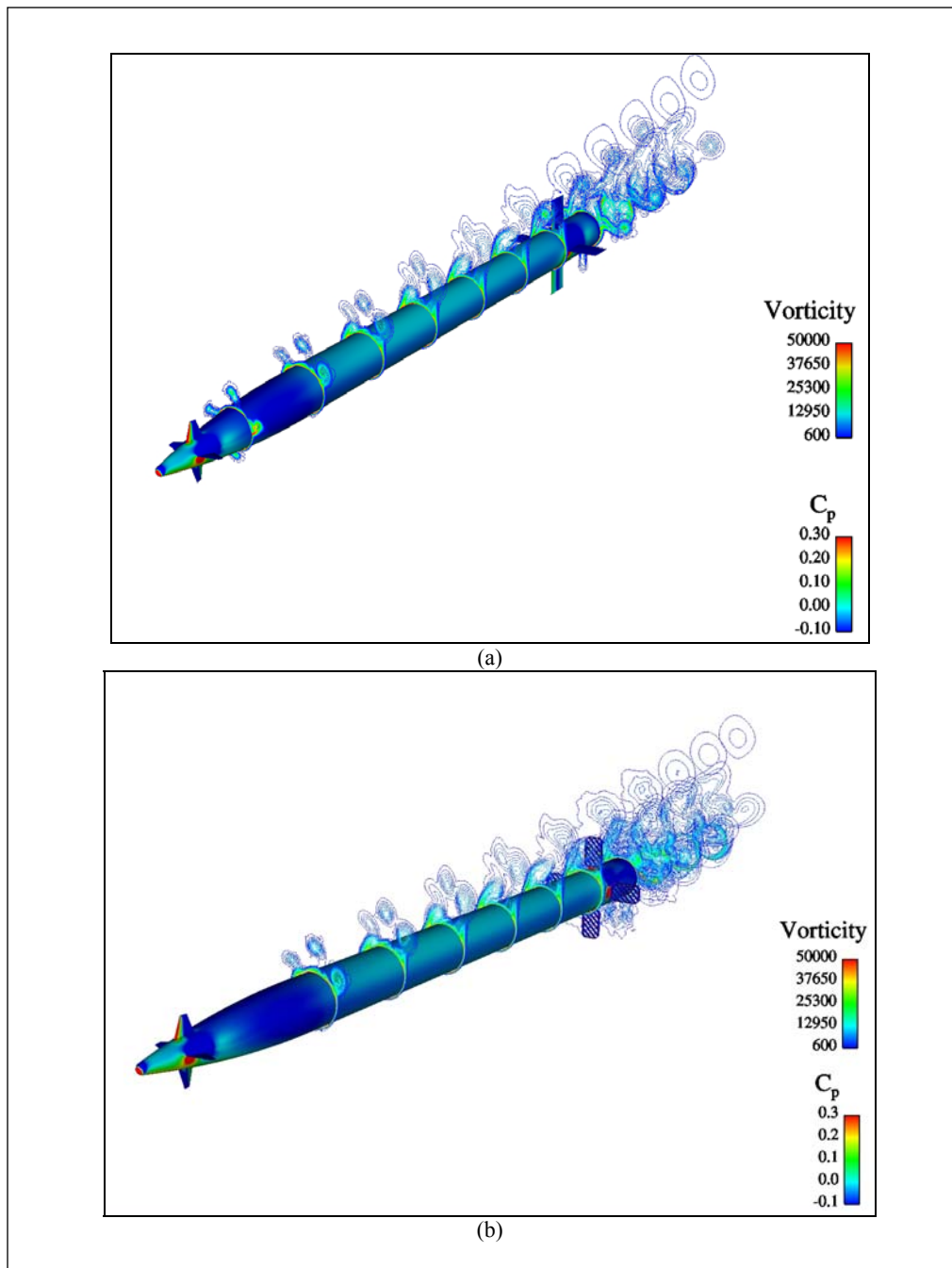


Figure 23. C_p surface contours and vorticity magnitude contours on cross planes at $x/d = 2, 4, \dots, 22$ for the (a) planar finned and (b) grid finned missile at $M = 0.6$ and $\alpha = 10^\circ$.

3.3 Control Surface Forces

The forces on the canards and fins are summarized in tabular and graphical form in appendices C–F. Some results are presented in this section to quantify the trends observed in the flow visualizations. The forces on the leeward and windward fins resulting in the adverse rolling moment are shown in figure 24, which shows the side force coefficient on each fin for the planar

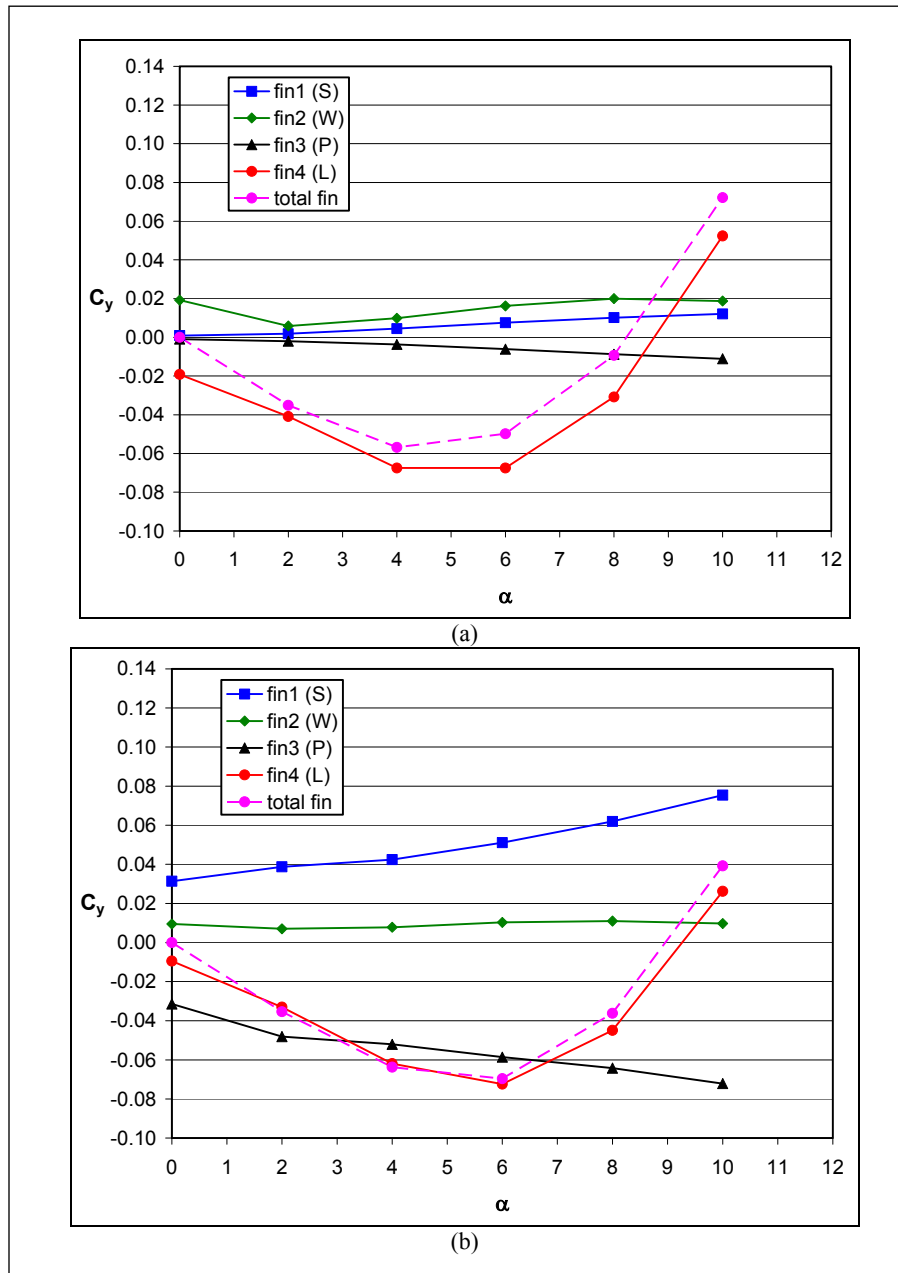


Figure 24. Side force coefficient on tail fins for (a) planar fin and (b) grid fin case for $\delta = 10^\circ$ and $M = 0.6$.

and grid fin cases at $\delta = 10^\circ$ and $M = 0.6$. In the planar fin case, the windward fin (fin 2) is at a nearly constant, small positive value. The leeward fin (fin 4) is negative until $\alpha > 8^\circ$. As in the supersonic case, this force imbalance produces the adverse rolling moment. The side forces on the fins are of the same order as those on the canards; however, the larger moment arm of the fins produces a larger rolling moment. In the grid fin case (figure 24b), there is a small reduction in the side forces at $\alpha = 0^\circ$ but not much at higher α . As in the supersonic case, the normal forces on the starboard and port fins also contribute to the adverse rolling moment. This is illustrated in figure 25, which shows the normal force coefficient on each fin for the planar and

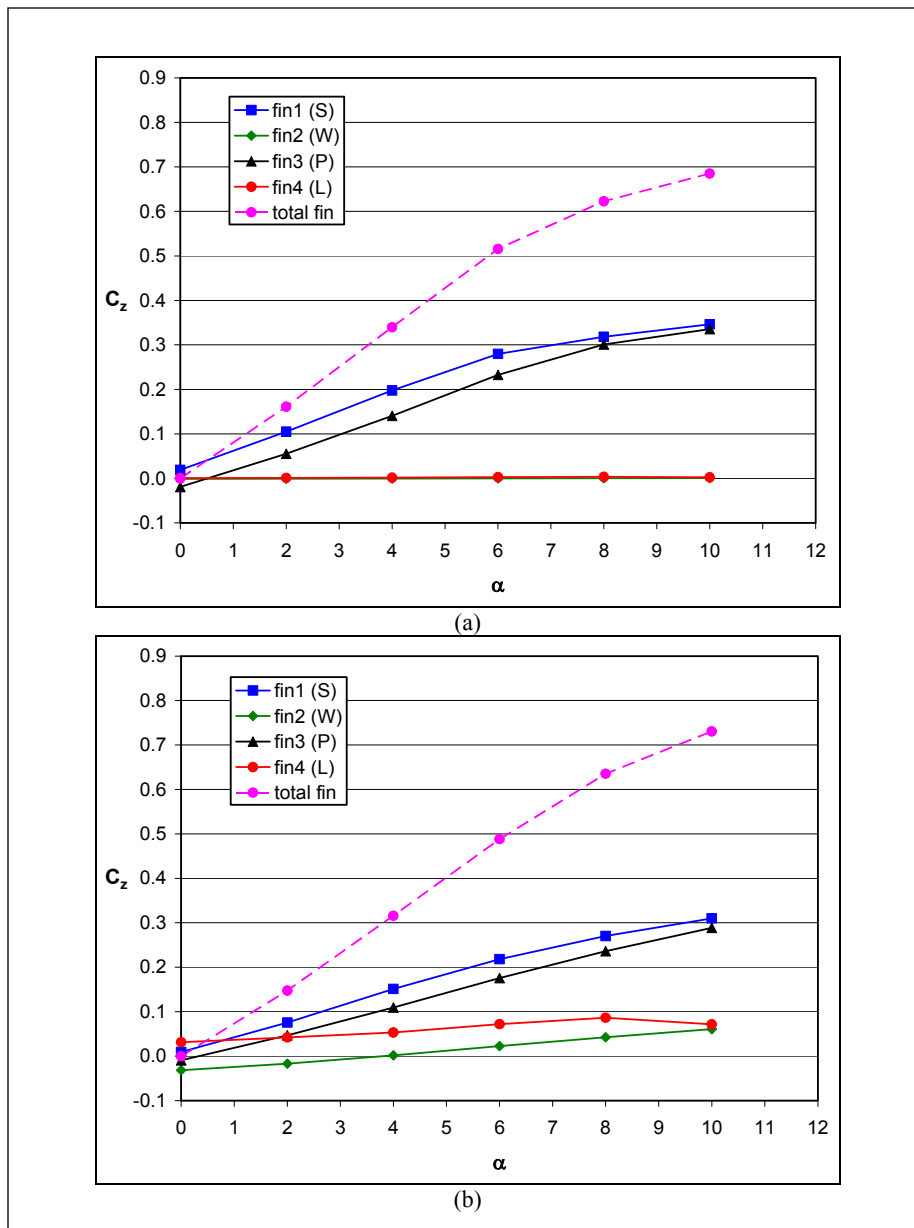


Figure 25. Normal force coefficient on tail fins for (a) planar fin and (b) grid fin case for $\delta = 10^\circ$ and $M = 0.6$.

grid fin cases at $\delta = 10^\circ$ and $M = 0.6$. The normal force behavior at $M = 0.9$ was similar to that at $M = 0.6$. The reduction of the difference in normal force between the starboard and port fins is only slightly smaller when the grid fins are used. However, even for the planar fin case, the component of the adverse rolling moment due to the difference in normal force on the horizontal fins at the subsonic and transonic speeds is smaller than it was at $M = 1.5$ (10).

3.4 Flow-Through Grid Fins

Another important aspect to the performance of grid fins is the state of the flow as it passes through the grid fin cells. An earlier study on grid fins (6) showed that a “bucket” exists in the

normal force vs. Mach number curve through the transonic and lower supersonic range. This is illustrated in figure 26, which was excerpted from figure 6 of reference (6). The figure presents the zero angle of attack fin normal force slope ($C_{NF\alpha}$) as a function of Mach number for a fin configuration, similar to the one used in this study. The data follow trends similar to those exhibited by conventional fins at subsonic ($M < 0.75$) and higher supersonic ($M > 1.60$) Mach numbers.

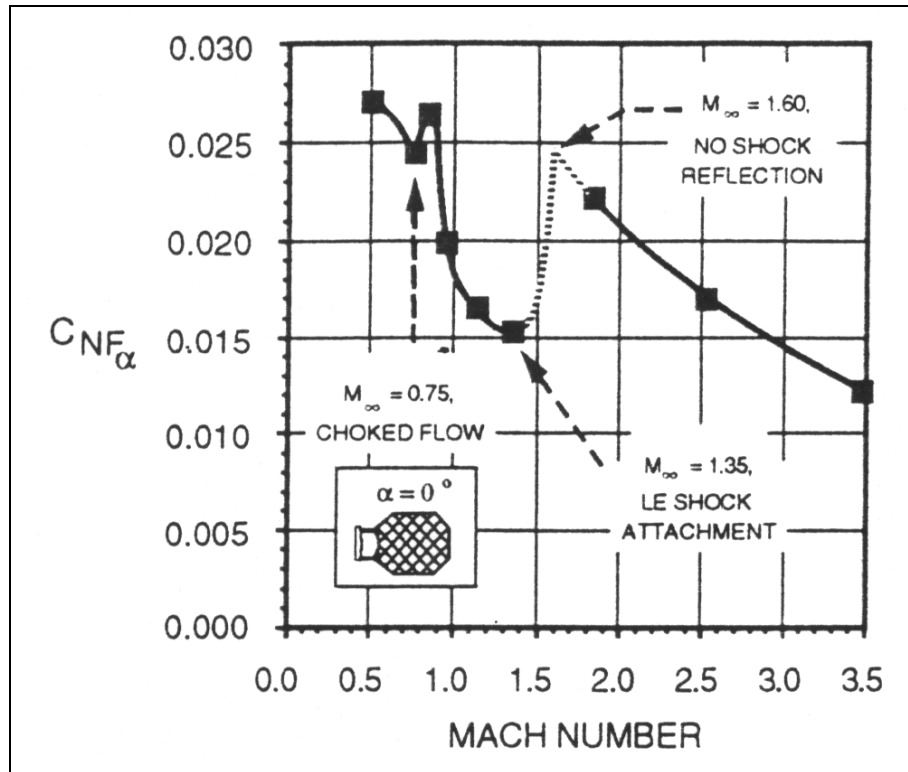


Figure 26. Fin normal force slope values as a function of Mach number (6).

Washington and Miller (6) attributed this “bucket” to two separate flow phenomena and stated it was a function of the grid fin internal cell geometry. For analysis purposes, they viewed a grid fin as a collection of individual cells acting as separate inlets. Washington and Miller proposed a grid fin flow field, indicating choking in the grid fin cells. This is illustrated in figure 27, which is excerpted from figure 7 of reference (6). At freestream Mach numbers < 1.0 , the reduction in the inlet cross-sectional area caused by the presence of the cell structural members and the build-up of the boundary layer on the cell walls causes the flow through the cell to accelerate to sonic (choked) conditions (figure 27a). The cell remains choked as the freestream Mach number increases past Mach 1.0 until a normal shock forms ahead of the grid fin cell itself (figure 27b). The reduction in flow through the grid fin cells causes a reduction in the normal force generated by the fin.

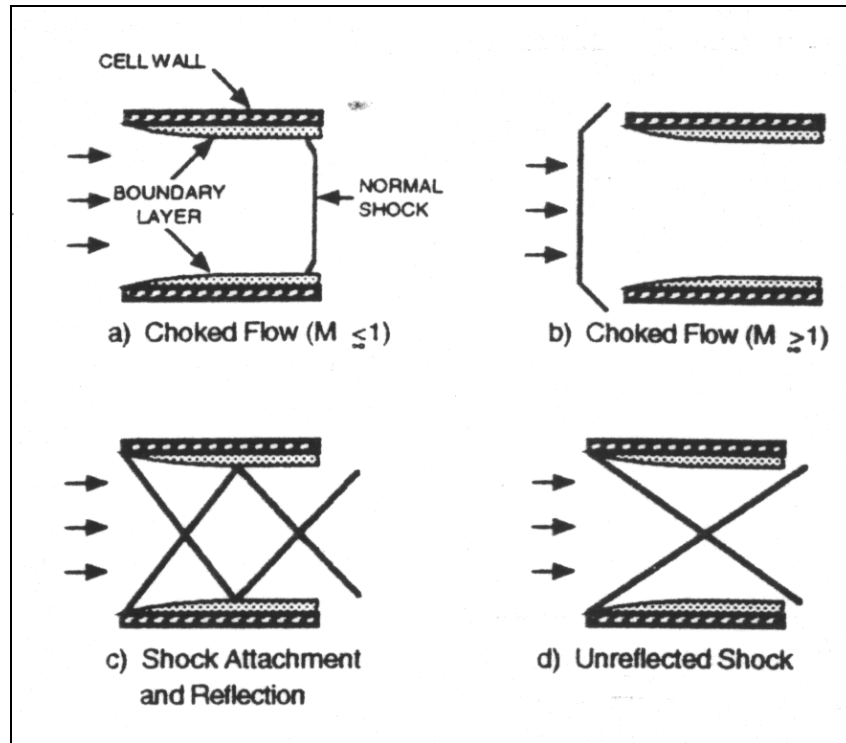


Figure 27. Grid fin flow field proposed in reference (6).

Increases of the freestream Mach number well beyond 1.0 eventually enable the cell to “swallow” the shock, resulting in a shock wave attaching to the leading edge of the cell. At lower supersonic Mach numbers, the leading edge shock wave may reflect within the cell structure, as shown in figure 27c. Increasing the freestream Mach number further will eventually lead to the shock wave passing through the cell without reflecting off the grid fin cell structure (figure 27d). Increases in the freestream Mach number further should have no qualitative effect on the grid fin flow field. Washington and Miller (6) state that the point where the shock wave first passes through the grid fin cell structure undisturbed is where the grid fin begins to exhibit supersonic normal force characteristics similar to conventional fins. In figure 26, the onset of choked flow is indicated at $M = 0.75$, leading edge shock attachment is indicated at $M = 1.35$, and the point of no-shock reflection is indicated at $M = 1.60$.

The flow-field solutions obtained via CFD computations allow us to qualitatively compare the flow field through the grid fin cell structure with that proposed by Washington and Miller (6). Figures 28–31 present the flow field on the symmetry plane of the grid fin missile for cases at $\delta = 10^\circ$, $\alpha = 0^\circ$, and $M = 0.6, 0.9, 1.5$, and 3.0 . Contours of C_p are shown in the first two parts of each figure, while contours of the Mach number are shown in the third part. The leeward grid fin geometry is not shown in the figures so that the flow field inside the grid fin cell structure can be observed. Part “a” of each figure shows the flow field over the whole missile. Strong vortices are observed trailing the canards at $M = 0.6, 0.9$, and 1.5 . The vortices were weaker at $M = 3.0$ and could not be observed with the contour scale used in figure 31. Typical oblique shock wave

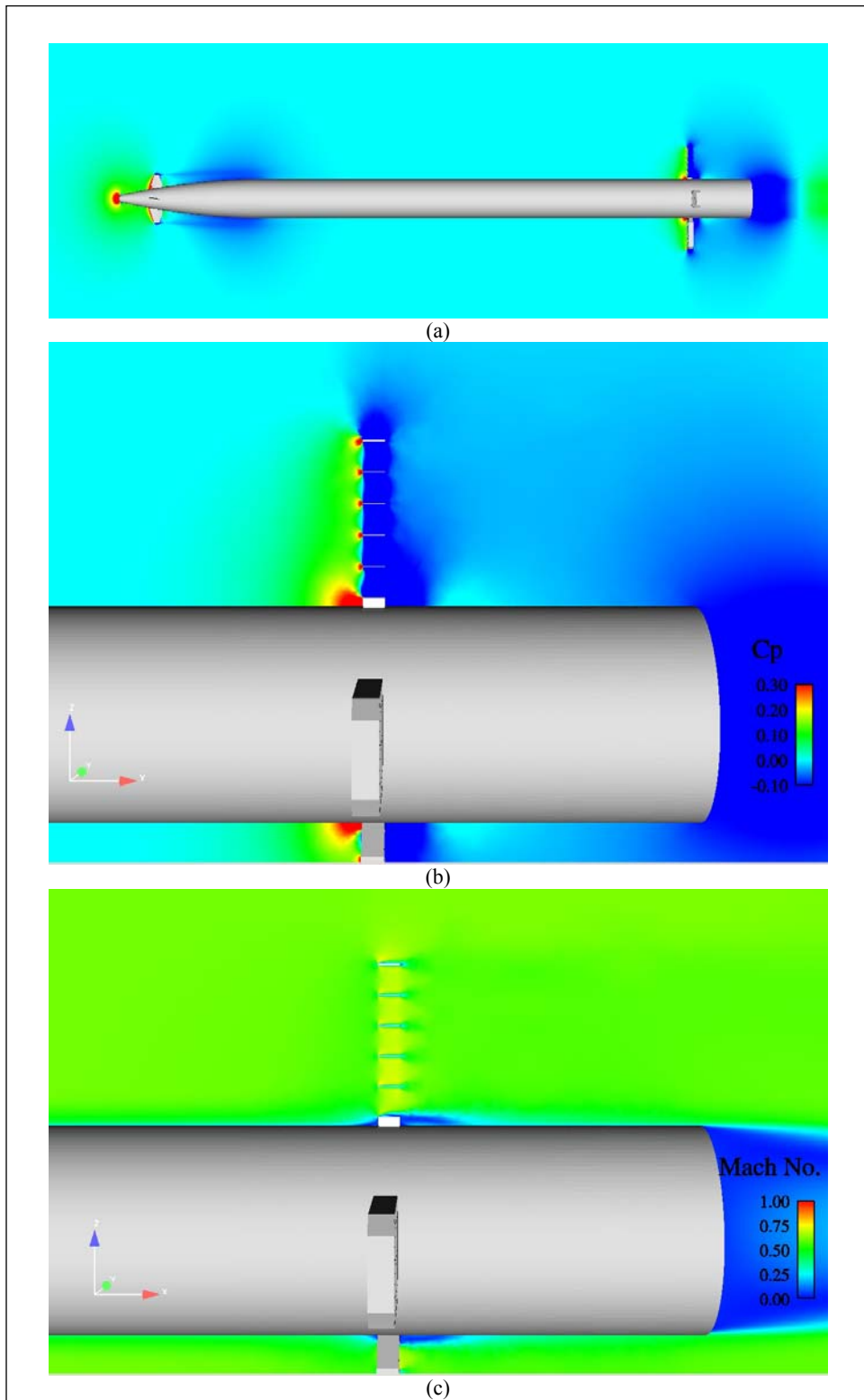


Figure 28. C_p (a, b) and Mach number (c) contours on vertical symmetry plane with leeward grid fin geometry removed, $\alpha = 0^\circ$ and $M = 0.6$.

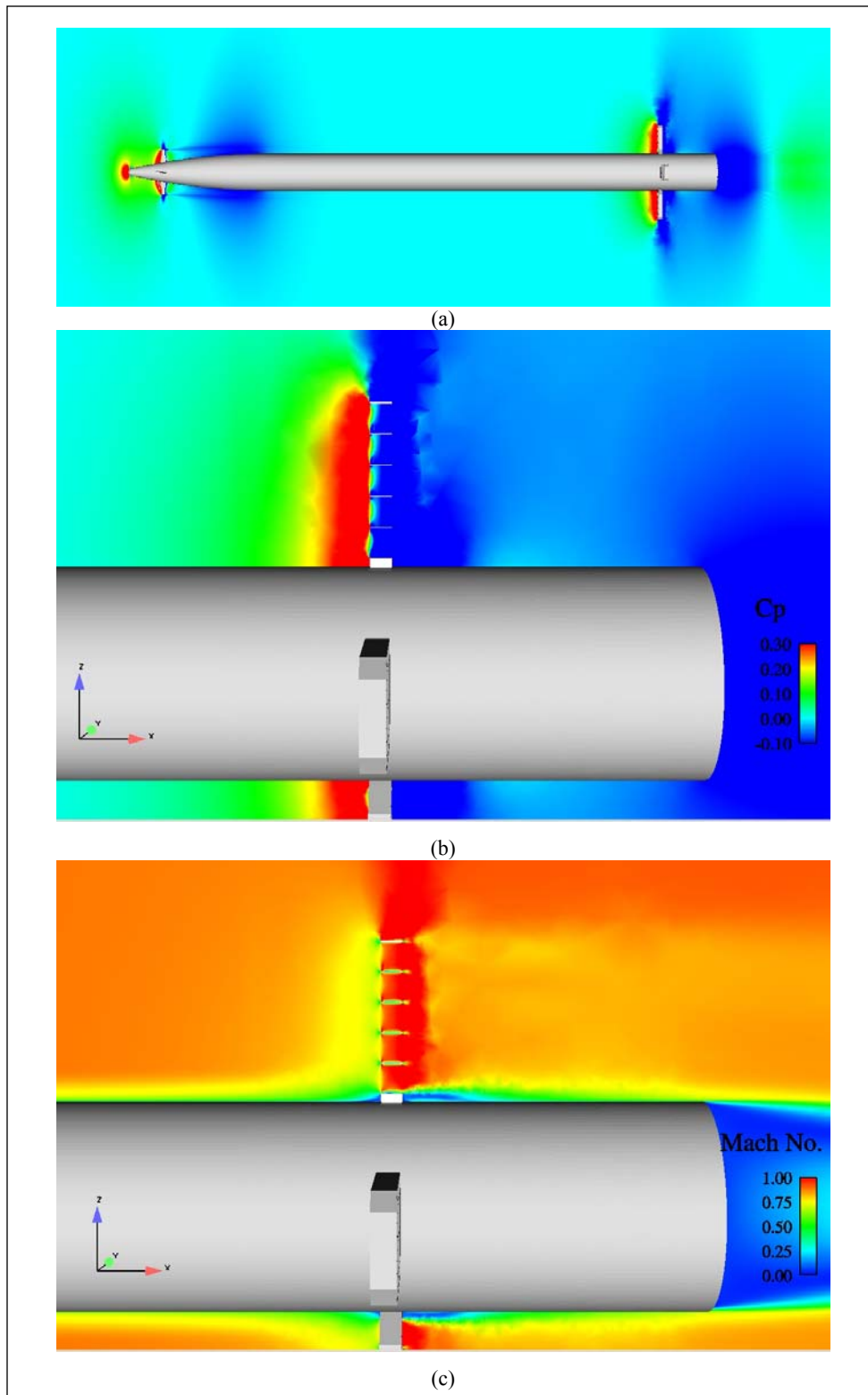


Figure 29. C_p (a, b) and Mach number (c) contours on vertical symmetry plane with leeward grid fin geometry removed, $\alpha = 0^\circ$ and $M = 0.9$.

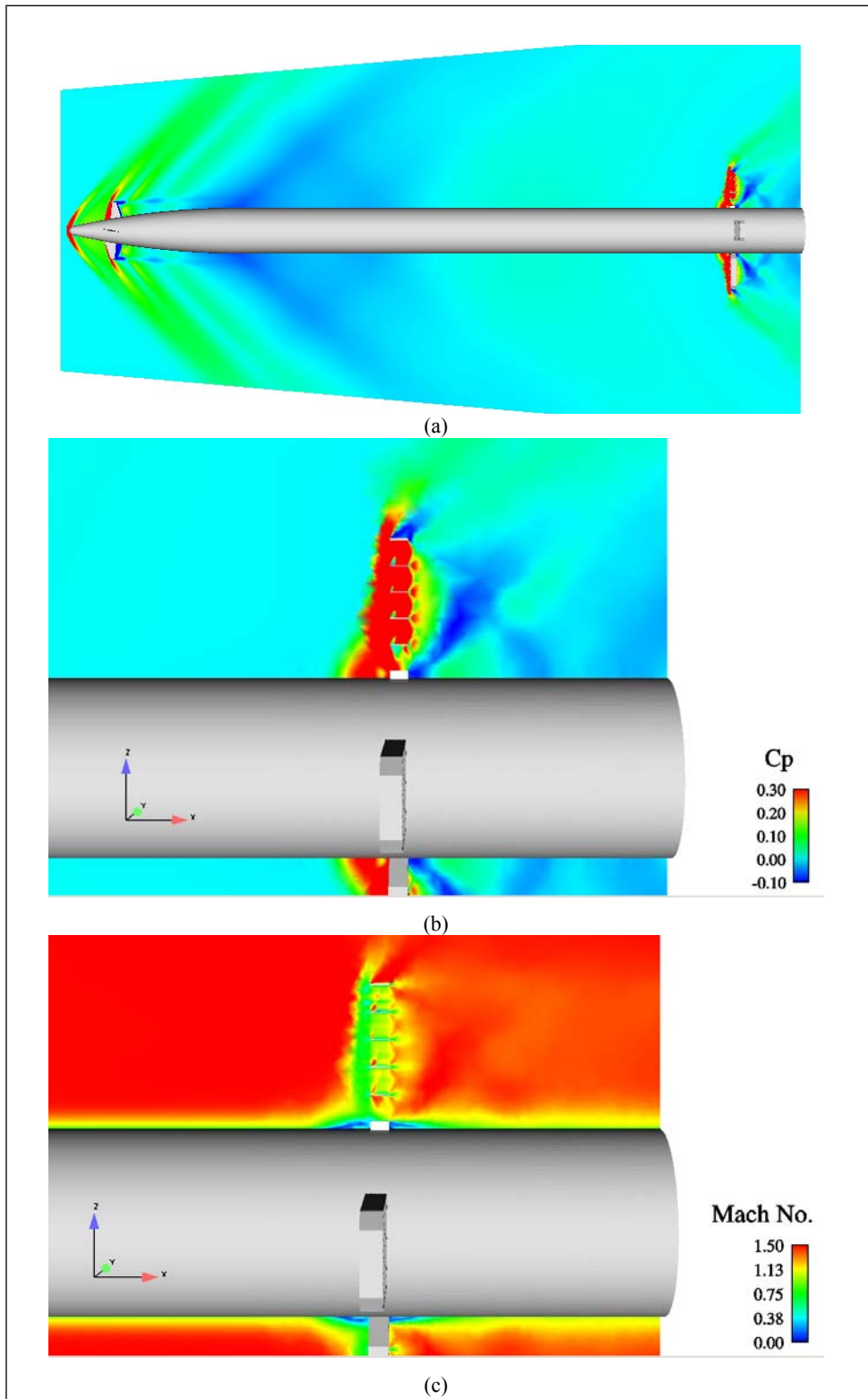


Figure 30. C_p (a, b) and Mach number (c) contours on vertical symmetry plane with leeward grid fin geometry removed, $\alpha = 0^\circ$ and $M = 1.5$.

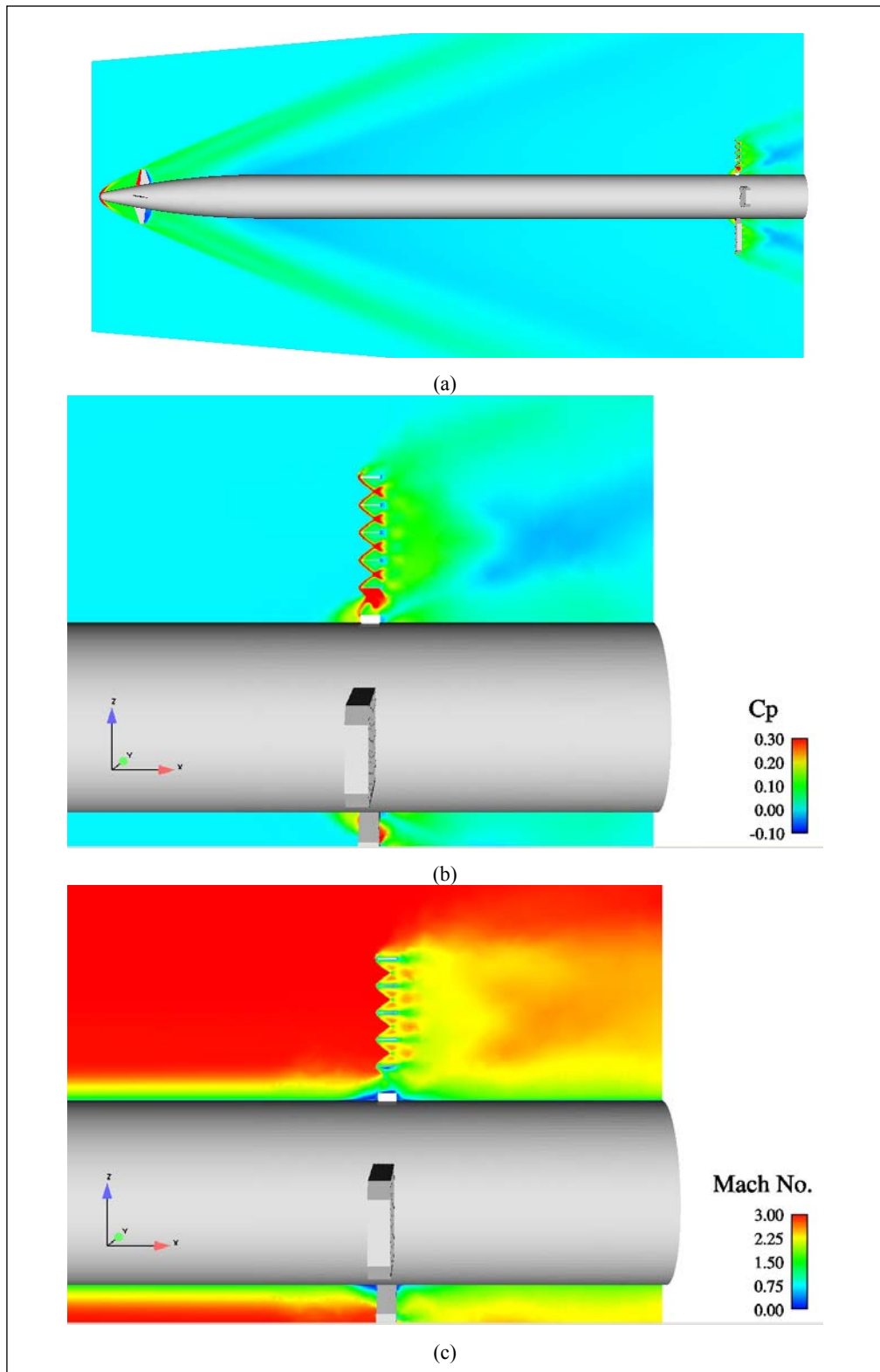


Figure 31. C_p (a, b) and Mach number (c) contours on vertical symmetry plane with leeward grid fin geometry removed, $\alpha = 0^\circ$ and $M = 3.0$.

structures are observed at the supersonic Mach numbers. For the $M = 0.9$ case, probing of the flow field showed that weak shock waves form near the nose and at the tips of the canards and fins.

Parts “b” and “c” of each figure show the C_p and Mach number contours, respectively, in the region of the leeward grid fin. It must be noted that these cases are with the canards deflected ($\delta = 10^\circ$), so vortices from the leeward, port, and starboard canards will be impacting the flow field near the leeward grid fin. However, general conclusions on the flow-field structure can still be surmised. At $M = 0.6$ (figure 28), the flow accelerates only to $\sim 0.70 < M < 0.75$, so no flow choking is observed. At $M = 0.9$ (figure 29), a shock forms inside the grid fin cell, ~ 0.75 chord lengths from the leading edge of the fin. This shock cannot be seen with the contour scales shown in the figure; it was determined by interactively probing the data in the post-processing software. This choked flow case compares to case “a” of figure 27.

At $M = 1.5$ (figure 30), a normal shock forms within 1 chord length ahead of the grid fin cells. Normal shock relations give $M_2 = 0.7$ for $M_1 = 1.5$, and interactive probing of the flow field gave Mach number values of $0.7\text{--}0.75$ in the region behind this shock wave (M_2). Some of the jaggedness in the contours is believed to be at least in part due to the contouring programs. Some may also be due to effects of the canard-trailing vortices impacting the flow field in this region. The mesh in this region is made up of fine tetrahedral cells (figure 4) and is adequate for capturing the shock waves. The flow then accelerates through the grid fin cells and chokes within the cells. The flow is rather complex, with oblique shocks forming on the web between the bottom two cells. It is likely that the impact of the canard-trailing vortices is affecting the flow-field structure. The flow is definitely choked, with a combination of cases “a–c” of figure 27. At $M = 3.0$ (figure 31), there are oblique shocks at the leading edges of the grid fin cells. These shocks reflect off each other, but do not reflect off the cell walls. This flow structure corresponds to case “d” of figure 27.

It is difficult to correlate the grid fin choking with the effectiveness of the grid fins at reducing the roll-reversal effect. The greatest reduction of roll-reversal was at $M = 1.5$, while there was only a small effect at low α for $M = 0.9$, and there was fin choking at both these Mach numbers. The roll reversal effect at $M = 0.6$ (no choking) was similar to that at $M = 0.9$.

4. Summary and Conclusions

Viscous CFD calculations were used to predict the aerodynamic coefficients and flow field around a generic canard-controlled missile configuration in subsonic ($M = 0.6$) and transonic ($M = 0.9$) flow. Validation of the computed results was demonstrated by the very good agreement between the computed aerodynamic coefficients and those obtained from wind tunnel measurements.

Visualizations of the flow field showed that the canard downwash produced a low-pressure region on the starboard side of the missile that, in turn, produced a large induced side force. This was very similar to the effect observed at low supersonic speed ($M = 1.5$) (10). Visualizations also showed that the canard-trailing vortices interact with the tail fins in the same way as at supersonic speed. This interaction takes place until α is high enough so that the vortices miss the leeward fin. The pressure differential on the leeward tail fin, produced by this interaction, is primarily responsible for the adverse induced roll effects.

Visualizations of the flow field through the grid fin structure showed choking of the flow at $M = 0.9$ and $M = 1.5$. The grid fin choking phenomena could not be correlated with the effectiveness of the grid fin to alleviate the roll-reversal problem.

The validated CFD results show that grid fins do not improve the canard roll-control effectiveness at subsonic and transonic speeds as well as they do at the low supersonic speed. While there is some improvement for $\alpha < 2^\circ$, it is negated by reversed roll above $\alpha = 2^\circ$. This behavior makes it difficult for the control system to maintain a stabilized roll attitude, thereby making it impractical to employ grid fin tail surfaces on canard-controlled missiles at subsonic and transonic speeds.

5. References

1. Allen, J. M.; Blair, A. B., Jr. Comparison of Analytical and Experimental Supersonic Aerodynamic Characteristics of a Forward Control Missile. *Journal of Spacecraft and Rockets* **1982**, *19* (2), 155–159.
2. Blair, A. B., Jr.; Dillon, J. L., Jr.; Watson, C. B. Experimental Study of Tail-Span Effects on a Canard-Controlled Missile. *Journal of Spacecraft and Rockets* **1993**, *30* (5), 635–640.
3. Blair, A. B., Jr. Supersonic Aerodynamic Characteristics of a Maneuvering Canard-Controlled Missile With Fixed and Free-Rolling Tail Fins. SAE Paper 90–1993; Society of Automotive Engineers: Warrendale, PA, October 1990.
4. Burt, J. R., Jr. *The Effectiveness of Canards for Roll Control*; RD-77-8; U.S. Army Missile Command: Redstone Arsenal, AL, 1976.
5. Miller, M. Aerodynamic Investigation of a Canard Controlled Missile Using Planar and Grid Fin Tail. Dynetics, Inc.: Huntsville, AL, unpublished work.
6. Washington, W. D.; Miller, M. S. Grid Fins—*A New Concept for Missile Stability and Control*; AIAA Paper 93–0035; American Institute of Aeronautics and Astronautics: Reston, VA, January 1993.
7. DeSpirito, J.; Edge, H. L.; Weinacht, P.; Sahu, J.; Dinavahi, S. P. G. Computational Fluid Dynamics Analysis of a Missile With Grid Fins. *Journal of Spacecraft and Rockets* **2001**, *38* (5), 711–718.
8. DeSpirito, J.; Sahu, J. *Viscous CFD Calculations of Grid Fin Missile Aerodynamics in the Supersonic Flow Regime*; AIAA Paper 2001–2057; American Institute of Aeronautics and Astronautics: Reston, VA, January 2001.
9. DeSpirito, J.; Vaughn, M. E., Jr.; Washington, W. D. *CFD Investigation of Canard-Controlled Missile With Planar and Grid Fins in Supersonic Flow*; AIAA Paper 2002-4509; American Institute of Aeronautics and Astronautics: Reston, VA, August 2002.
10. DeSpirito, J.; Vaughn, M. E., Jr.; Washington, W. D. *Numerical Investigation of Aerodynamics of Canard-Controlled Missile Using Planar and Grid Tail Fins, Part I: Supersonic Flow*; ARL-TR-2848; U. S. Army Research Laboratory: Aberdeen Proving Ground, MD, 2002.
11. Fluent, Inc. “Fluent 6.0 User’s Guide.” Vol. 2, Lebanon, NH, 2001.

12. Shih, T. H.; Liou, W. W.; Shabbir, A.; Yang, Z.; Zhu, J. A New k - ε Eddy-Viscosity Model for High Reynolds Number Turbulent Flows—Model Development and Validation. *Computers and Fluids* **1995**, *24* (3), 227-238.
13. Moore, F. G.; McInville, R. M.; Hymer, T. C. Application of the 1998 Version of the Aeroprediction Code. *Journal of Spacecraft and Rockets* **1999**, *36* (5), 633–645.

Appendix A. Aerodynamic Coefficients for Planar Fin Case

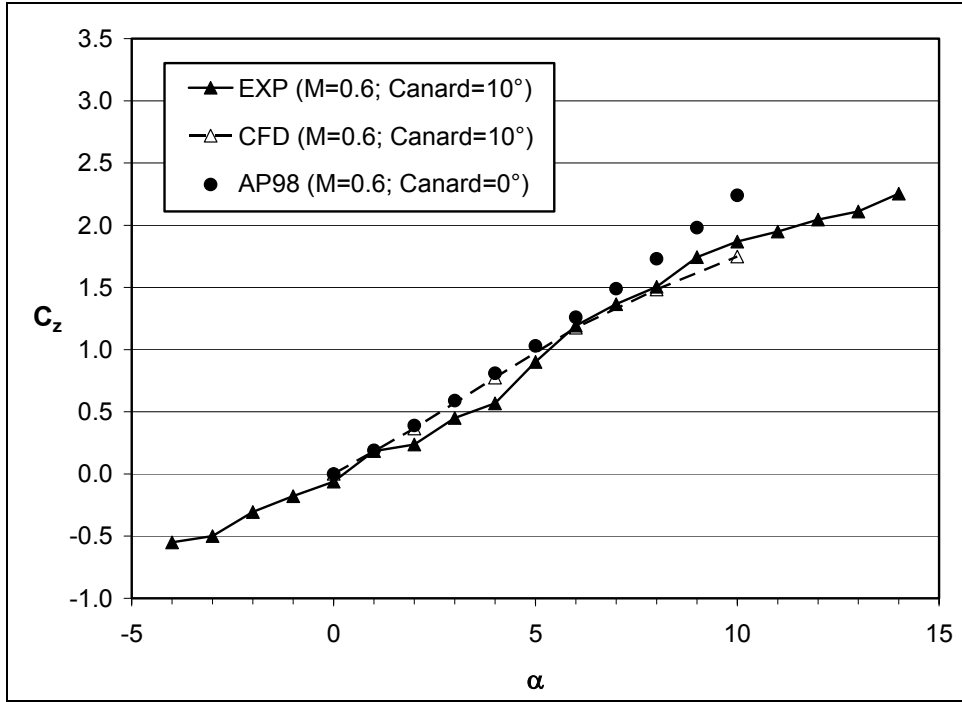


Figure A-1. Normal force for the planar fin case at Mach 0.6.

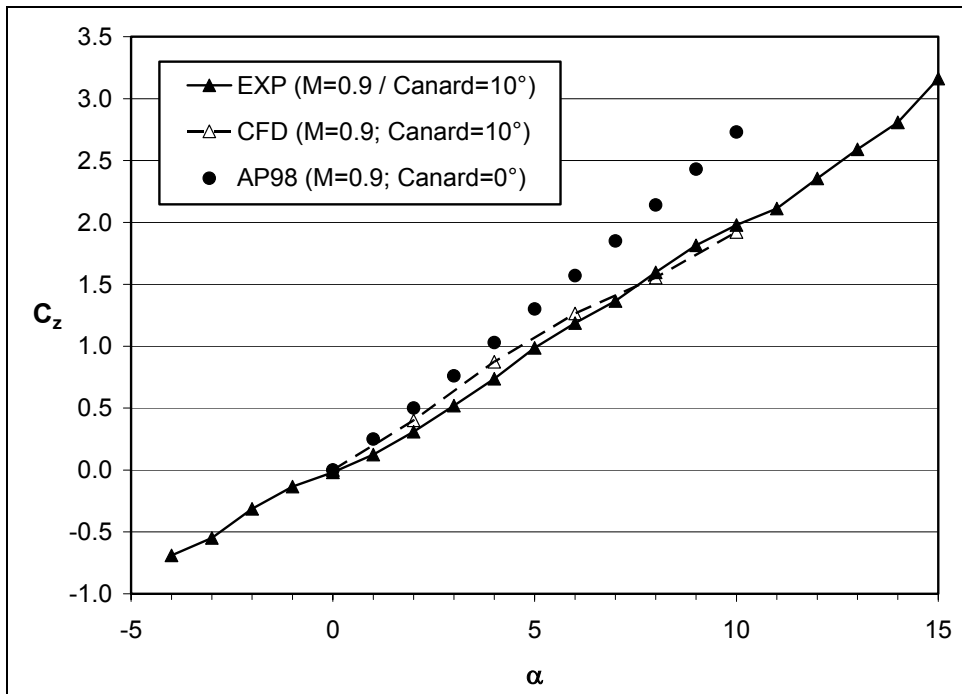


Figure A-2. Normal force for the planar fin case at Mach 0.9.

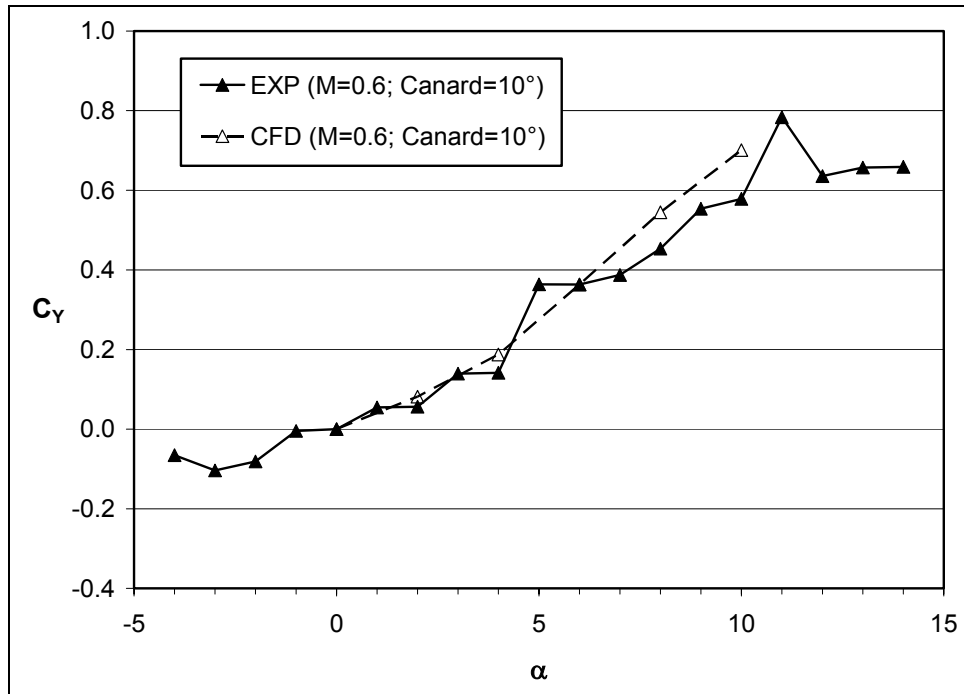


Figure A-3. Side force for the planar fin case at Mach 0.6.

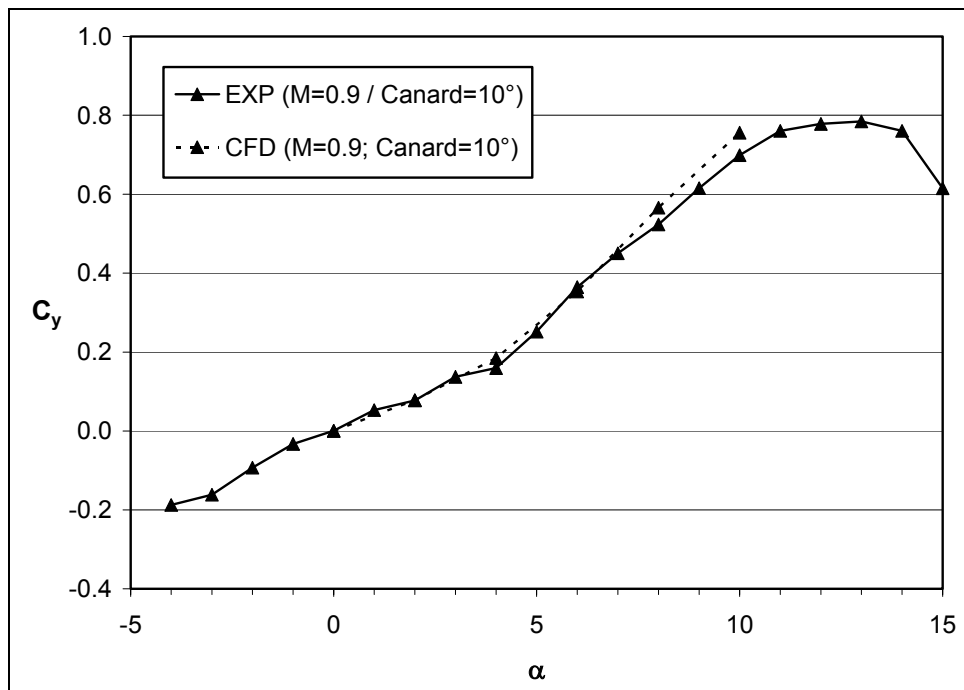


Figure A-4. Side force for the planar fin case at Mach 0.9.

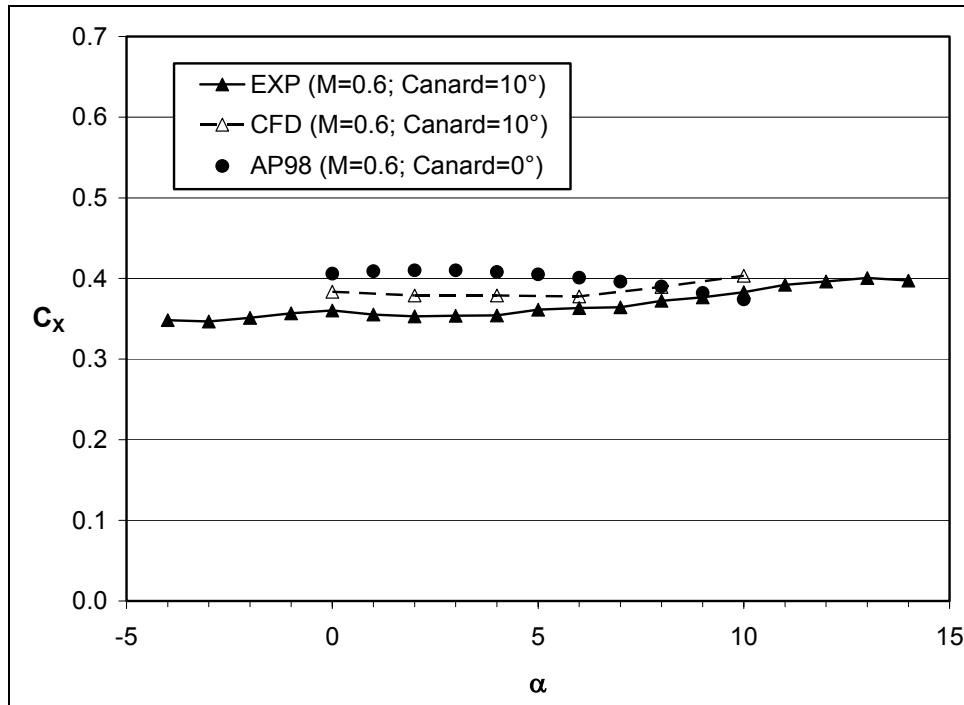


Figure A-5. Axial force for the planar fin case at Mach 0.6.

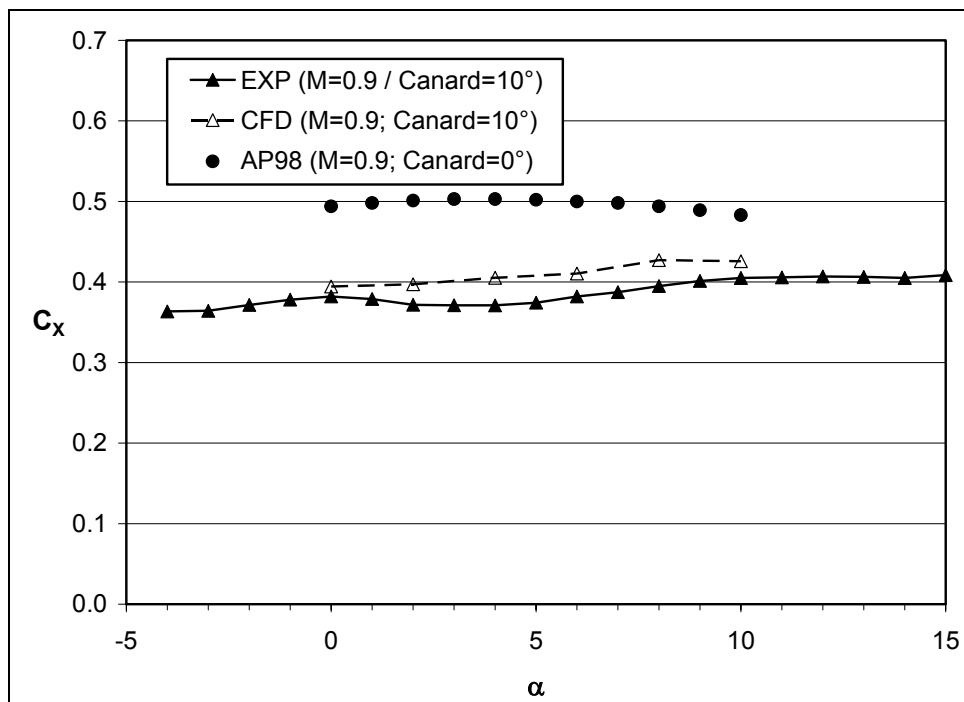


Figure A-6. Axial force for the planar fin case at Mach 0.9.

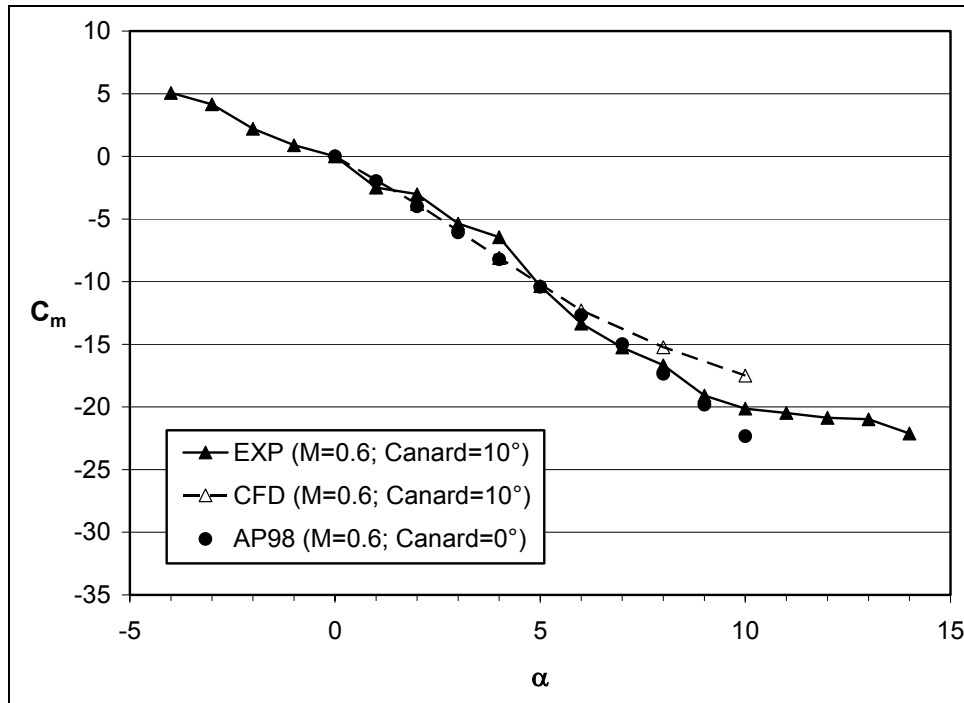


Figure A-7. Pitching moment about the nose for the planar fin case at Mach 0.6.

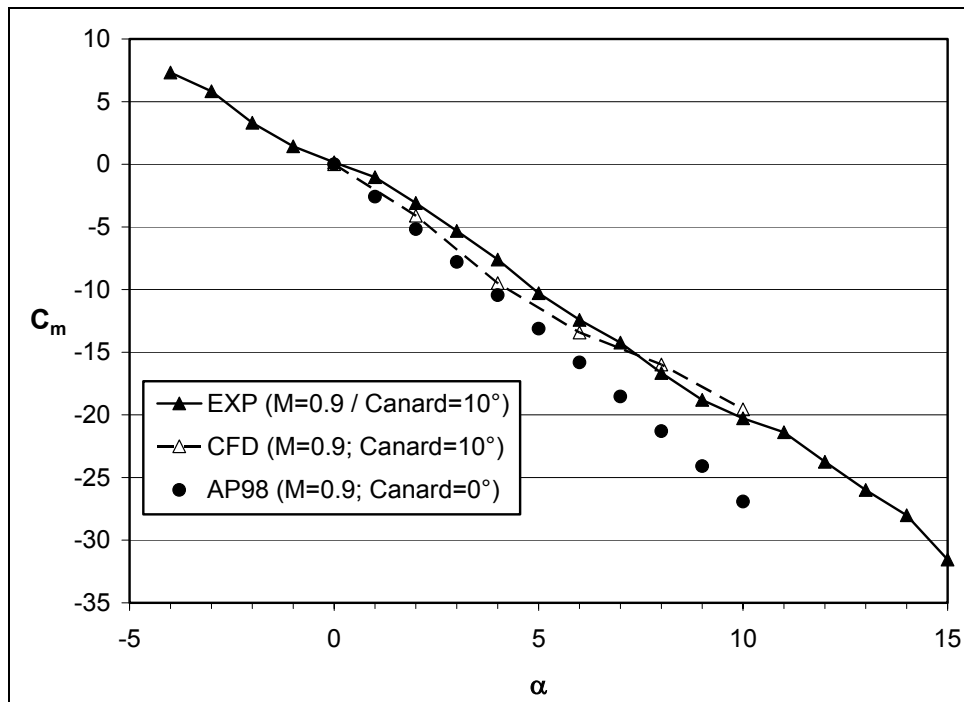


Figure A-8. Pitching moment about the nose for the planar fin case at Mach 0.9.

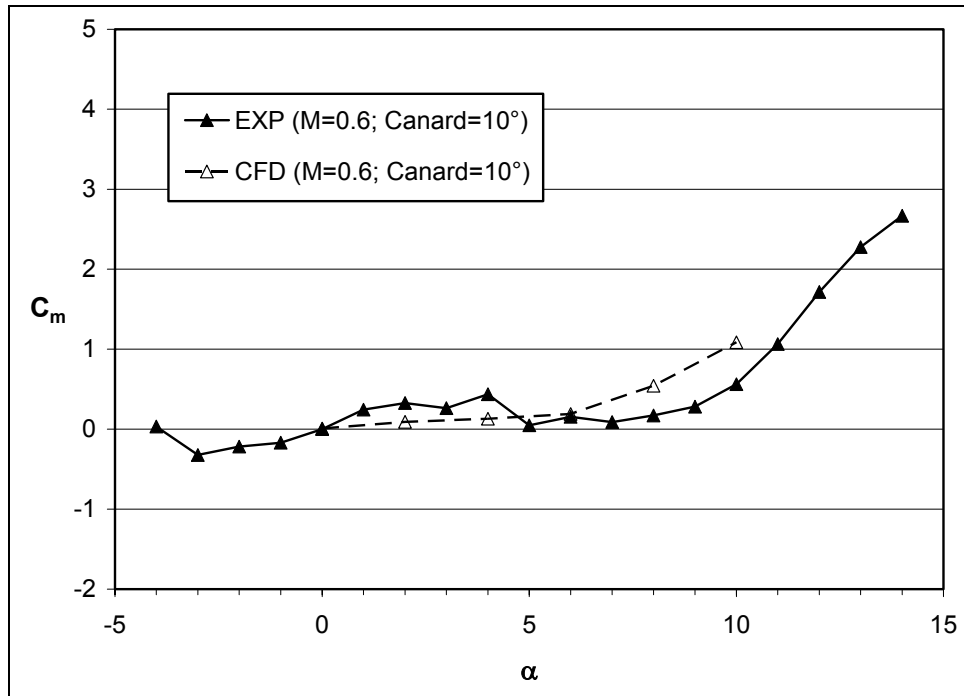


Figure A-9. Pitching moment about the moment reference point (MRP) for the planar fin case at Mach 0.6.

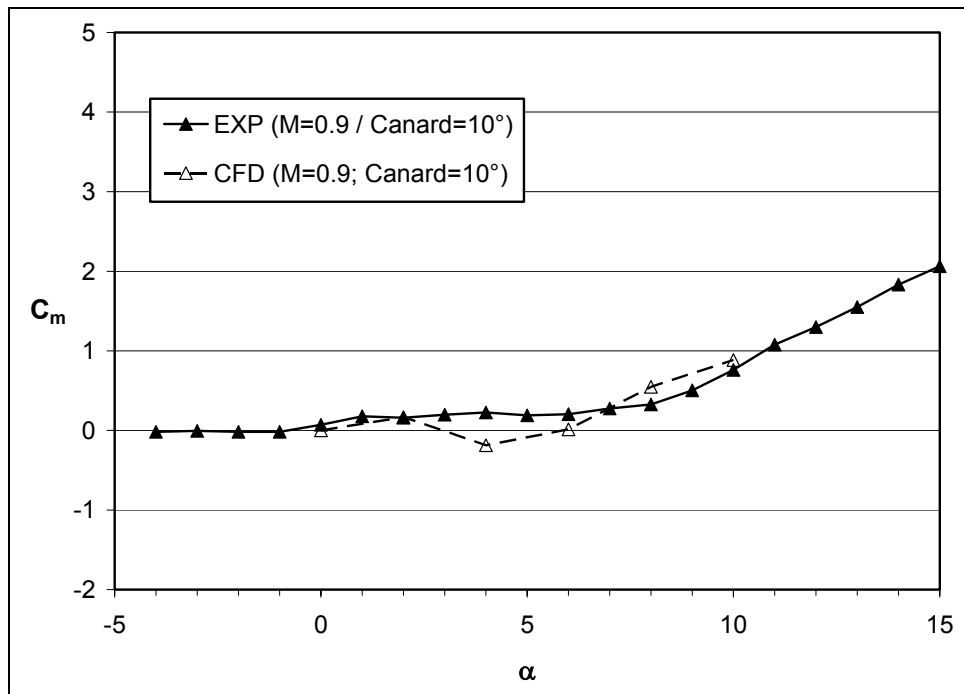


Figure A-10. Pitching moment about the MRP for the planar fin case at Mach 0.9.

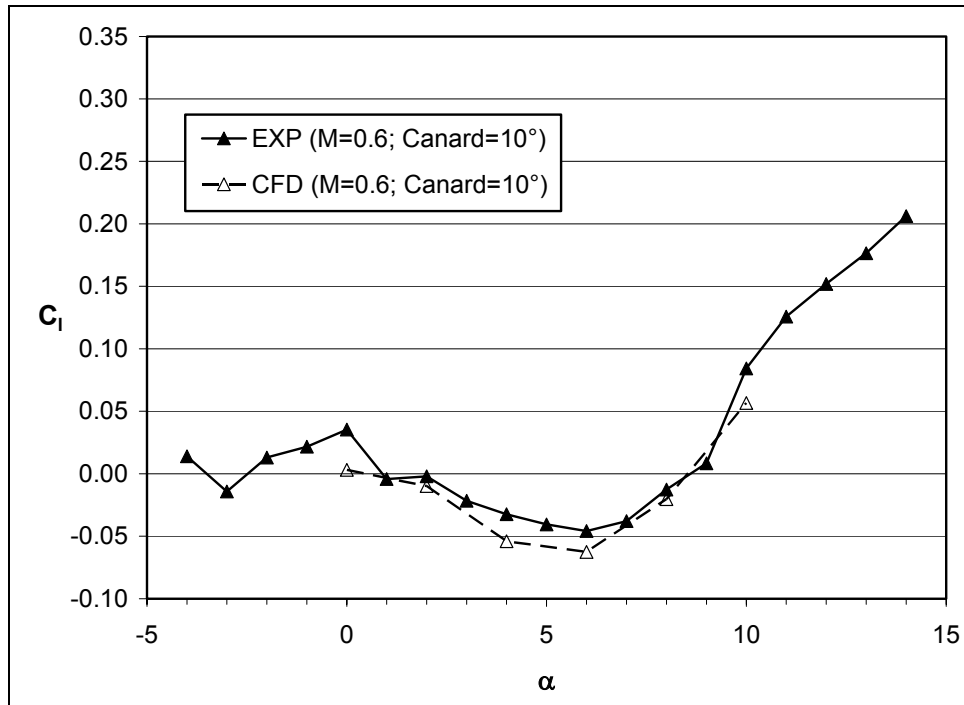


Figure A-11. Rolling moment for the planar fin case at Mach 0.6.

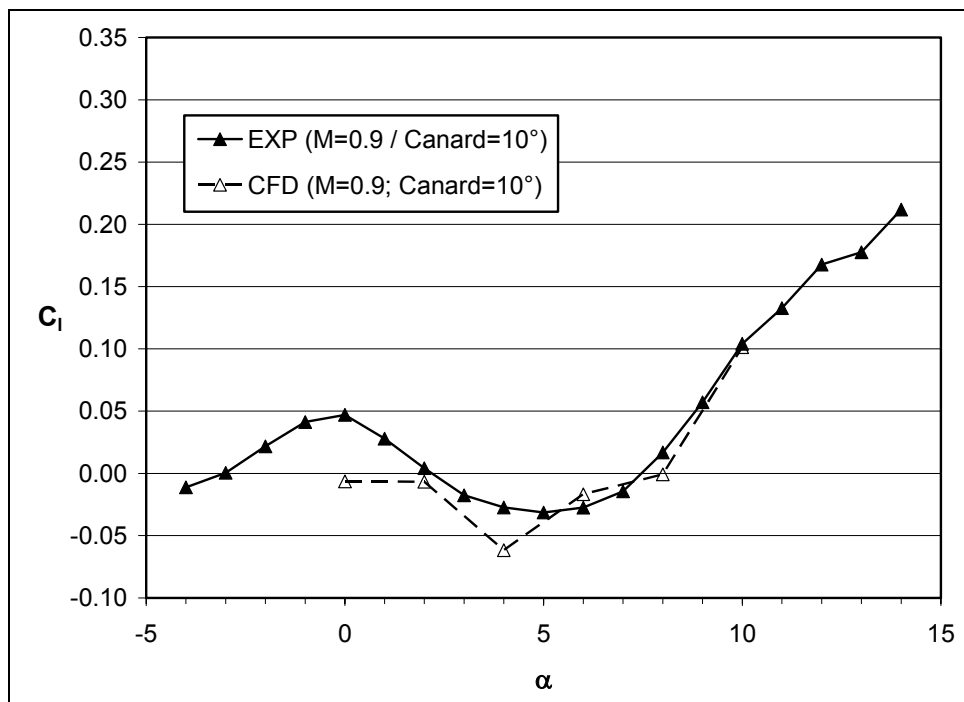


Figure A-12. Rolling moment for the planar fin case at Mach 0.9.

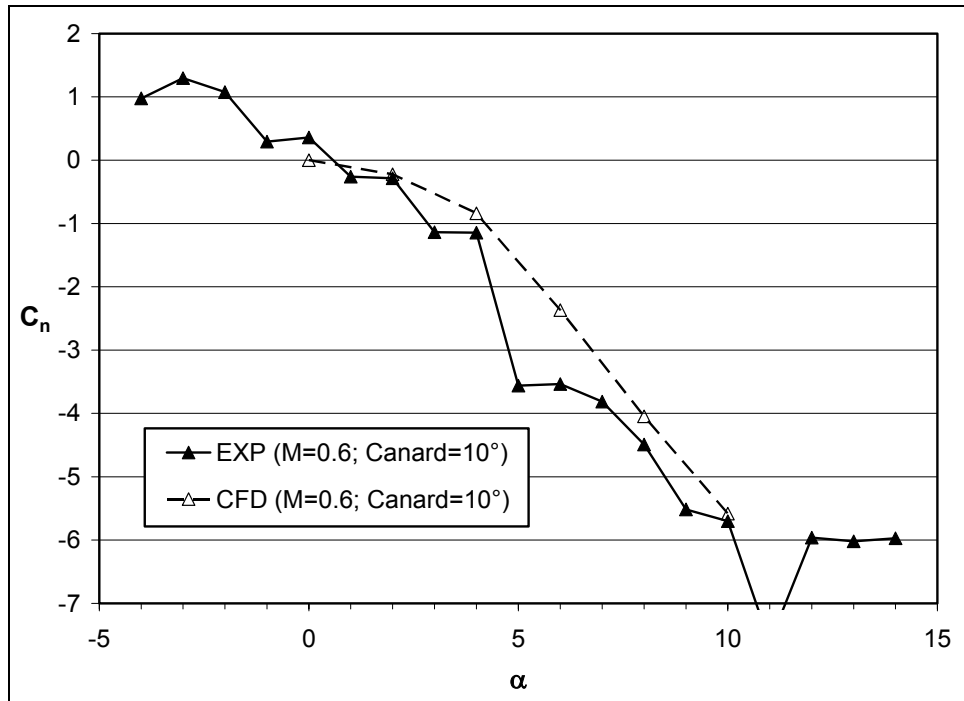


Figure A-13. Yawing moment about the nose for the planar fin case at Mach 0.6.

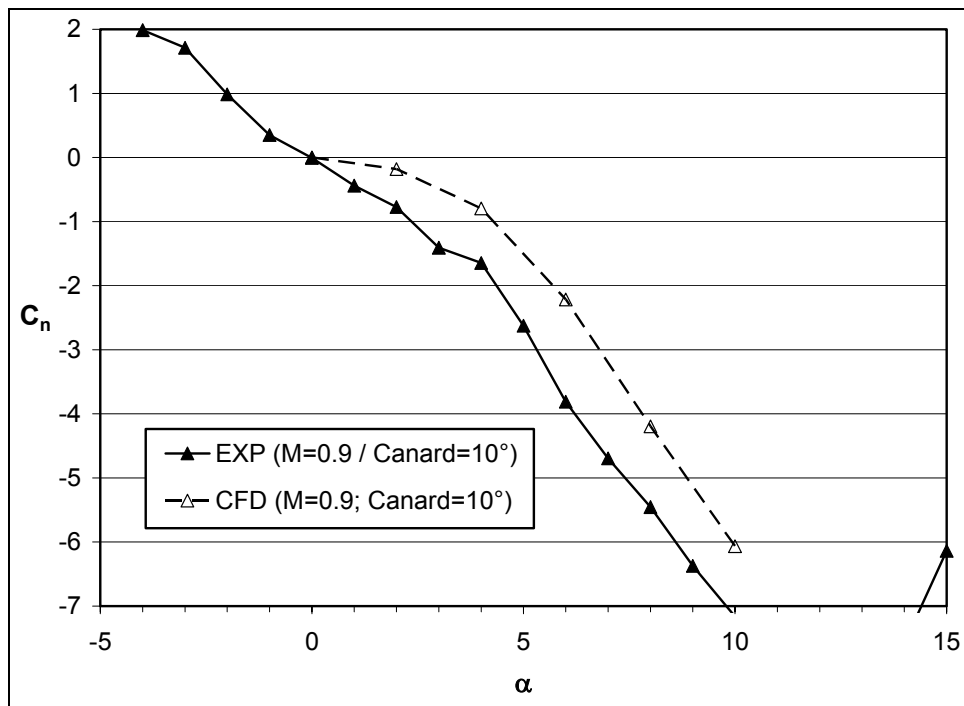


Figure A-14. Yawing moment about the nose for the planar fin case at Mach 0.9.

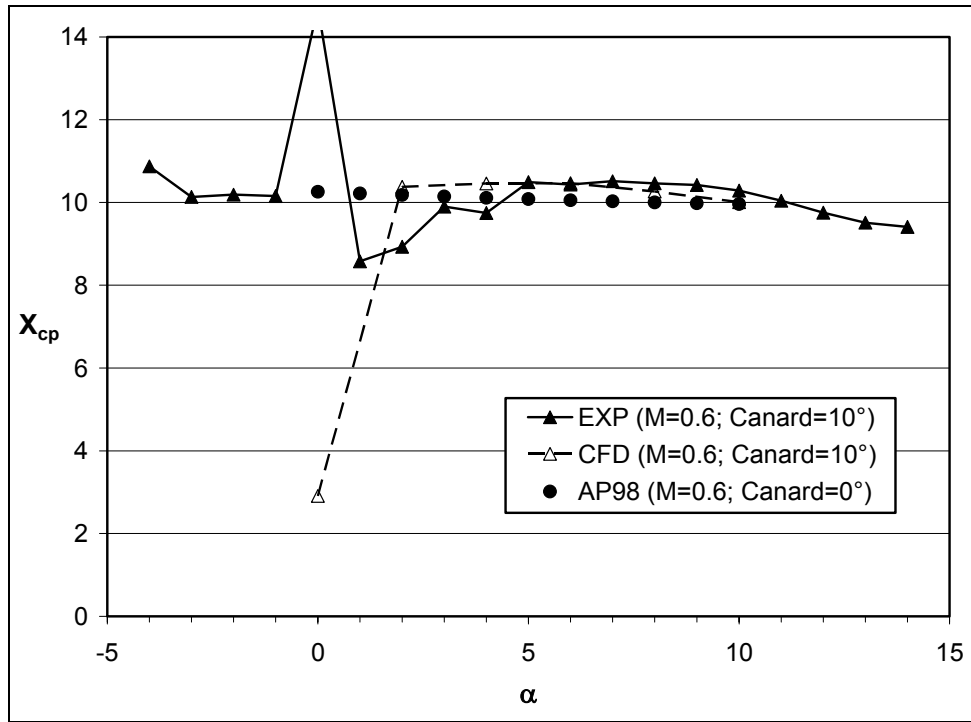


Figure A-15. Center of pressure location from the nose for the planar fin case at Mach 0.6.

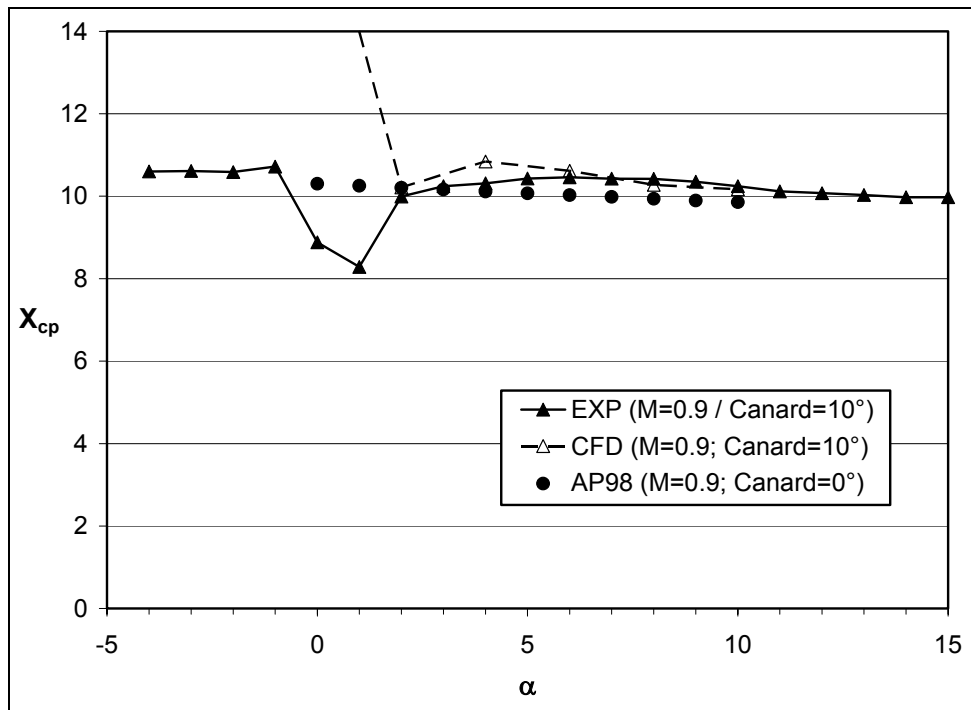


Figure A-16. Center of pressure location from the nose for the planar fin case at Mach 0.9.

INTENTIONALLY LEFT BLANK.

Appendix B. Aerodynamic Coefficients for Grid Fin Case

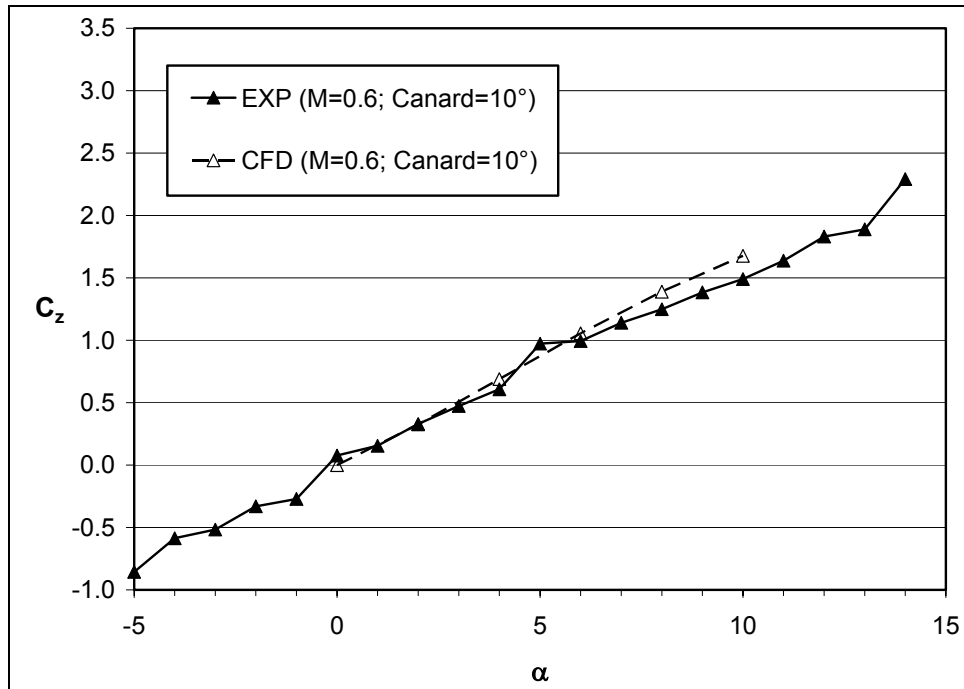


Figure B-1. Normal force for the grid fin case at Mach 0.6.

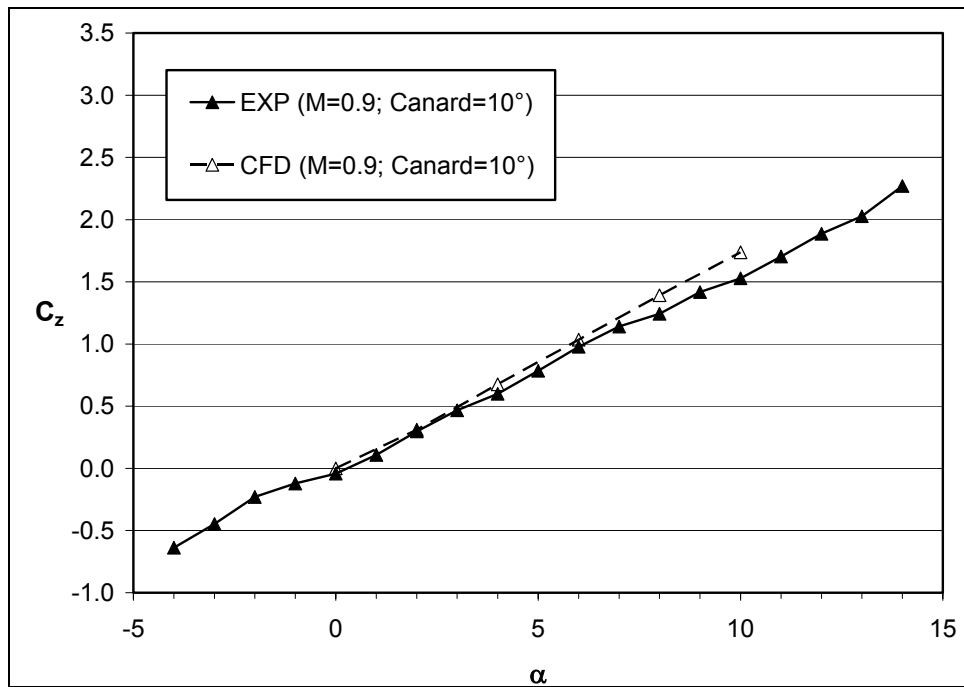


Figure B-2. Normal force for the grid fin case at Mach 0.9.

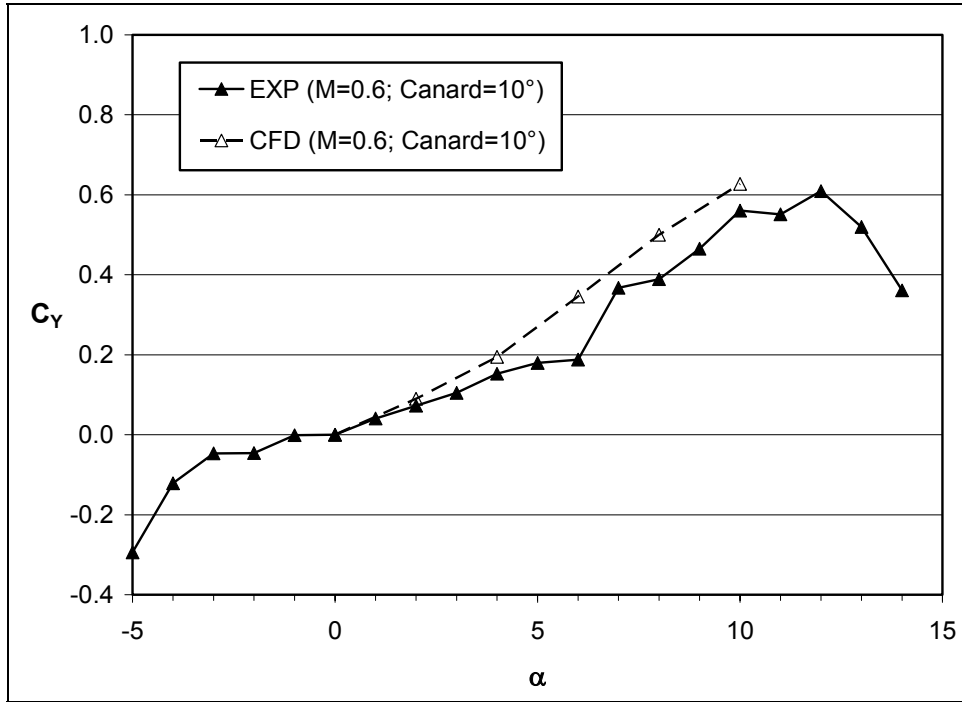


Figure B-3. Side force for the grid fin case at Mach 0.6.

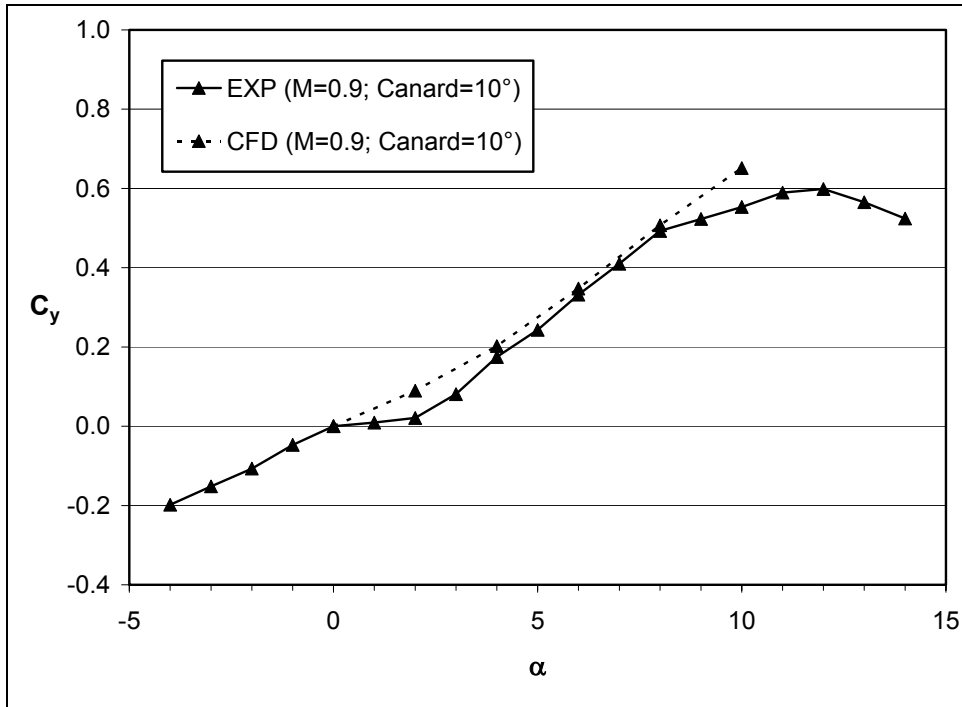


Figure B-4. Side force for the grid fin case at Mach 0.9.

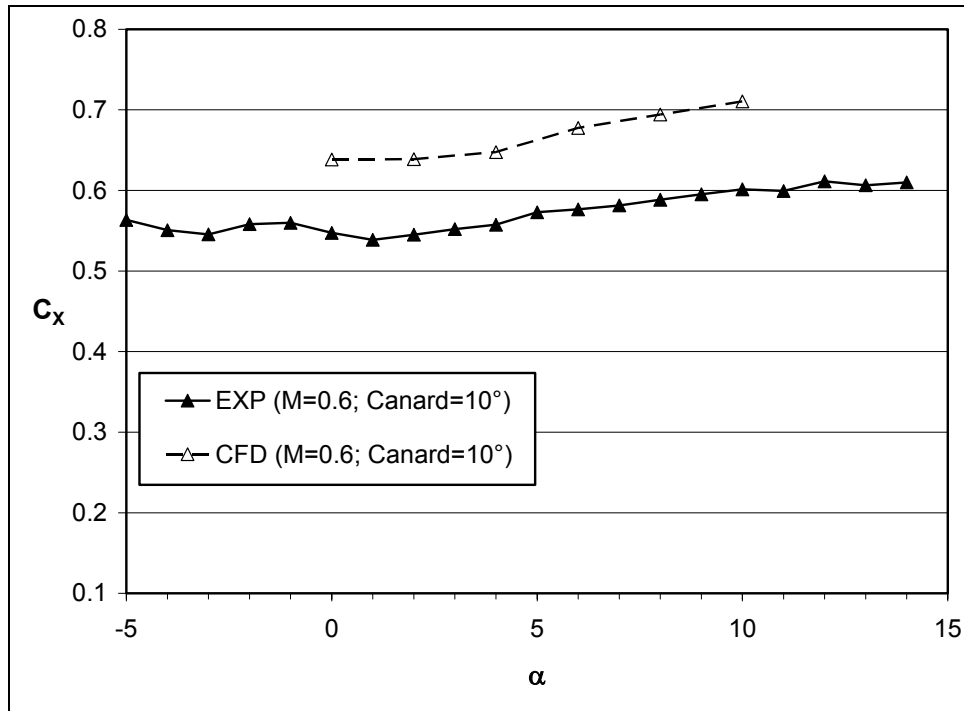


Figure B-5. Axial force for the grid fin case at Mach 0.6.

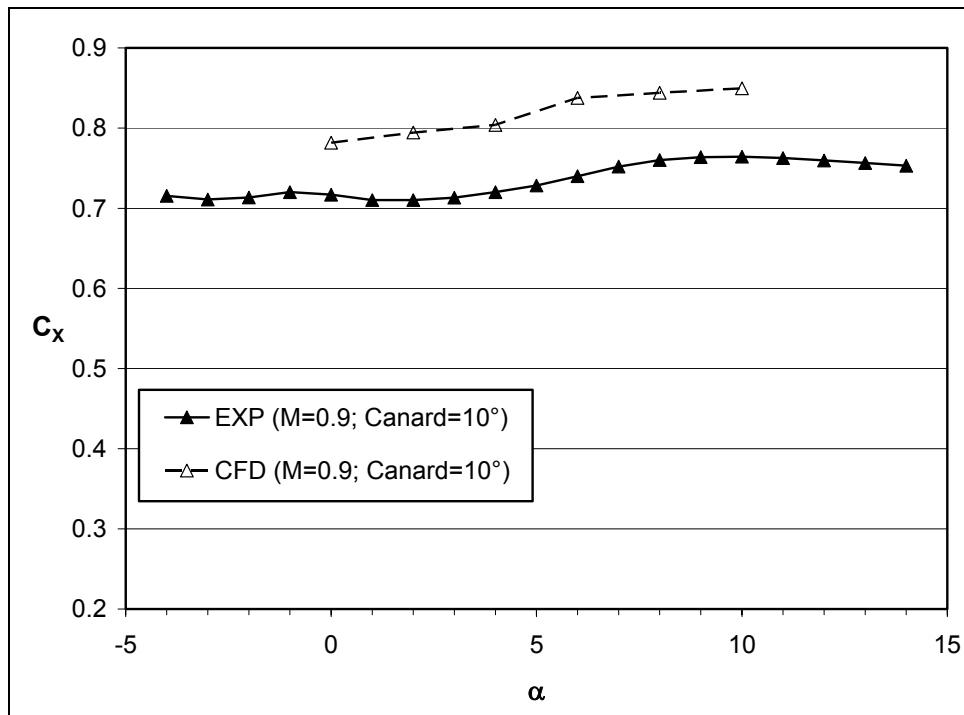


Figure B-6. Axial force for the grid fin case at Mach 0.9.

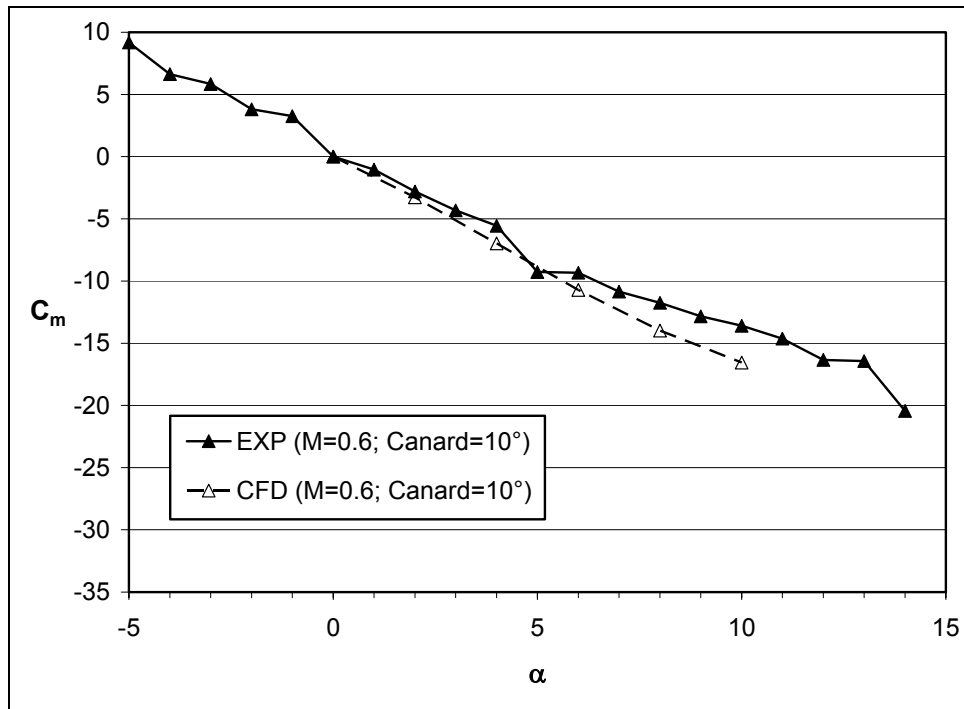


Figure B-7. Pitching moment about the nose for the grid fin case at Mach 0.6.

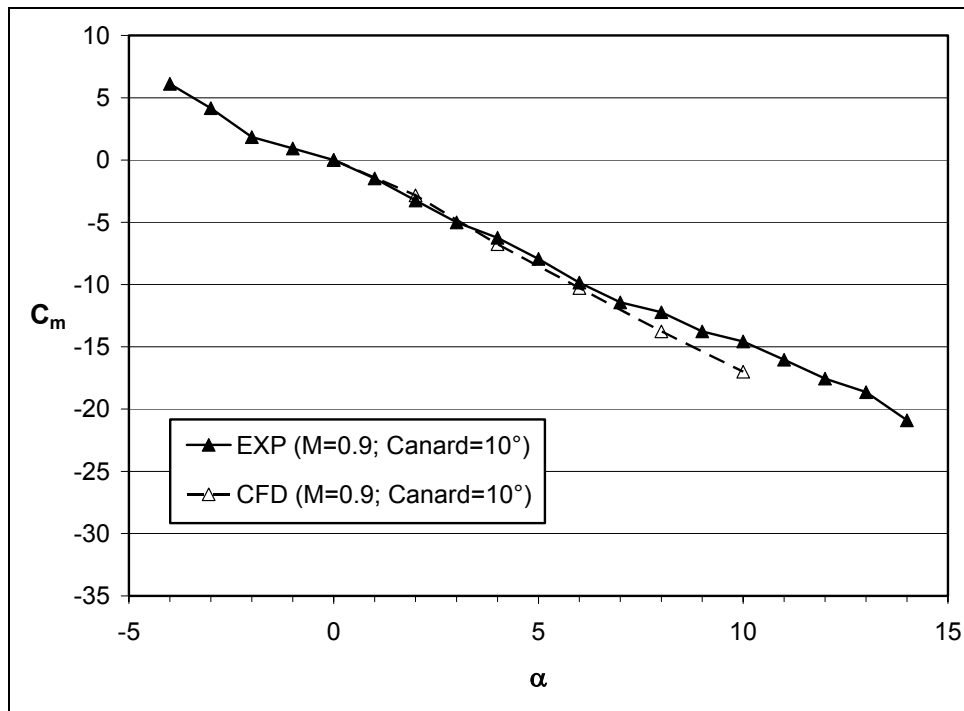


Figure B-8. Pitching moment about the nose for the grid fin case at Mach 0.9.

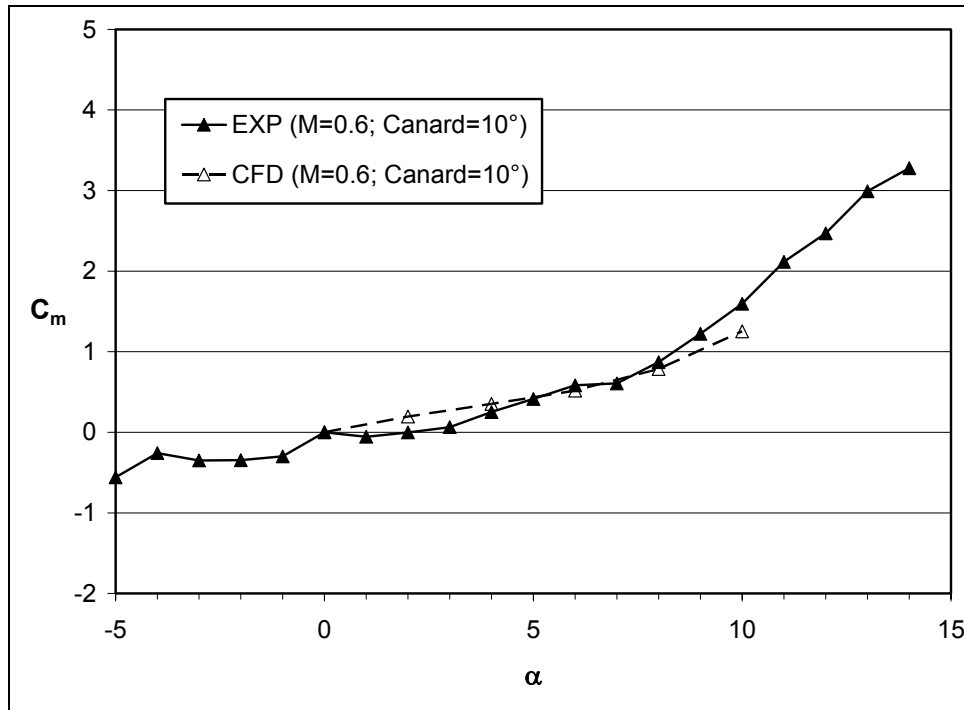


Figure B-9. Pitching moment about the moment reference point (MRP) for the grid fin case at Mach 0.6.

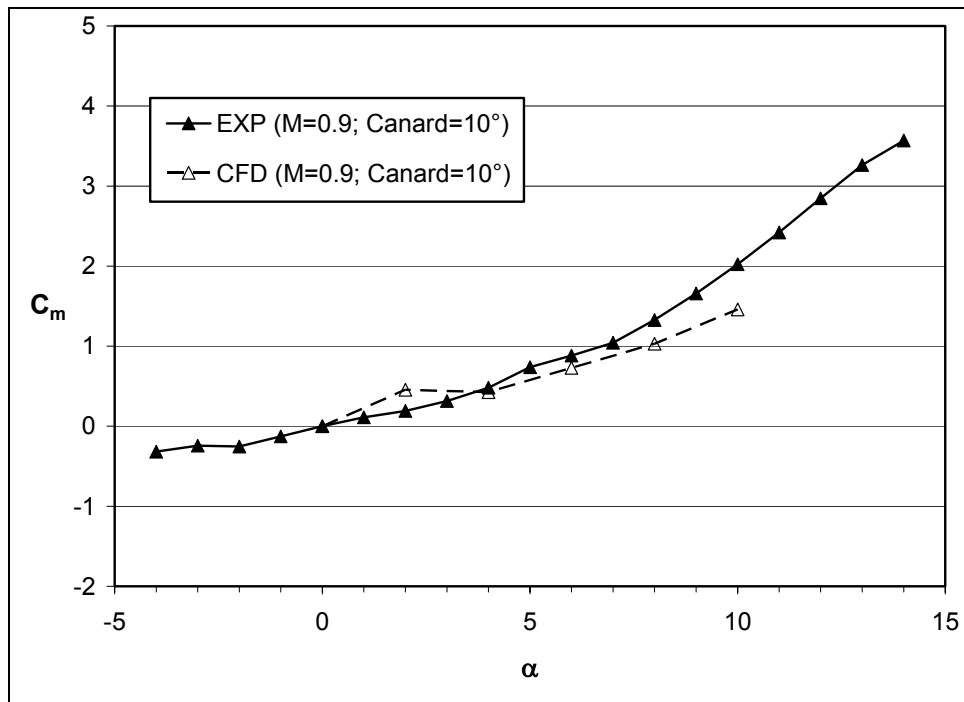


Figure B-10. Pitching moment about the MRP for the grid fin case at Mach 0.9.

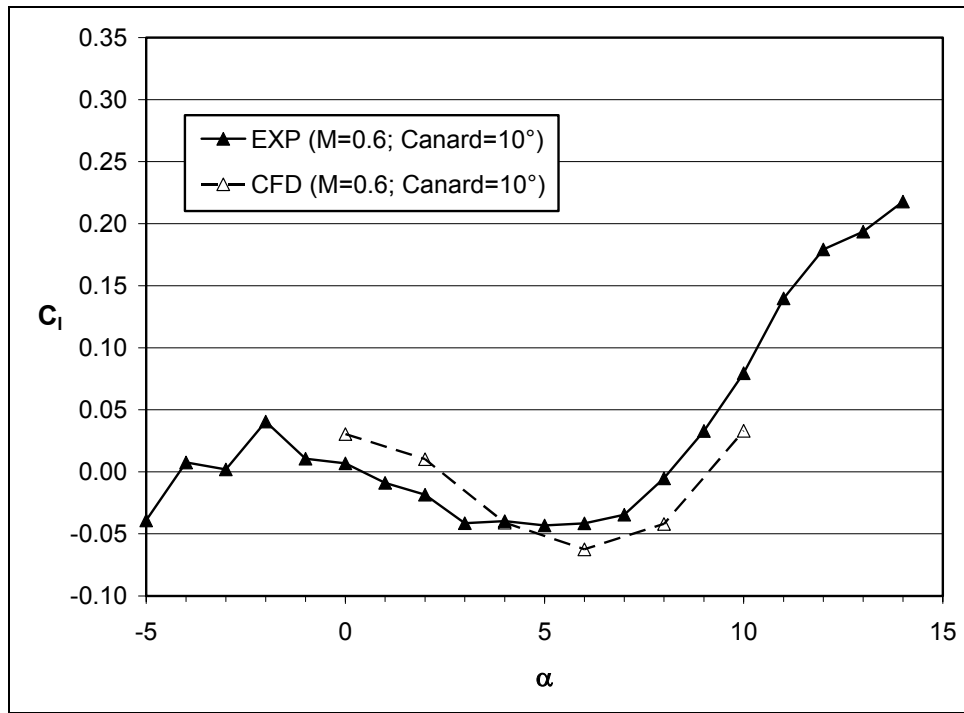


Figure B-11. Rolling moment for the grid fin case at Mach 0.6.

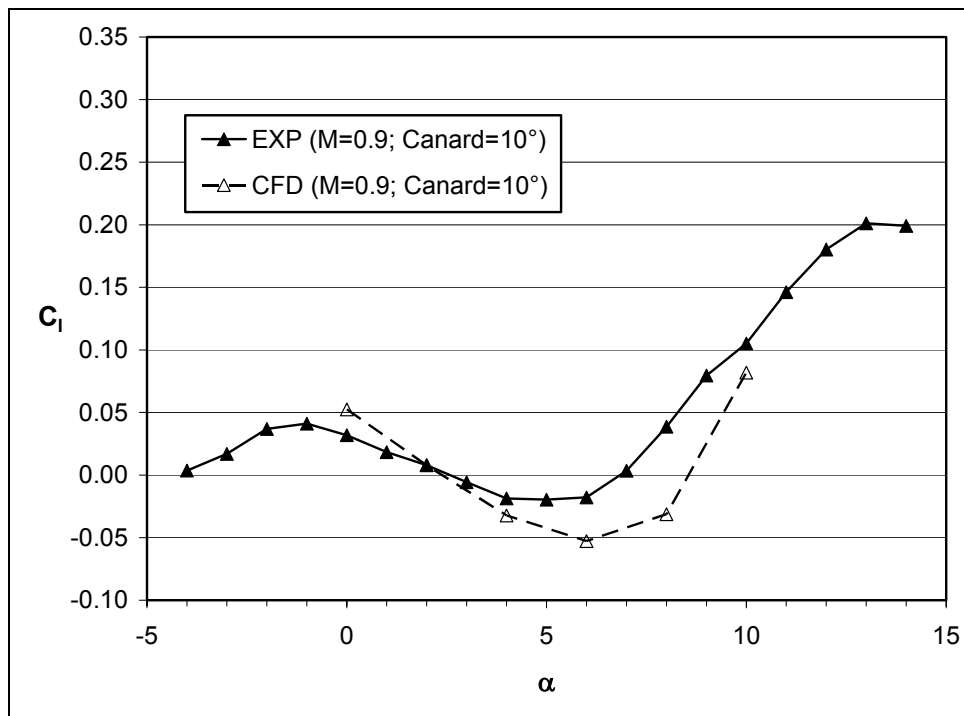


Figure B-12. Rolling moment for the grid fin case at Mach 0.9.

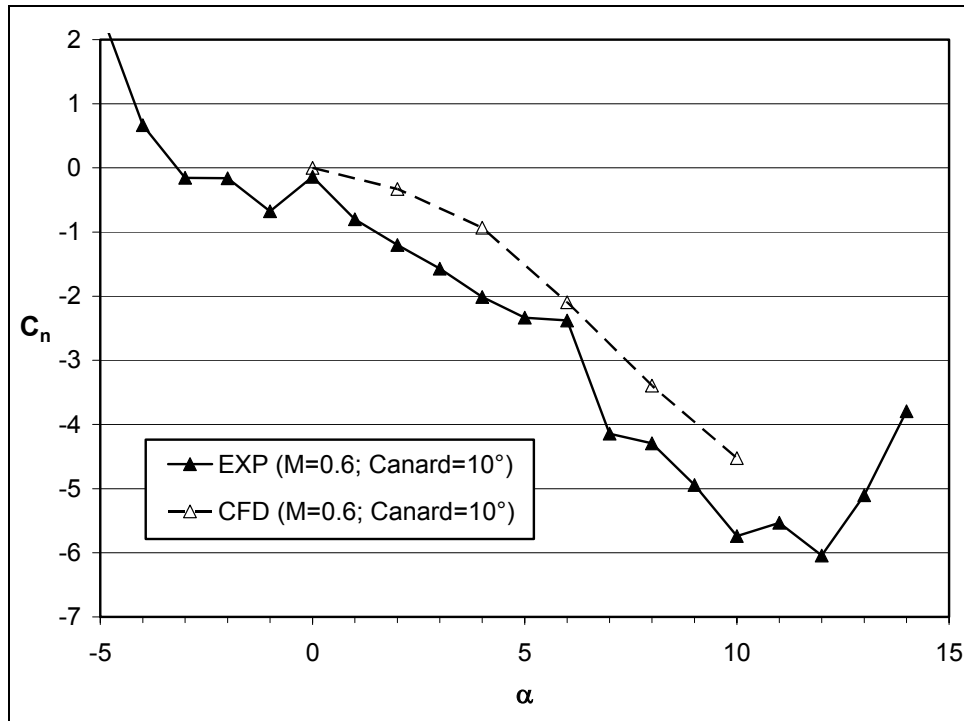


Figure B-13. Yawing moment about the nose for the grid fin case at Mach 0.6.

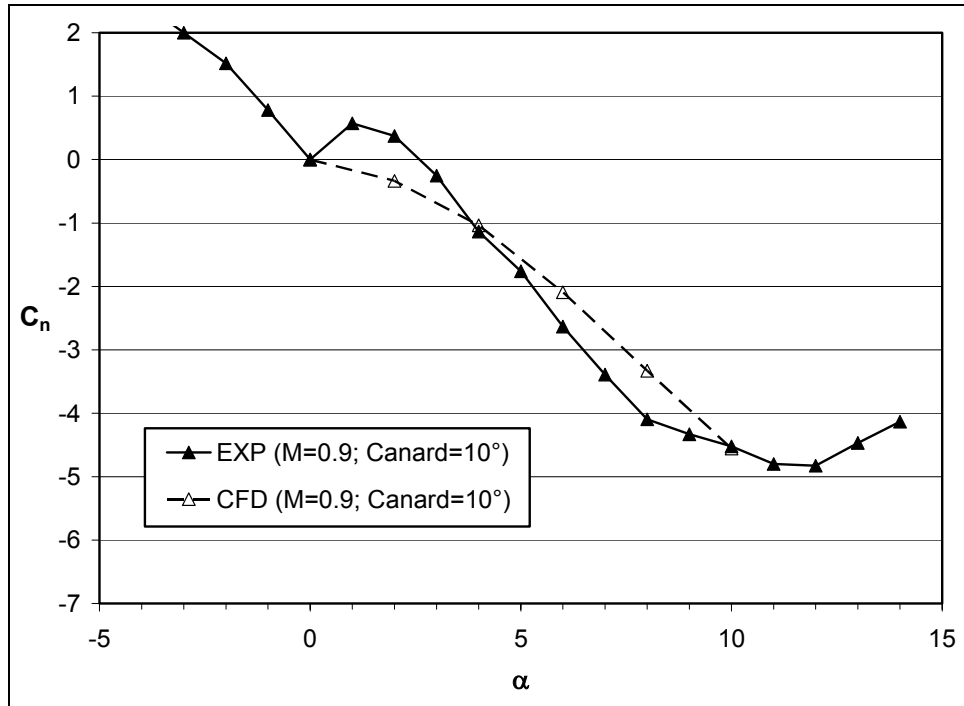


Figure B-14. Yawing moment about the nose for the grid fin case at Mach 0.9.

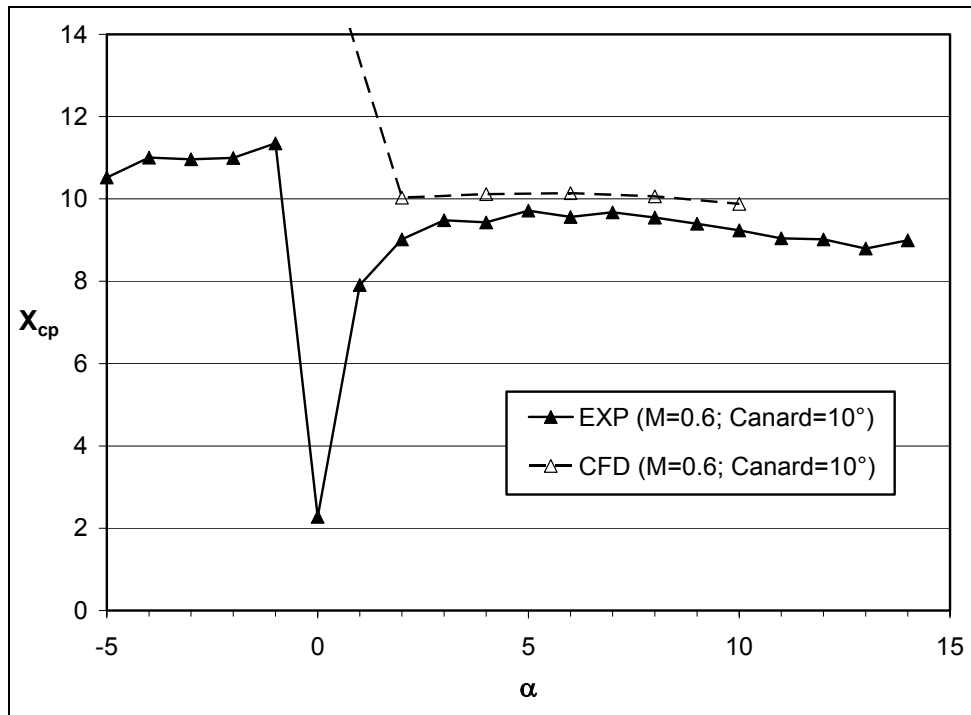


Figure B-15. Center of pressure location from the nose for the grid fin case at Mach 0.6.

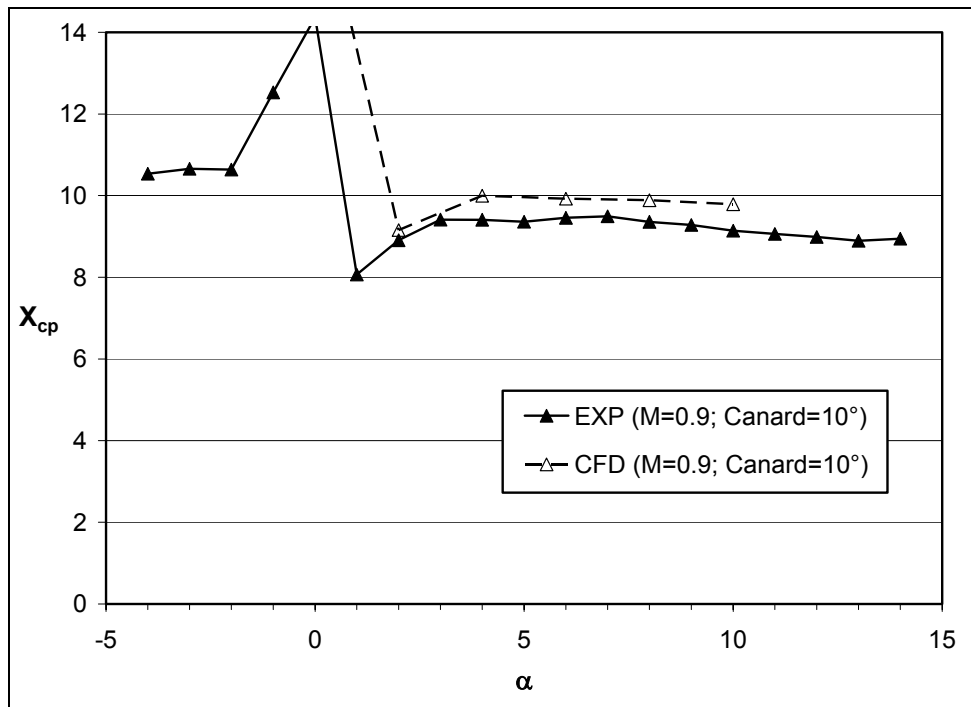


Figure B-16. Center of pressure location from the nose for the grid fin case at Mach 0.9.

INTENTIONALLY LEFT BLANK.

Appendix C. Force Coefficients on Canards

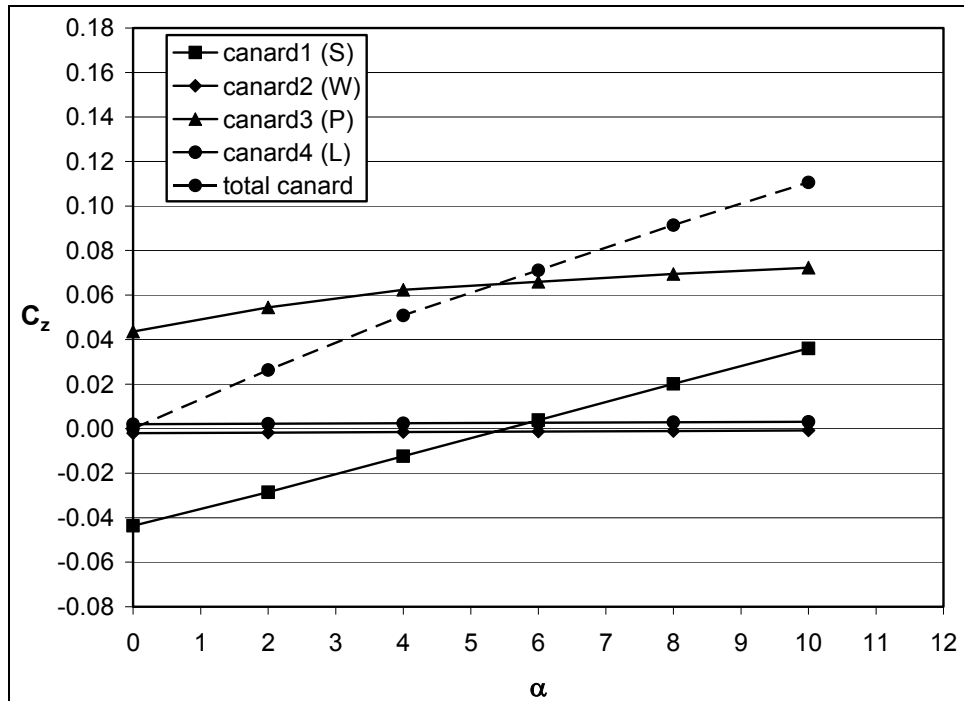


Figure C-1. Canard normal force, $\delta = 10^\circ$, Mach 0.6.

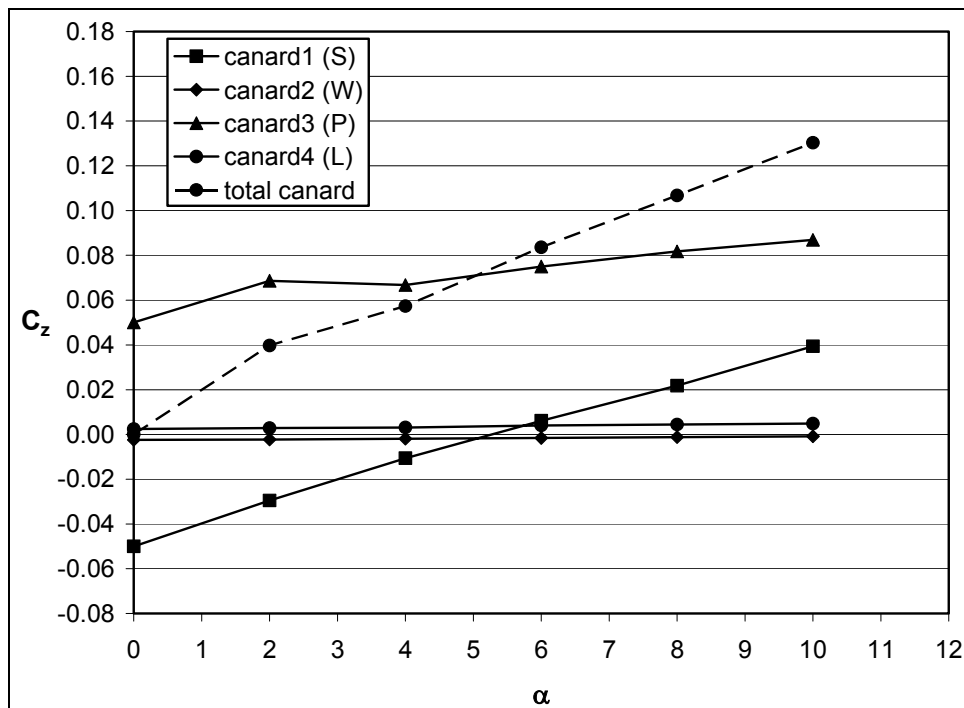


Figure C-2. Canard normal force, $\delta = 10^\circ$, Mach 0.9.

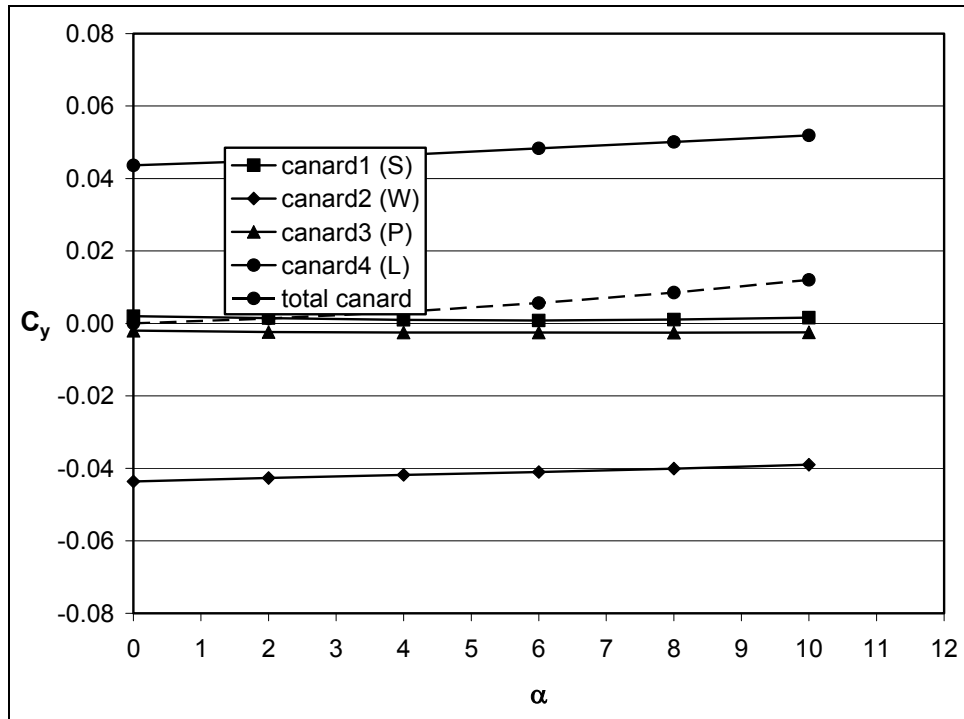


Figure C-3. Canard side force, $\delta = 10^\circ$, Mach 0.6.

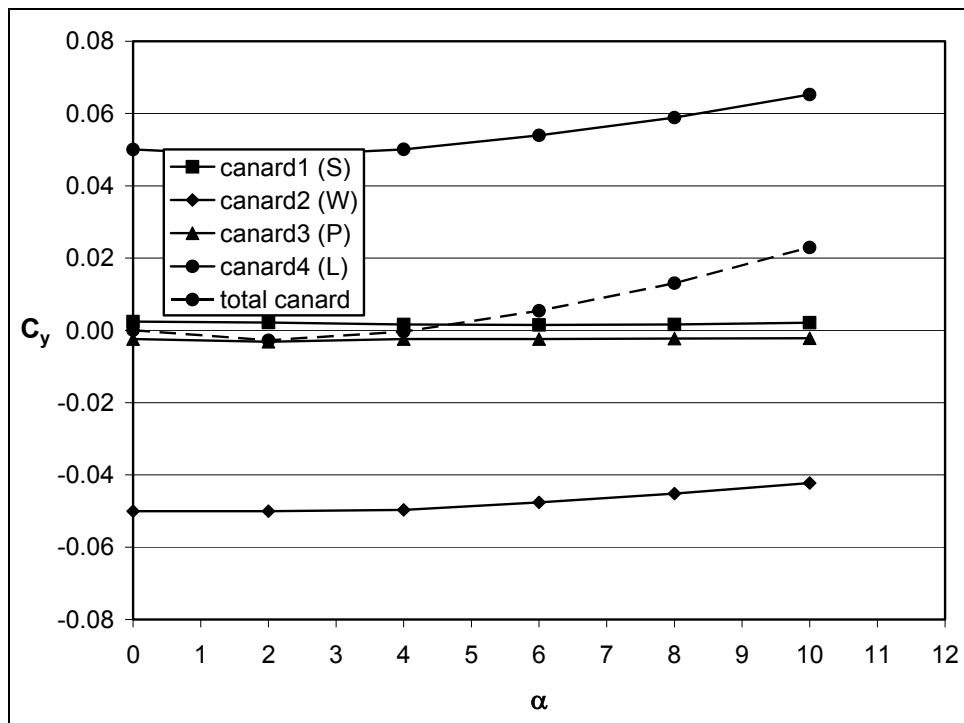


Figure C-4. Canard side force, $\delta = 10^\circ$, Mach 0.9.

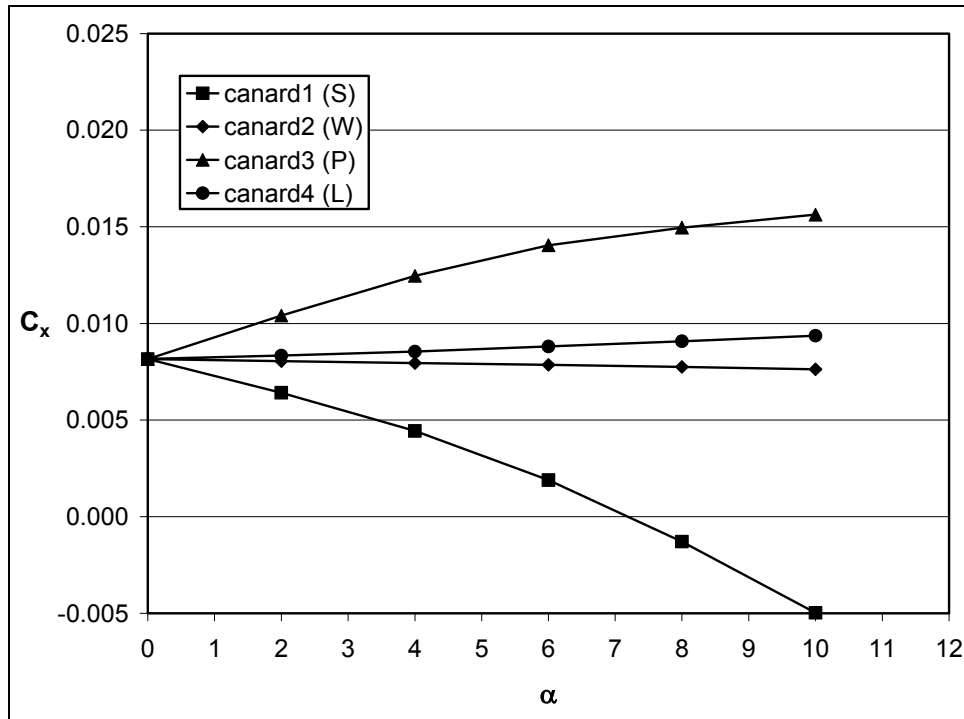


Figure C-5. Canard axial force, $\delta = 10^\circ$, Mach 0.6.

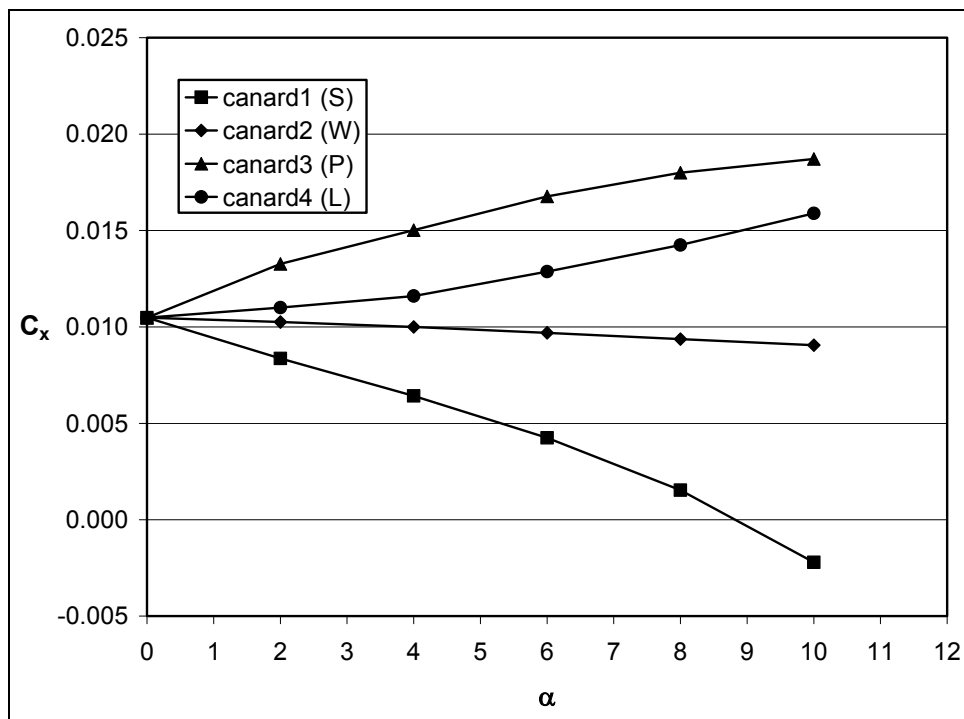


Figure C-6. Canard axial force, $\delta = 10^\circ$, Mach 0.9.

Table C-1. Aerodynamic coefficients on canards, planar fin case, $\delta = 10^\circ$, Mach 0.6.

α	0	2	4	6	8	10
Axial Force						
Canard 1 (S)	0.0082	0.0064	0.0044	0.0019	-0.0013	-0.0050
Canard 2 (W)	0.0082	0.0081	0.0080	0.0079	0.0077	0.0076
Canard 3 (P)	0.0082	0.0104	0.0125	0.0140	0.0150	0.0156
Canard 4 (L)	0.0082	0.0083	0.0085	0.0088	0.0091	0.0094
Total canard	0.0326	0.0332	0.0334	0.0326	0.0305	0.0276
Side Force						
Canard 1 (S)	0.0020	0.0014	0.0010	0.0008	0.0010	0.0016
Canard 2 (W)	-0.0436	-0.0427	-0.0418	-0.0410	-0.0401	-0.0390
Canard 3 (P)	-0.0020	-0.0024	-0.0025	-0.0025	-0.0025	-0.0024
Canard 4 (L)	0.0436	0.0449	0.0465	0.0483	0.0501	0.0519
Total canard	0.0000	0.0014	0.0032	0.0056	0.0085	0.0120
Normal Force						
Canard 1 (S)	-0.0436	-0.0286	-0.0124	0.0039	0.0201	0.0360
Canard 2 (W)	-0.0020	-0.0018	-0.0015	-0.0013	-0.0011	-0.0008
Canard 3 (P)	0.0436	0.0545	0.0623	0.0659	0.0695	0.0723
Canard 4 (L)	0.0020	0.0022	0.0024	0.0027	0.0029	0.0031
Total canard	0.0000	0.0263	0.0509	0.0711	0.0914	0.1106

Notes: S = starboard; W = windward; P = port; L = leeward.

Table C-2. Aerodynamic coefficients on canards, planar fin case, $\delta = 10^\circ$, Mach 0.9.

α	0	2	4	6	8	10
Axial Force						
Canard 1 (S)	0.0105	0.0084	0.0064	0.0042	0.0015	-0.0022
Canard 2 (W)	0.0105	0.0102	0.0100	0.0097	0.0094	0.0091
Canard 3 (P)	0.0105	0.0133	0.0150	0.0168	0.0180	0.0187
Canard 4 (L)	0.0105	0.0110	0.0116	0.0129	0.0142	0.0159
Total canard	0.0419	0.0429	0.0430	0.0436	0.0432	0.0414
Side Force						
Canard 1 (S)	0.0024	0.0022	0.0016	0.0015	0.0016	0.0021
Canard 2 (W)	-0.0500	-0.0500	-0.0497	-0.0476	-0.0452	-0.0423
Canard 3 (P)	-0.0024	-0.0032	-0.0024	-0.0024	-0.0023	-0.0022
Canard 4 (L)	0.0500	0.0483	0.0501	0.0540	0.0589	0.0652
Total canard	0.0000	-0.0027	-0.0004	0.0054	0.0130	0.0229
Normal Force						
Canard 1 (S)	-0.0500	-0.0295	-0.0106	0.0061	0.0218	0.0394
Canard 2 (W)	-0.0024	-0.0023	-0.0019	-0.0016	-0.0012	-0.0008
Canard 3 (P)	0.0500	0.0686	0.0668	0.0750	0.0817	0.0869
Canard 4 (L)	0.0024	0.0028	0.0031	0.0040	0.0044	0.0048
Total canard	0.0000	0.0397	0.0573	0.0836	0.1067	0.1303

Notes: S = starboard; W = windward; P = port; L = leeward.

INTENTIONALLY LEFT BLANK.

Appendix D. Force Coefficients on Planar Fins

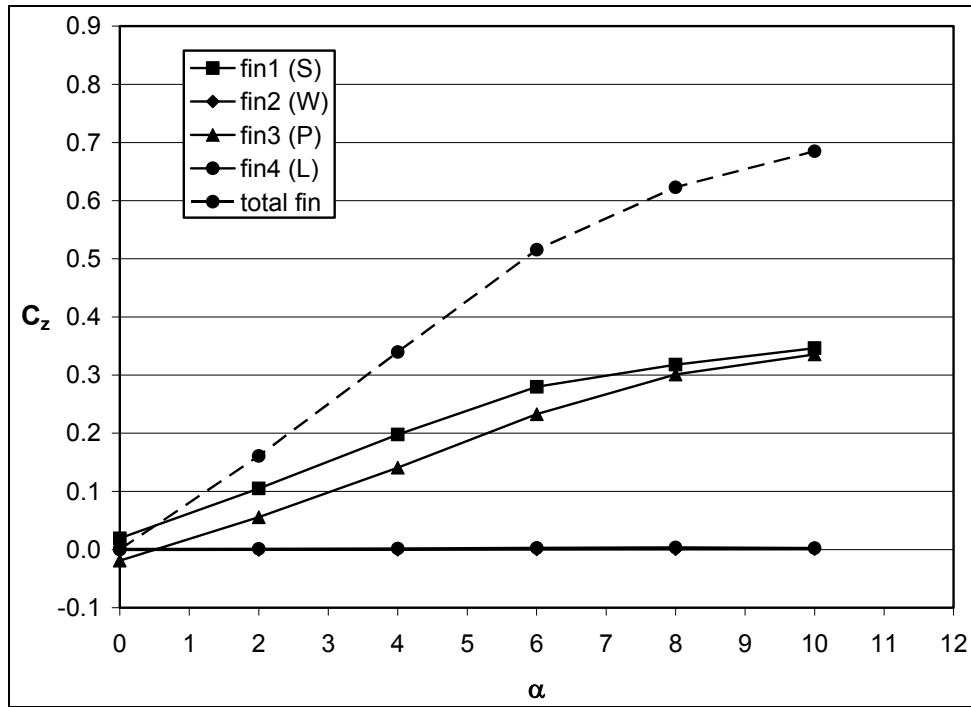


Figure D-1. Planar fin normal force, $\delta = 10^\circ$, Mach 0.6.

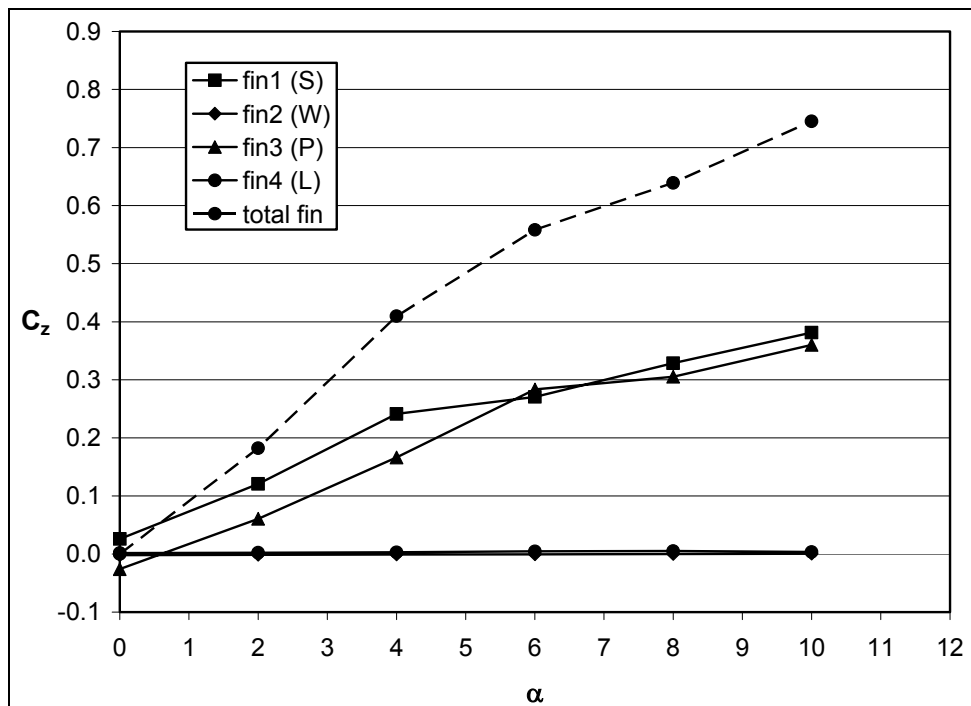


Figure D-2. Planar fin normal force, $\delta = 10^\circ$, Mach 0.9.

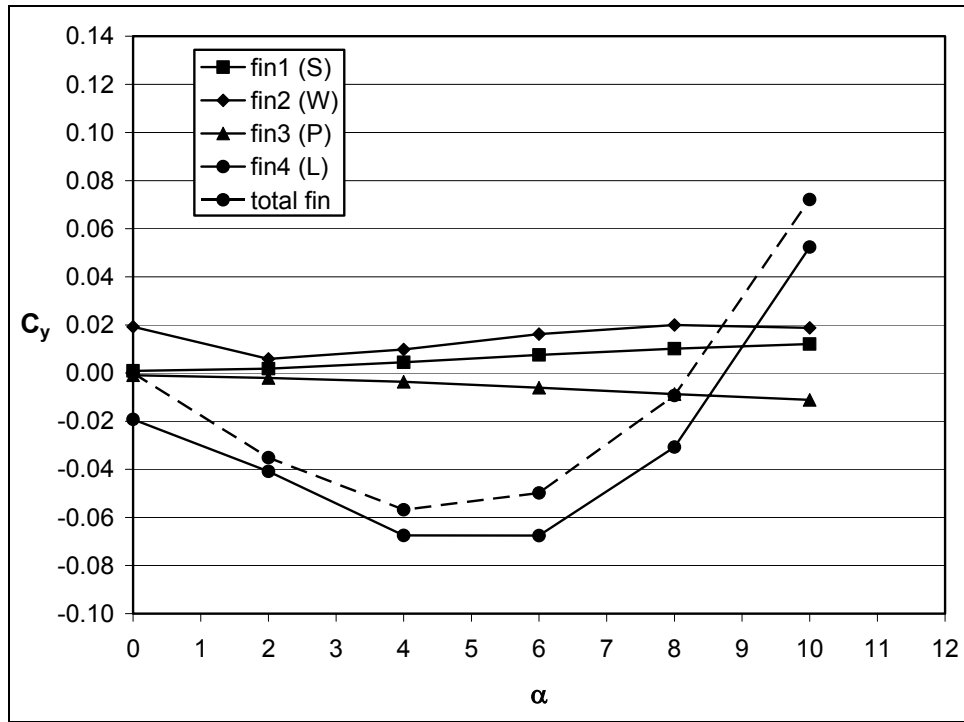


Figure D-3. Planar fin side force, $\delta = 10^\circ$, Mach 0.6.

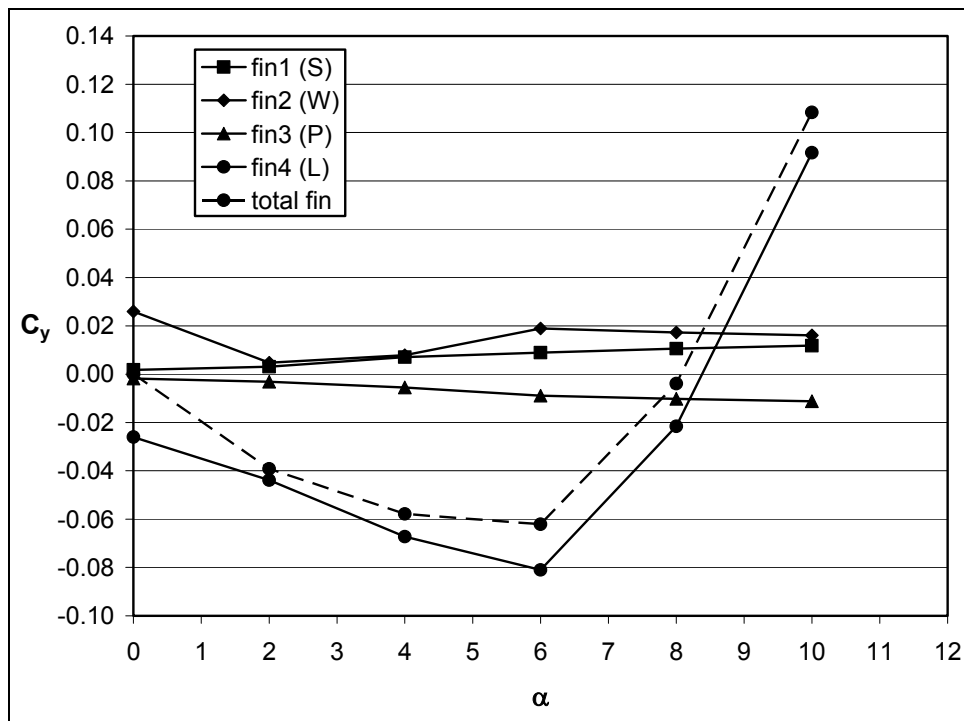


Figure D-4. Planar fin side force, $\delta = 10^\circ$, Mach 0.9.

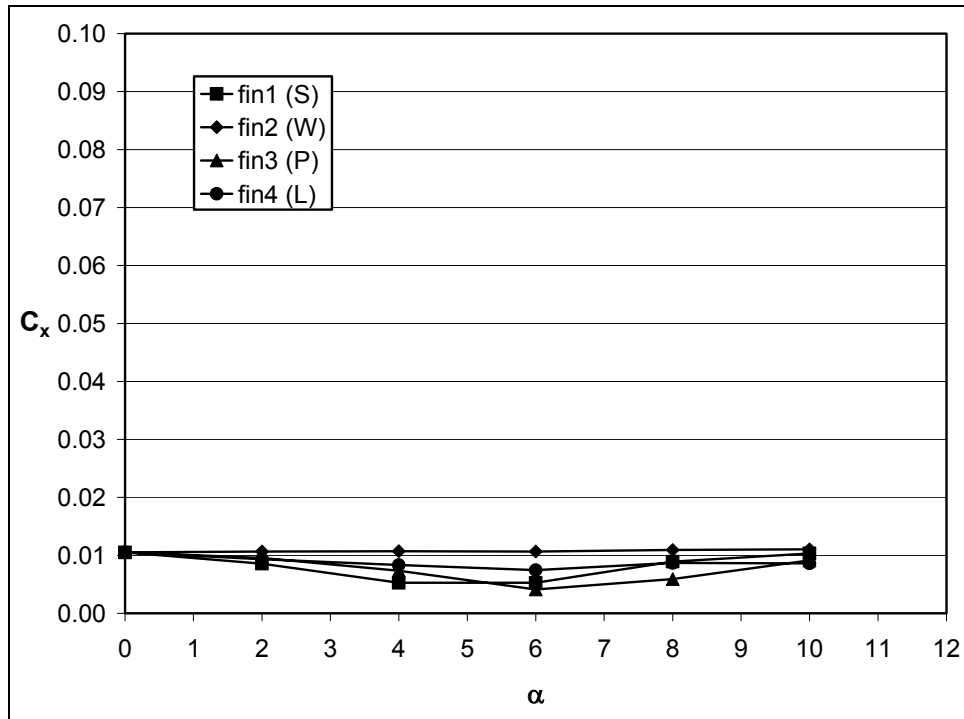


Figure D-5. Planar fin axial force, $\delta = 10^\circ$, Mach 0.6.

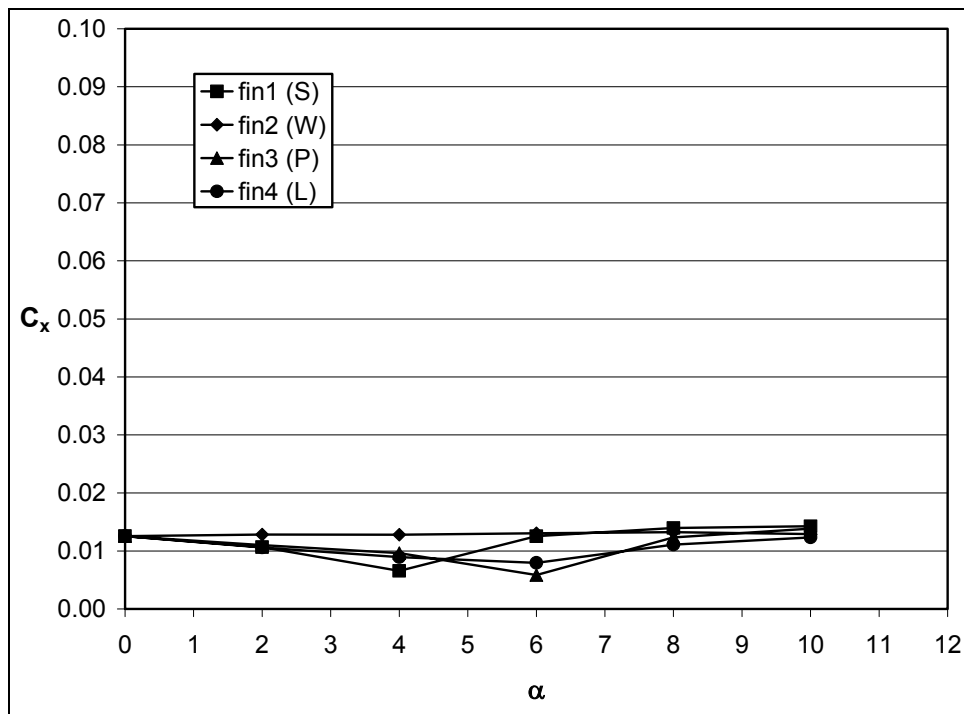


Figure D-6. Planar fin axial force, $\delta = 10^\circ$, Mach 0.9.

Table D-1. Aerodynamic coefficients on planar fins, $\delta = 10^\circ$, Mach 0.6.

α	0	2	4	6	8	10
Axial Force						
Fin 1 (S)	0.0105	0.0086	0.0053	0.0053	0.0089	0.0103
Fin 2 (W)	0.0105	0.0107	0.0107	0.0107	0.0109	0.0110
Fin 3 (P)	0.0105	0.0095	0.0073	0.0041	0.0059	0.0091
Fin 4 (L)	0.0105	0.0093	0.0083	0.0074	0.0087	0.0086
Total fin	0.0420	0.0381	0.0316	0.0275	0.0344	0.0391
Side Force						
Fin 1 (S)	0.0009	0.0019	0.0045	0.0076	0.0101	0.0121
Fin 2 (W)	0.0192	0.0059	0.0099	0.0162	0.0200	0.0188
Fin 3 (P)	-0.0009	-0.0020	-0.0036	-0.0061	-0.0087	-0.0111
Fin 4 (L)	-0.0192	-0.0409	-0.0675	-0.0675	-0.0308	0.0524
Total fin	0.0000	-0.0351	-0.0568	-0.0498	-0.0094	0.0721
Normal Force						
Fin 1 (S)	0.0192	0.1049	0.1976	0.2799	0.3181	0.3463
Fin 2 (W)	-0.0009	-0.0006	-0.0003	0.0001	0.0003	0.0006
Fin 3 (P)	-0.0192	0.0555	0.1407	0.2328	0.3010	0.3355
Fin 4 (L)	0.0009	0.0012	0.0017	0.0029	0.0034	0.0024
Total fin	0.0000	0.1610	0.3397	0.5156	0.6228	0.6849

Notes: S = starboard; W = windward; P = port; L = leeward.

Table D-2. Aerodynamic coefficients on planar fins, $\delta = 10^\circ$, Mach 0.9.

α	0	2	4	6	8	10
Axial Force						
Fin 1 (S)	0.0126	0.0107	0.0066	0.0125	0.0140	0.0143
Fin 2 (W)	0.0126	0.0128	0.0128	0.0131	0.0132	0.0129
Fin 3 (P)	0.0126	0.0110	0.0096	0.0058	0.0123	0.0139
Fin 4 (L)	0.0126	0.0106	0.0089	0.0080	0.0111	0.0123
Total fin	0.0502	0.0451	0.0379	0.0394	0.0506	0.0533
Side Force						
Fin 1 (S)	0.0018	0.0031	0.0070	0.0089	0.0106	0.0118
Fin 2 (W)	0.0260	0.0048	0.0079	0.0189	0.0172	0.0161
Fin 3 (P)	-0.0018	-0.0031	-0.0055	-0.0089	-0.0102	-0.0112
Fin 4 (L)	-0.0260	-0.0439	-0.0672	-0.0810	-0.0215	0.0917
Total fin	0.0000	-0.0392	-0.0578	-0.0621	-0.0039	0.1084
Normal Force						
Fin 1 (S)	0.0260	0.1208	0.2412	0.2707	0.3286	0.3812
Fin 2 (W)	-0.0018	-0.0014	-0.0009	-0.0005	-0.0002	0.0003
Fin 3 (P)	-0.0260	0.0608	0.1662	0.2835	0.3055	0.3601
Fin 4 (L)	0.0018	0.0021	0.0031	0.0045	0.0052	0.0036
Total fin	0.0000	0.1823	0.4095	0.5582	0.6391	0.7453

Notes: S = starboard; W = windward; P = port; L = leeward.

INTENTIONALLY LEFT BLANK.

Appendix E. Force Coefficients on Grid Fins

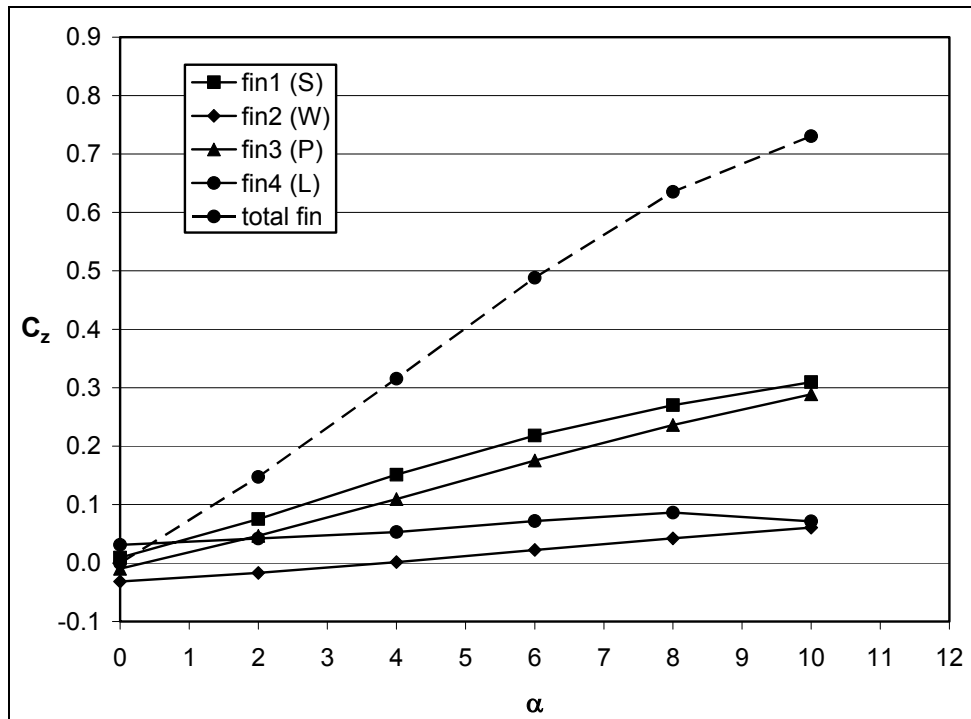


Figure E-1. Grid fin normal force, $\delta = 10^\circ$, Mach 0.6.

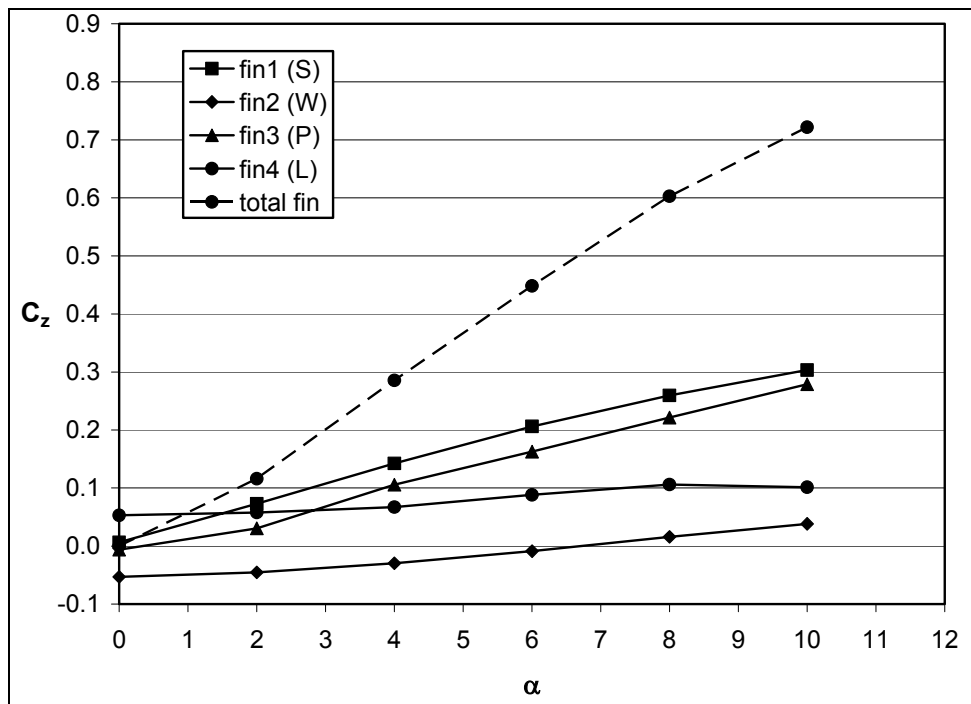


Figure E-2. Grid fin normal force, $\delta = 10^\circ$, Mach 0.9.

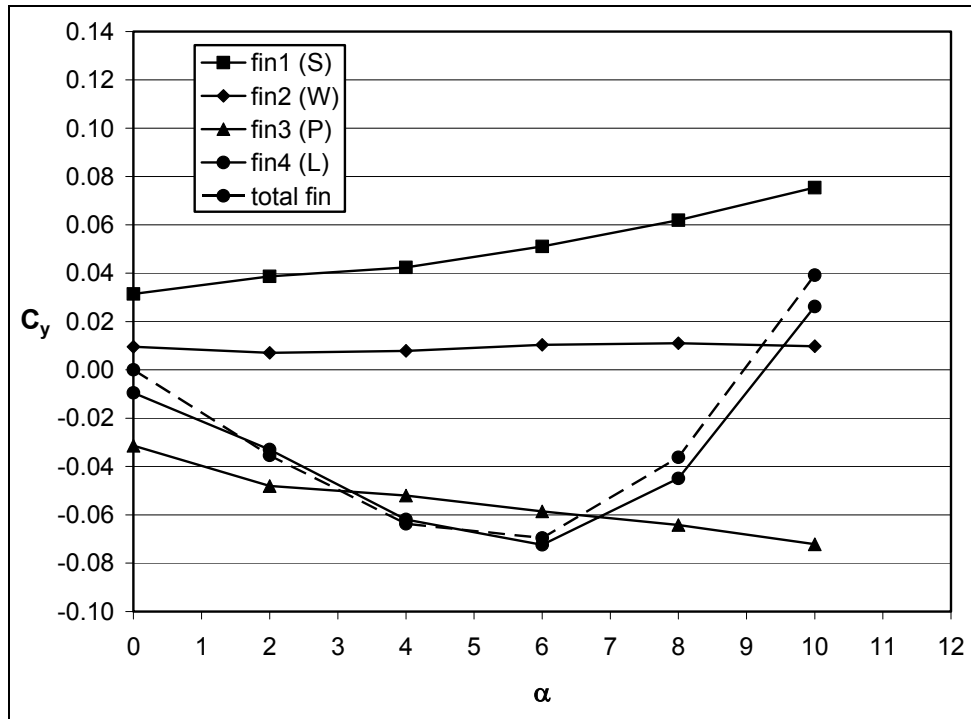


Figure E-3. Grid fin side force, $\delta = 10^\circ$, Mach 0.6.

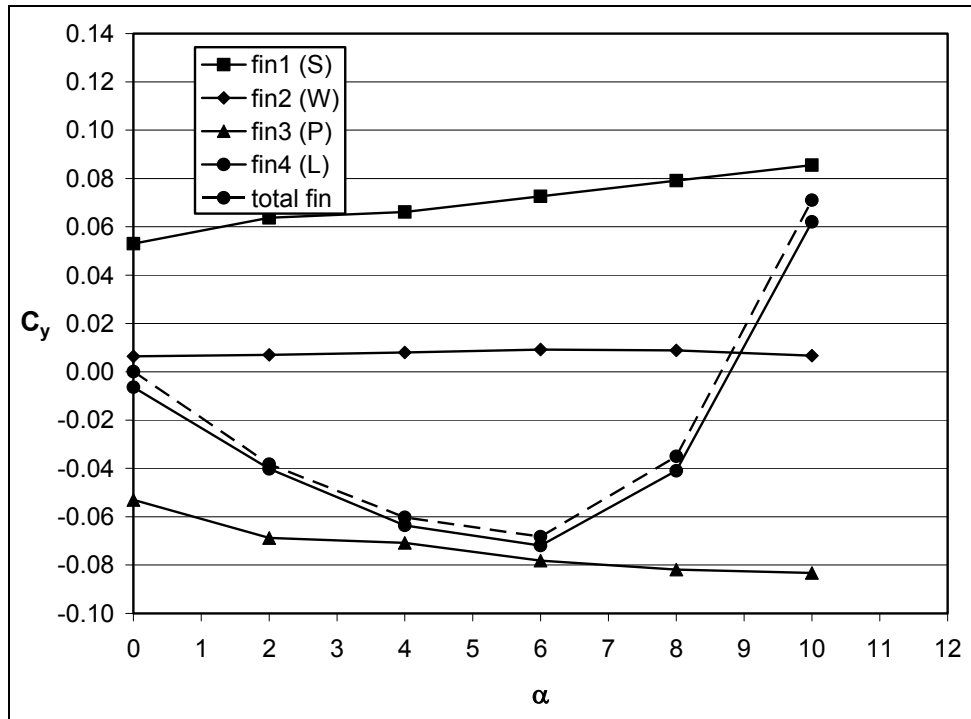


Figure E-4. Grid fin side force, $\delta = 10^\circ$, Mach 0.9.

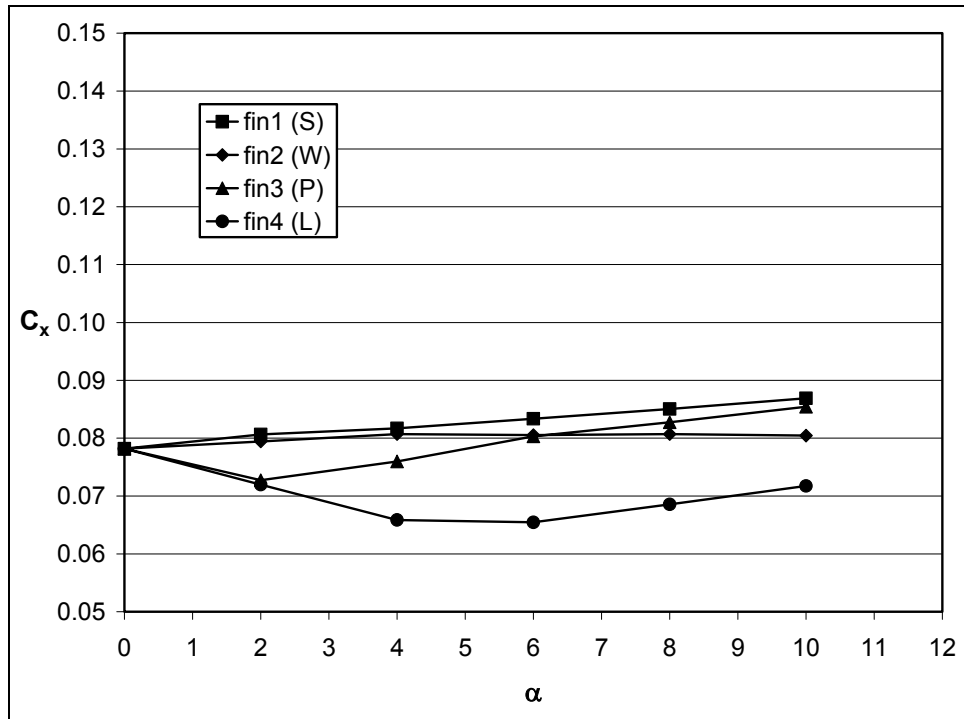


Figure E-5. Grid fin axial force, $\delta = 10^\circ$, Mach 0.6.

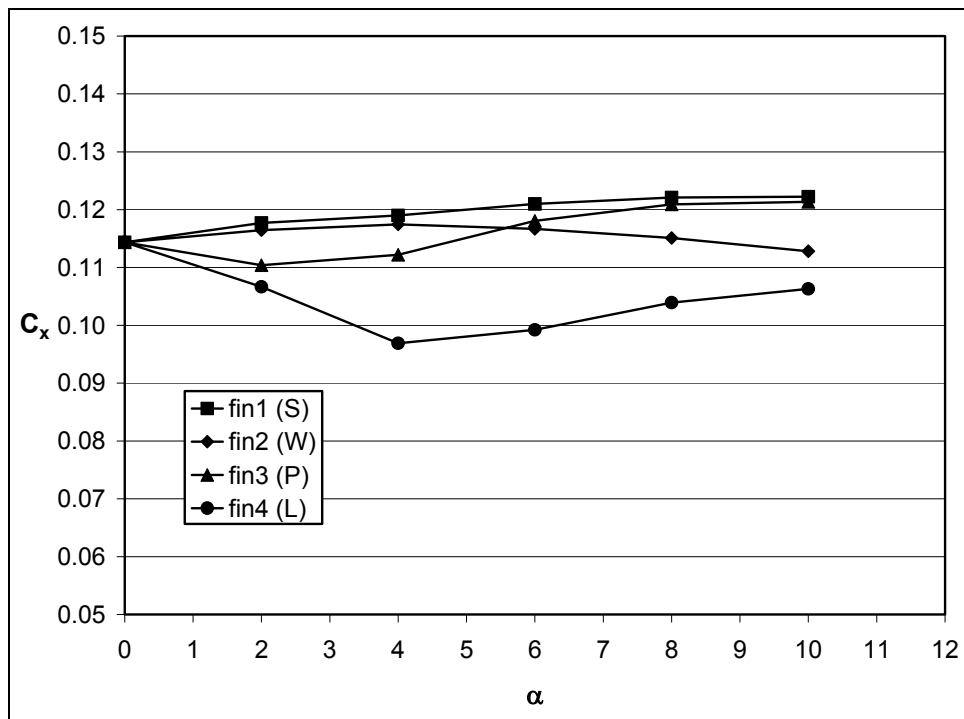


Figure E-6. Grid fin axial force, $\delta = 10^\circ$, Mach 0.9.

Table E-1. Aerodynamic coefficients on grid fins, $\delta = 10^\circ$, Mach 0.6.

α	0	2	4	6	8	10
Axial Force						
Fin 1 (S)	0.0782	0.0807	0.0817	0.0833	0.0850	0.0869
Fin 2 (W)	0.0782	0.0794	0.0807	0.0805	0.0807	0.0804
Fin 3 (P)	0.0782	0.0728	0.0760	0.0803	0.0827	0.0854
Fin 4 (L)	0.0782	0.0720	0.0659	0.0655	0.0686	0.0717
Total fin	0.3127	0.3048	0.3043	0.3097	0.3171	0.3245
Side Force						
Fin 1 (S)	0.0314	0.0387	0.0424	0.0511	0.0619	0.0754
Fin 2 (W)	0.0095	0.0070	0.0078	0.0103	0.0110	0.0097
Fin 3 (P)	-0.0314	-0.0481	-0.0520	-0.0586	-0.0642	-0.0722
Fin 4 (L)	-0.0095	-0.0330	-0.0619	-0.0724	-0.0449	0.0262
Total fin	0.0000	-0.0354	-0.0637	-0.0696	-0.0362	0.0392
Normal Force						
Fin 1 (S)	0.0095	0.0755	0.1513	0.2183	0.2703	0.3099
Fin 2 (W)	-0.0314	-0.0169	0.0017	0.0225	0.0424	0.0606
Fin 3 (P)	-0.0095	0.0467	0.1096	0.1754	0.2363	0.2888
Fin 4 (L)	0.0314	0.0422	0.0532	0.0719	0.0863	0.0714
Total fin	0.0000	0.1475	0.3158	0.4881	0.6353	0.7307

Notes: S = starboard; W = windward; P = port; L = leeward.

Table E-2. Aerodynamic coefficients on grid fins, $\delta = 10^\circ$, Mach 0.9.

α	0	2	4	6	8	10
Axial Force						
Fin 1 (S)	0.1144	0.1177	0.1190	0.1210	0.1221	0.1222
Fin 2 (W)	0.1144	0.1164	0.1174	0.1167	0.1151	0.1128
Fin 3 (P)	0.1144	0.1104	0.1122	0.1181	0.1209	0.1213
Fin 4 (L)	0.1144	0.1067	0.0969	0.0992	0.1039	0.1063
Total fin	0.4575	0.4512	0.4455	0.4549	0.4620	0.4627
Side Force						
Fin 1 (S)	0.0530	0.0637	0.0662	0.0726	0.0791	0.0855
Fin 2 (W)	0.0064	0.0070	0.0080	0.0092	0.0088	0.0067
Fin 3 (P)	-0.0530	-0.0688	-0.0708	-0.0782	-0.0819	-0.0833
Fin 4 (L)	-0.0063	-0.0402	-0.0636	-0.0719	-0.0410	0.0621
Total fin	0.0000	-0.0382	-0.0602	-0.0682	-0.0350	0.0710
Normal Force						
Fin 1 (S)	0.0064	0.0729	0.1424	0.2061	0.2595	0.3032
Fin 2 (W)	-0.0530	-0.0453	-0.0297	-0.0087	0.0159	0.0382
Fin 3 (P)	-0.0063	0.0306	0.1058	0.1627	0.2214	0.2789
Fin 4 (L)	0.0530	0.0578	0.0671	0.0883	0.1060	0.1015
Total fin	0.0001	0.1160	0.2855	0.4483	0.6029	0.7218

Notes: S = starboard; W = windward; P = port; L = leeward.

INTENTIONALLY LEFT BLANK.

Appendix F. Components of Aerodynamic Coefficients

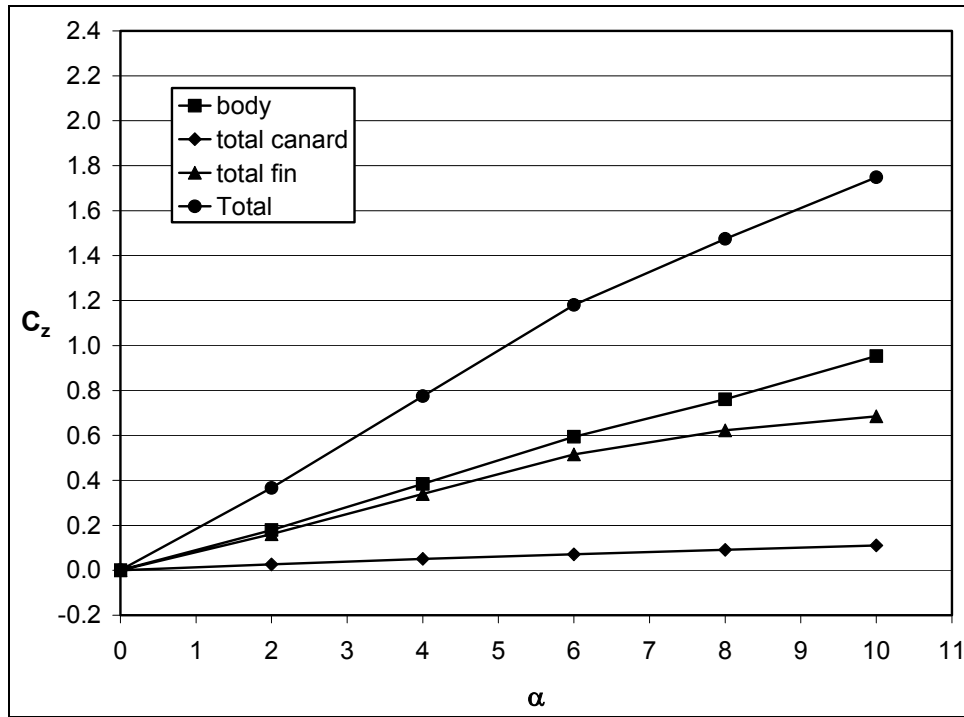


Figure F-1. Components of normal force for the planar fin case, $\delta = 10^\circ$, Mach 0.6.

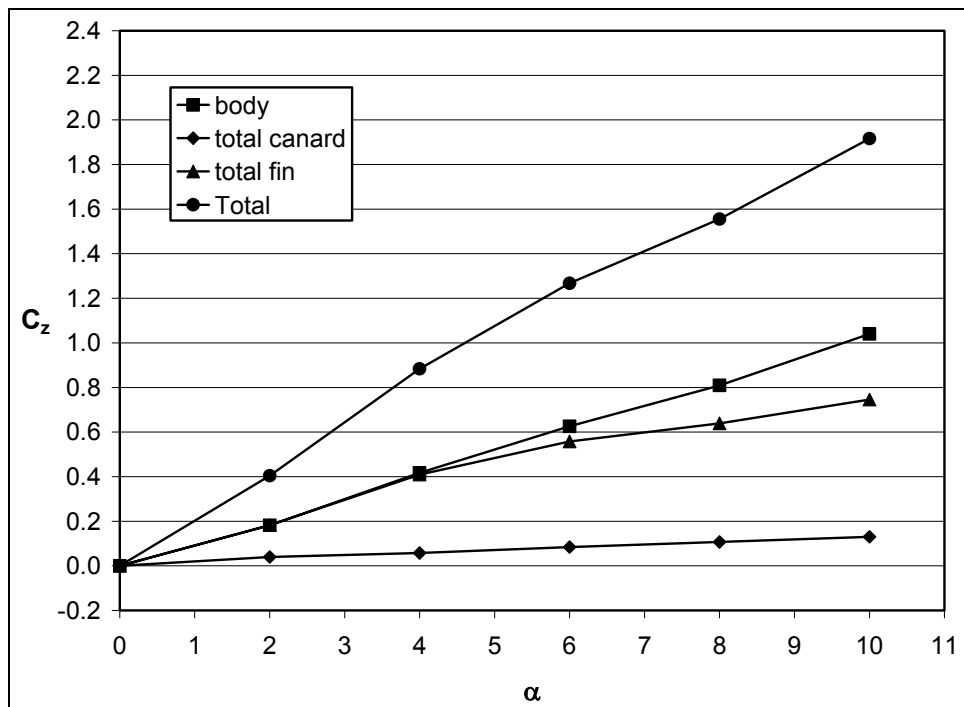


Figure F-2. Components of normal force for the planar fin case, $\delta = 10^\circ$, Mach 0.9.

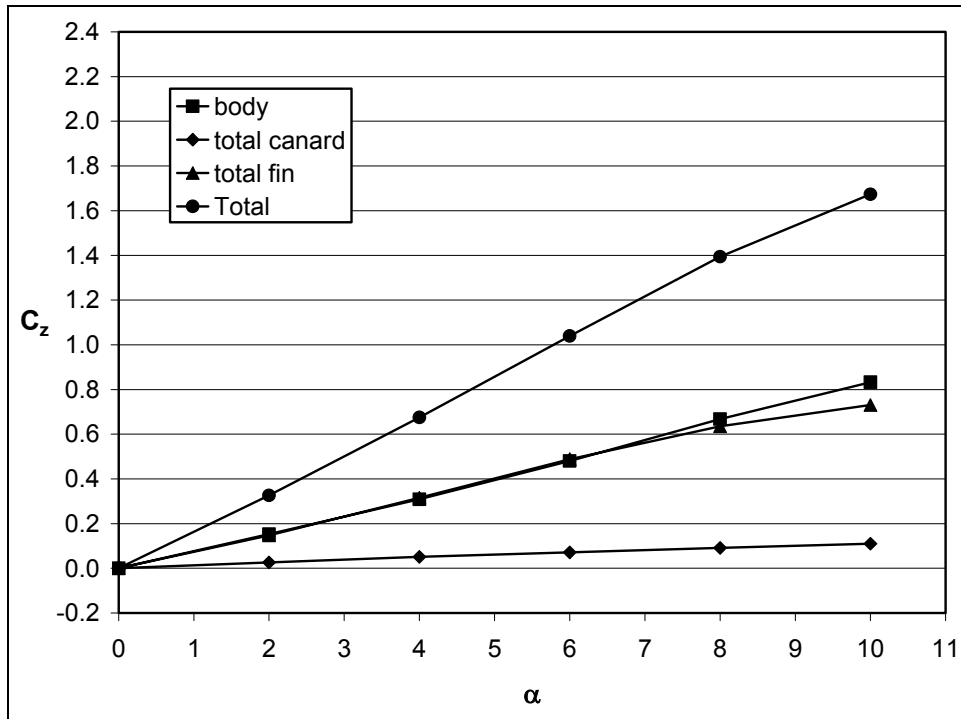


Figure F-3. Components of normal force for the grid fin case, $\delta = 10^\circ$, Mach 0.6.

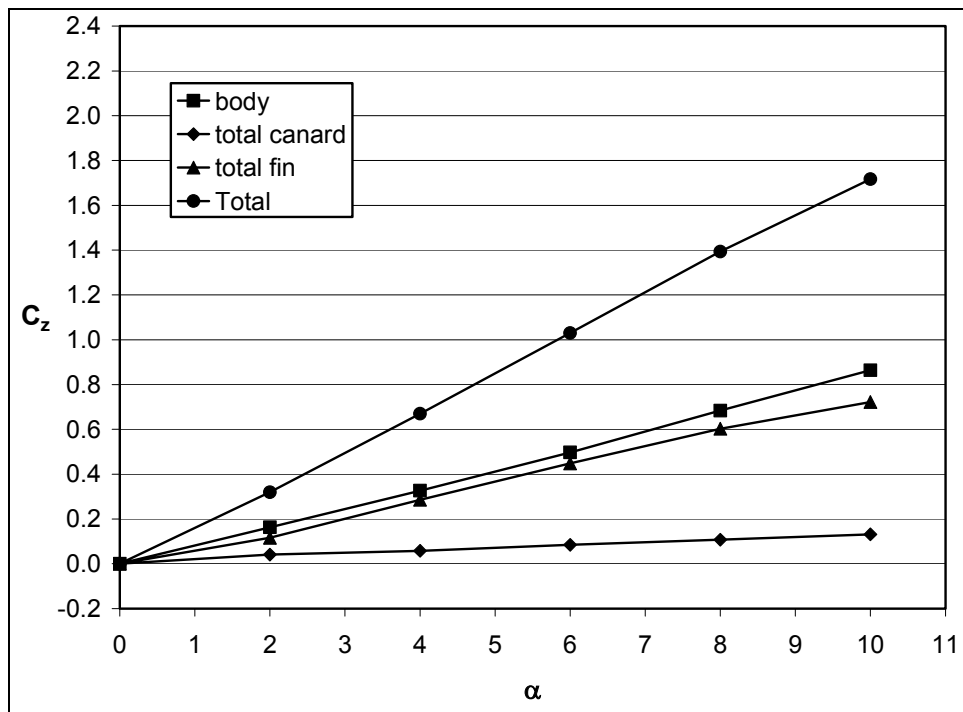


Figure F-4. Components of normal force for the grid fin case, $\delta = 10^\circ$, Mach 0.9.

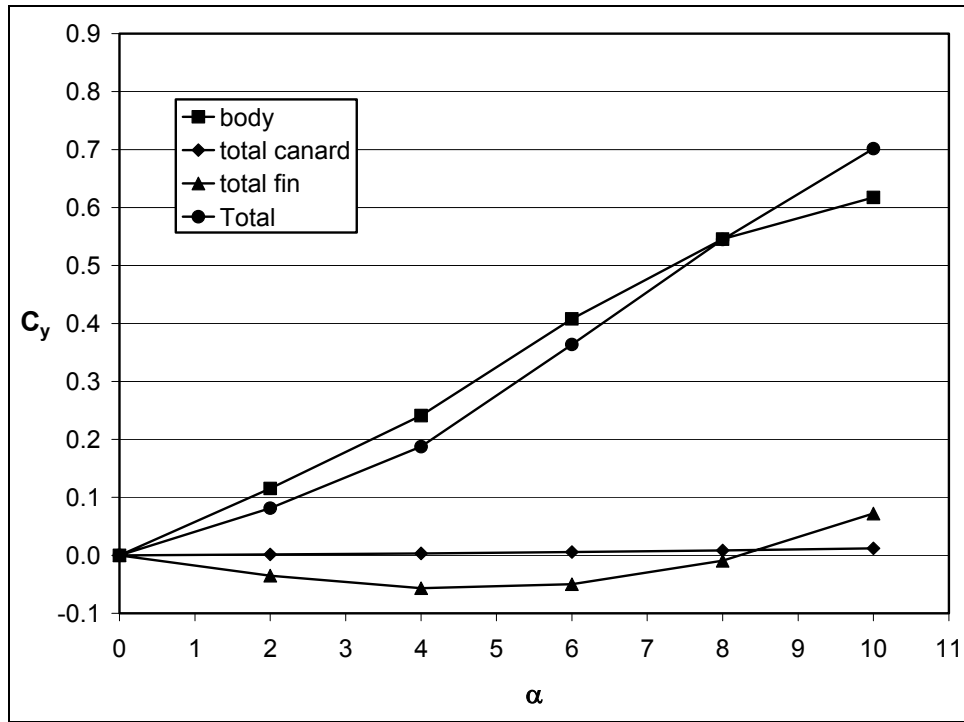


Figure F-5. Components of side force for the planar fin case, $\delta = 10^\circ$, Mach 0.6.

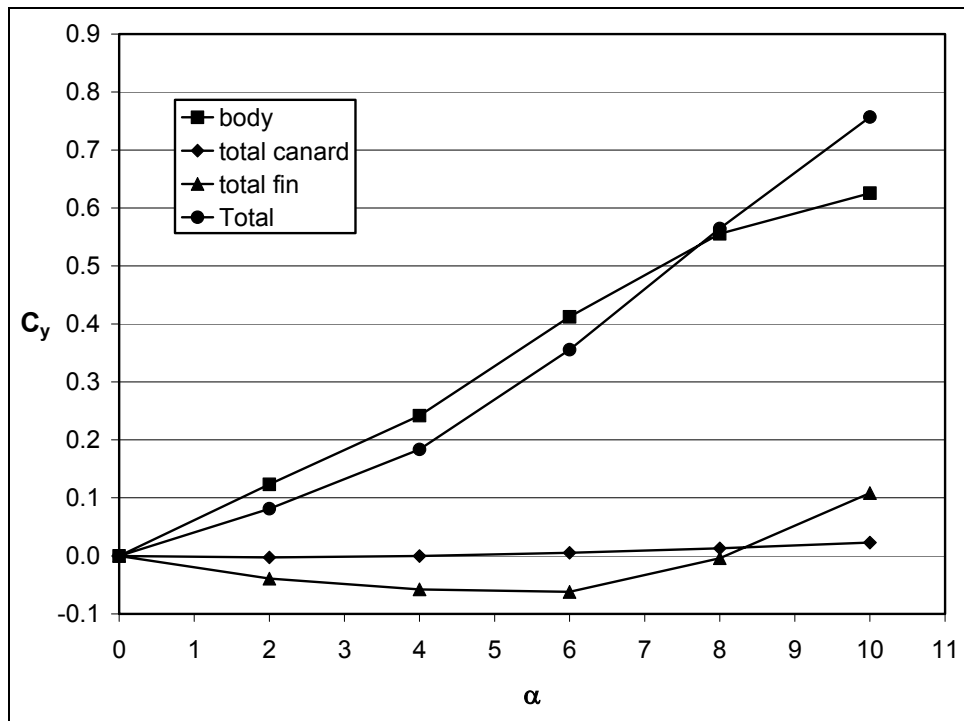


Figure F-6. Components of side force for the planar fin case, $\delta = 10^\circ$, Mach 0.9.

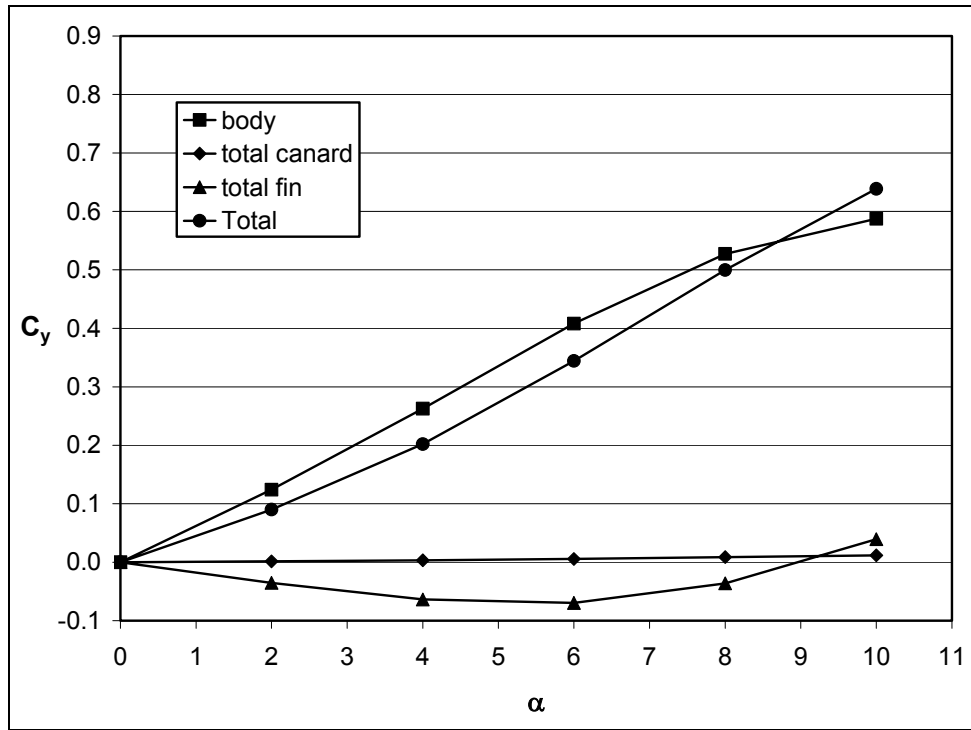


Figure F-7. Components of side force for the grid fin case, $\delta = 10^\circ$, Mach 0.6.

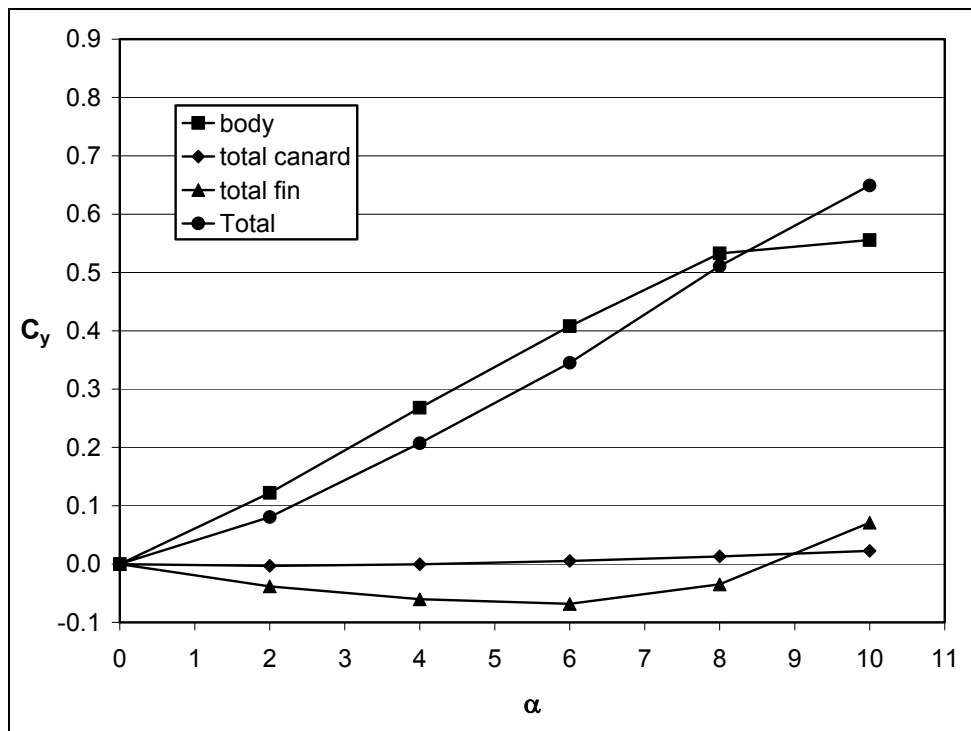


Figure F-8. Components of side force for the grid fin case, $\delta = 10^\circ$, Mach 0.9.

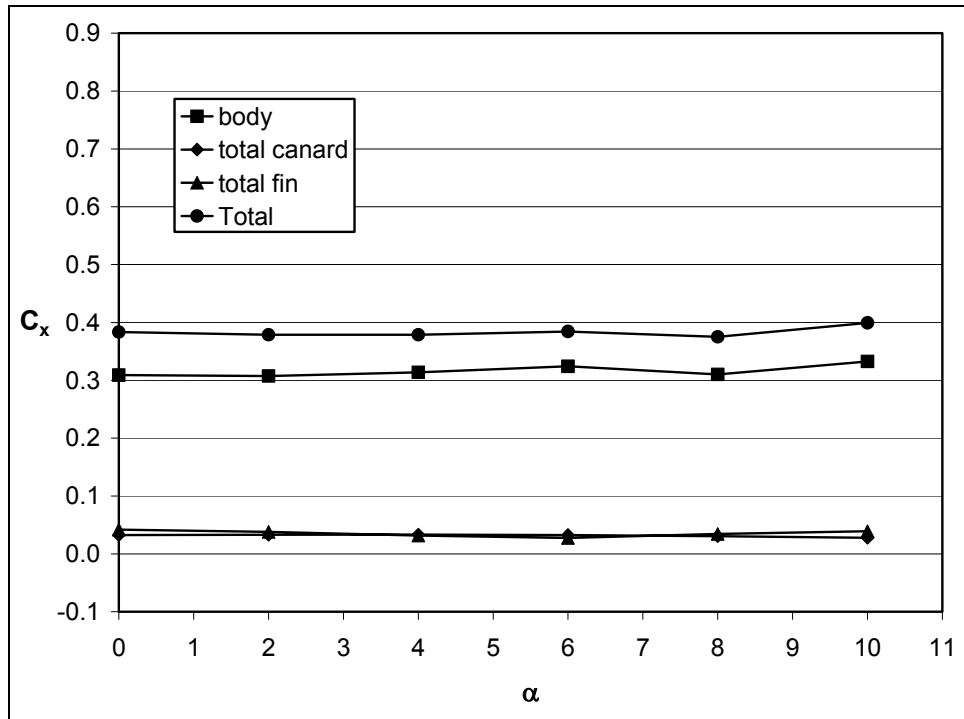


Figure F-9. Components of axial force for the planar fin case, $\delta = 10^\circ$, Mach 0.6.

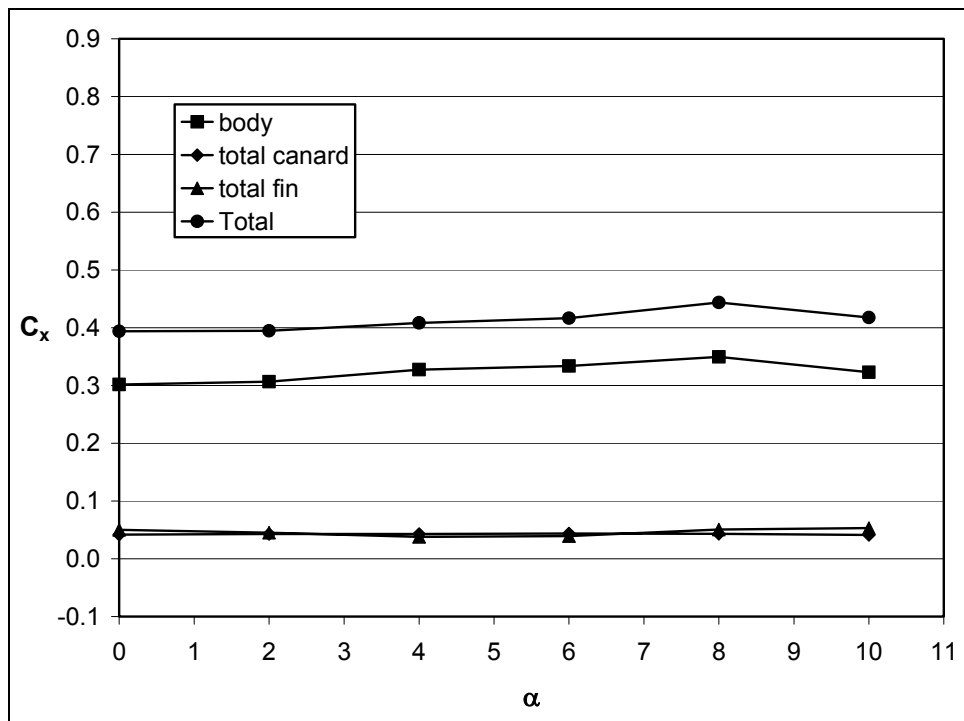


Figure F-10. Components of axial force for the planar fin case, $\delta = 10^\circ$, Mach 0.9.

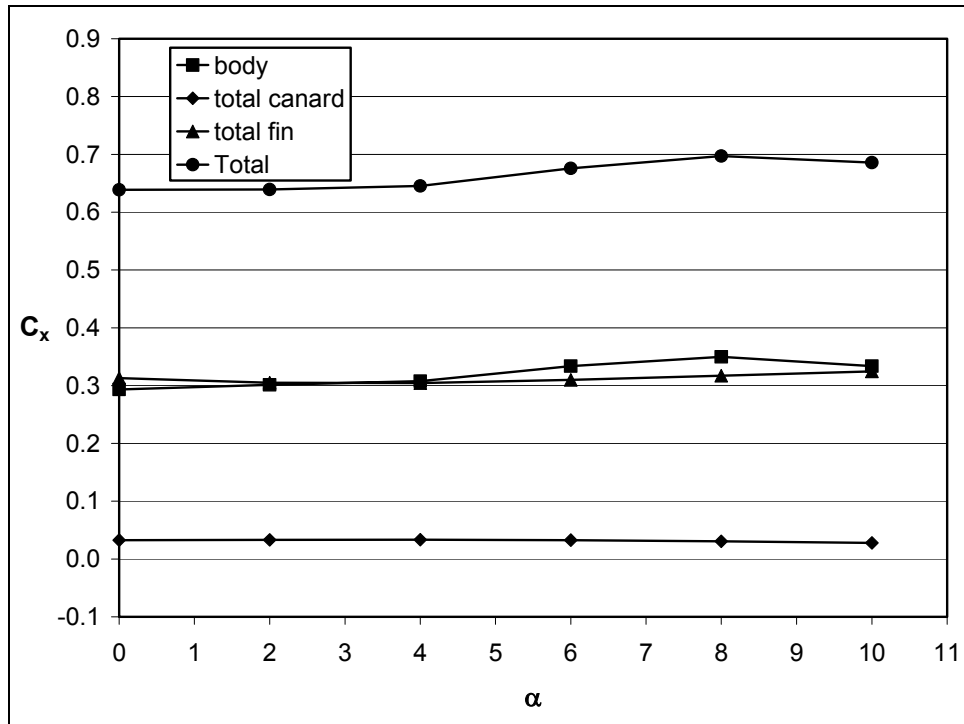


Figure F-11. Components of axial force for the grid fin case, $\delta = 10^\circ$, Mach 0.6.

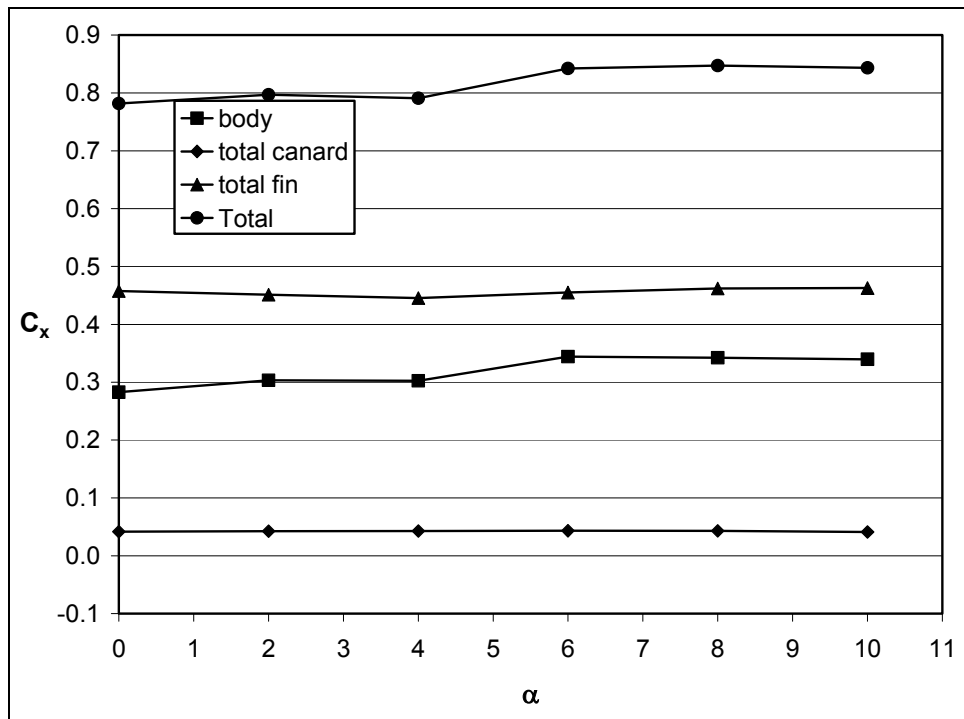


Figure F-12. Components of axial force for the grid fin case, $\delta = 10^\circ$, Mach 0.9.

Table F-1. Components of aerodynamic coefficients, planar fin case, $\delta = 10^\circ$, Mach 0.6.

α	0	2	4	6	8	10
Axial Force						
Body	0.3088	0.3075	0.3138	0.3242	0.3104	0.3326
Total canard	0.0326	0.0332	0.0334	0.0326	0.0305	0.0276
Total fin	0.0420	0.0381	0.0316	0.0275	0.0344	0.0391
Total	0.3835	0.3788	0.3788	0.3843	0.3753	0.3993
Side Force						
Body	0.0000	0.1152	0.2410	0.4078	0.5453	0.6173
Total canard	0.0000	0.0014	0.0032	0.0056	0.0085	0.0120
Total fin	0.0000	-0.0351	-0.0568	-0.0498	-0.0094	0.0721
Total	0.0000	0.0814	0.1874	0.3636	0.5445	0.7014
Normal Force						
Body	0.0012	0.1788	0.3847	0.5940	0.7606	0.9532
Total canard	0.0000	0.0263	0.0509	0.0711	0.0914	0.1106
Total fin	0.0000	0.1610	0.3397	0.5156	0.6228	0.6829
Total	0.0012	0.3662	0.7752	1.1807	1.4748	1.7487

Table F-2. Components of aerodynamic coefficients, planar fin case, $\delta = 10^\circ$, Mach 0.9.

α	0	2	4	6	8	10
Axial Force						
Body	0.3018	0.3067	0.3274	0.3337	0.3498	0.3228
Total canard	0.0419	0.0429	0.0430	0.0436	0.0432	0.0414
Total fin	0.0502	0.0451	0.0379	0.0394	0.0506	0.0533
Total	0.3939	0.3947	0.4084	0.4167	0.4436	0.4176
Side Force						
Body	0.0000	0.1232	0.2418	0.4122	0.5555	0.6255
Total canard	0.0000	-0.0027	-0.0004	0.0054	0.0130	0.0229
Total fin	0.0000	-0.0392	-0.0578	-0.0621	-0.0039	0.1084
Total	0.0000	0.0813	0.1836	0.3555	0.5647	0.7568
Normal Force						
Body	0.0000	0.1818	0.4166	0.6256	0.8091	1.0403
Total canard	0.0000	0.0397	0.0573	0.0836	0.1067	0.1303
Total fin	0.0000	0.1823	0.4095	0.5582	0.6391	0.7453
Total	0.0000	0.4038	0.8835	1.2674	1.5549	1.9158

Table F-3. Components of aerodynamic coefficients, grid fin case, $\delta = 10^\circ$, Mach 0.6.

α	0	2	4	6	8	10
Axial Force						
Body	0.2931	0.3011	0.3078	0.3336	0.3496	0.3336
Total Canard	0.0327	0.0332	0.0334	0.0326	0.0305	0.0277
Total Fin	0.3127	0.3048	0.3043	0.3097	0.3171	0.3245
Total	0.6385	0.6391	0.6454	0.6758	0.6971	0.6857
Side Force						
Body	0.0000	0.1240	0.2626	0.4082	0.5274	0.5874
Total Canard	0.0000	0.0014	0.0032	0.0057	0.0086	0.0119
Total Fin	0.0000	-0.0354	-0.0637	-0.0696	-0.0362	0.0392
Total	0.0000	0.0900	0.2021	0.3442	0.4998	0.6385
Normal Force						
Body	0.0000	0.1528	0.3086	0.4802	0.6675	0.8325
Total Canard	0.0000	0.0263	0.0509	0.0712	0.0915	0.1104
Total Fin	0.0000	0.1475	0.3158	0.4881	0.6353	0.7307
Total	0.0000	0.3266	0.6753	1.0396	1.3943	1.6735

Table F-4. Components of aerodynamic coefficients, grid fin case, $\delta = 10^\circ$, Mach 0.9.

α	0	2	4	6	8	10
Axial Force						
Body	0.2826	0.3033	0.3026	0.3442	0.3422	0.3396
Total canard	0.0417	0.0425	0.0428	0.0432	0.0429	0.0411
Total fin	0.4575	0.4512	0.4455	0.4549	0.4620	0.4627
Total	0.7817	0.7970	0.7909	0.8423	0.8471	0.8434
Side Force						
Body	0.0000	0.1220	0.2680	0.4078	0.5327	0.5557
Total canard	0.0000	-0.0032	-0.0004	0.0054	0.0132	0.0225
Total fin	0.0000	-0.0382	-0.0602	-0.0682	-0.0350	0.0710
Total	0.0000	0.0805	0.2073	0.3450	0.5109	0.6492
Normal Force						
Body	0.0000	0.1627	0.3263	0.4968	0.6836	0.8639
Total canard	0.0000	0.0409	0.0577	0.0848	0.1073	0.1315
Total fin	0.0001	0.1160	0.2855	0.4483	0.6029	0.7218
Total	0.0001	0.3197	0.6695	1.0299	1.3938	1.7172

List of Abbreviations and Symbols

A	cell face area, m^2
cal.	caliber (1 caliber = D)
C_l	rolling moment coefficient
C_m	pitching moment coefficient
C_n	yawing moment coefficient
$C_{NF\alpha}$	zero angle-of-attack fin normal force slope
C_p	pressure coefficient
C_x	axial force coefficient
C_y	side force coefficient
C_z	normal force coefficient
D	missile base diameter, m
E	total energy, J
F	inviscid flux vector
G	viscous flux vector
H	vector of source terms
i, j, k	Cartesian unit vectors
M	Mach number
MRP	moment reference point
p	pressure, N/m^2
q	heat flux vector
u, v, w	velocity components in x, y, z directions, m/s
V	cell volume, m^3
v	velocity vector (= $ui + vj + wk$)
x_{cp}	location of center of pressure

W	vector of conservative variables
x, y, z	axial, horizontal, and vertical body axes
α	angle of attack, degree
δ	canard deflection angle, degree
ν	kinematic viscosity, m^2/s
ρ	density, kg/m^3
τ	viscous stress tensor

NO. OF
COPIES ORGANIZATION

1
(PDF
Only) DEFENSE TECHNICAL
INFORMATION CENTER
DTIC OCA
8725 JOHN J KINGMAN RD
STE 0944
FT BELVOIR VA 22060-6218

1 COMMANDING GENERAL
US ARMY MATERIEL CMD
AMCRDA TF
5001 EISENHOWER AVE
ALEXANDRIA VA 22333-0001

1 INST FOR ADVNCD TCHNLGY
THE UNIV OF TEXAS
AT AUSTIN
3925 W BRAKER LN STE 400
AUSTIN TX 78759-5316

1 US MILITARY ACADEMY
MATH SCI CTR EXCELLENCE
MADN MATH
THAYER HALL
WEST POINT NY 10996-1786

1 DIRECTOR
US ARMY RESEARCH LAB
AMSRD ARL D
DR D SMITH
2800 POWDER MILL RD
ADELPHI MD 20783-1197

1 DIRECTOR
US ARMY RESEARCH LAB
AMSRD ARL CS IS R
2800 POWDER MILL RD
ADELPHI MD 20783-1197

3 DIRECTOR
US ARMY RESEARCH LAB
AMSRD ARL CI OK TL
2800 POWDER MILL RD
ADELPHI MD 20783-1197

3 DIRECTOR
US ARMY RESEARCH LAB
AMSRD ARL CS IS T
2800 POWDER MILL RD
ADELPHI MD 20783-1197

NO. OF
COPIES ORGANIZATION

ABERDEEN PROVING GROUND

1 DIR USARL
AMSRD ARL CI OK TP (BLDG 4600)

<u>NO. OF COPIES</u>	<u>ORGANIZATION</u>	<u>NO. OF COPIES</u>	<u>ORGANIZATION</u>
3	USAF WRIGHT AERONAUTICAL LABORATORIES AFWAL FIMG J SHANG N E SCAGGS WPAFB OH 45433-6553	4	COMMANDER US ARMY TACOM ARDEC AMSTA AR FSF T BLDG 382 C NG H HUDGINS J GRAU W KOENIG PICATINNY ARSENAL NJ 07806-5000
1	COMMANDER NSWC CODE B40 W YANTA DAHLGREN VA 22448-5100	1	DEFENSE INTELLIGENCE AGENCY MISSILE AND SPACE INT CTR MSA 1 A NICHOLSON BLDG 4545 FOWLER RD REDSTONE ARSENAL AL 35898-5500
1	COMMANDER NSWC CODE 420 A WARDLAW INDIAN HEAD MD 20640-5035	2	AFRL/MNAV G ABATE M VALENTINO 101 W EGLIN BLVD STE 219 EGLIN AIR FORCE BASE FL 32542
4	DIRECTOR NASA LANGLEY RESEARCH CTR TECH LIBRARY D M BUSHNELL M J HEMSCH J SOUTH LANGLEY STATION HAMPTON VA 23665	1	COMMANDER US ARMY TACOM AMSTA AR CCH B P VALENTI BLDG 65 S PICATINNY ARSENAL NJ 07806-5001
2	DARPA P KEMMEY J RICHARDSON 3701 N FAIRFAX DR ARLINGTON VA 22203-1714	1	COMMANDER US ARMY ARDEC ATTN SFAE FAS SD M DEVINE PICATINNY ARSENAL NJ 07806-5001
7	DIRECTOR NASA AMES RESEARCH CTR T 27B 1 L SCHIFF T 27B 1 T HOLST MS 237 2 D CHAUSSEE MS 258 M RAI MS 258 1 B MEAKIN MS T27B 2 M AFTOSMIS MS T27B 2 J MELTON MOFFETT FIELD CA 94035	1	AEROPREDICTION INC F MOORE 9449 GROVER DR STE 201 KING GEORGE VA 22485
3	AIR FORCE ARMAMENT LAB AFATL/FXA S C KORN B SIMPSON D BELK EGLIN AFB FL 32542-5434	1	AEROJET ELECTRONICS PLANT D W PILLASCH B170 DEPT 5311 PO BOX 296 1100 W HOLLYVALE ST AZUSA CA 91702
		1	MASSACHUSETTS INSTITUTE OF TECHNOLOGY TECH LIBRARY 77 MASSACHUSETTS AVE CAMBRIDGE MA 02139

<u>NO. OF COPIES</u>	<u>ORGANIZATION</u>	<u>NO. OF COPIES</u>	<u>ORGANIZATION</u>
1	LOS ALAMOS NATIONAL LAB B HOGAN MS G770 LOS ALAMOS NM 87545	1	COMMANDER USAAMCOM AMSAM RD SS G LANDINGHAM REDSTONE ARSENAL AL 35898-5252
3	DIRECTOR SANDIA NATIONAL LABS DIV 1554 W OBERKAMPF DIV 1554 F BLOTTNER DIV 1636 W WOLFE ALBUQUERQUE NM 87185	10	COMMANDER USAAMCOM AMSAM RD SS AT R KRETZSCHMAR L AUMAN E KREEGER C MIKKELSON E VAUGHN (5 CPS) W WASHINGTON REDSTONE ARSENAL AL 35898-5252
1	NAWC D FINDLAY MS 3 BLDG 2187 PATUXENT RIVER MD 20670	4	FLUENT INC G STUCKERT T SCHEIDEGGER D LYTLE D LEE 10 CAVENDISH CT CENTERRA RESOURCE PARK LEBANON NH 03766-1442
1	METACOMP TECHNOLOGIES INC S R CHAKRAVARTHY 28632-B ROADSIDE DR SUITE 255 AGOURA HILLS CA 91301		
1	ADVANCED TECHNOLOGY CTR ARVIN/CALSPAN AERODYNAMICS RESEARCH DEPT M S HOLDEN PO BOX 400 BUFFALO NY 14225		<u>ABERDEEN PROVING GROUND</u>
1	UNIV OF ILLINOIS AT URBANA CHAMPAIGN DEPT OF MECHANICAL AND INDUSTRIAL ENGRG J C DUTTON URBANA IL 61801	27	DIR USARL AMSRD ARL WM J SMITH T ROSENBERGER AMSRD ARL WM B A HORST W CIEPIELA AMSRD ARL WM BA D LYON T BROWN D HEPNER AMSRD ARL WM BD B FORCH M NUSCA AMSRD ARL WM BC P PLOSTINS J DESPIRITO (5 CPS) B GUIDOS K HEAVEY J NEWILL J SAHU S SILTON AMSRD ARL WM BC P WEINACHT AMSRD ARL WM BF S WILKERSON H EDGE
1	UNIVERSITY OF MARYLAND DEPT OF AEROSPACE ENGRG J D ANDERSON JR COLLEGE PARK MD 20742		
1	UNIVERSITY OF TEXAS DEPT OF AEROSPACE ENGRG MECHANICS D S DOLLING AUSTIN TX 78712-1055		
1	COMMANDER US ARMY TACOM ARDEC BLDG 162S AMCPM DS MO P J BURKE PICATINNY ARSENAL NJ 07806-5000		

NO. OF
COPIES ORGANIZATION

ABERDEEN PROVING GROUND (CONT'D)

AMSRD ARL SL BE
A MIKHAIL
AMSRD ARL CI
C NIETUBICZ
AMSRD ARL CI HC
R NOAK
R ANGELINI

NO. OF
COPIES ORGANIZATION

- 1 DSTL BEDFORD
T BIRCH
BEDFORD TECHNOLOGY PARK
BEDFORD
MK44 2FQ

- 1 DSTL FORT HALSTEAD
J EDWARDS
SEVENOAKS KENT
TN14 7BP

- 3 DEFENCE RESEARCH AND
DEVELOPMENT CANADA
VALCARTIER
F LESAGE
E FOURNIER
A DUPUIS
2459 PIE XI BLVD NORTH
VAL BELAIR QC G3J1X5
CANADA

- 1 INSTITUTE SAINT LOUIS
C BERNER
PO BOX 34
68301 SAINT LOUIS CEDEX
FRANCE